

# Monolithic Perovskite Tandem Solar Cells: A Review of the Present Status and Advanced Characterization Methods Toward 30% Efficiency

Marko Jošt, Lukas Kegelmann, Lars Korte, and Steve Albrecht\*

Tandem solar cells are the next step in the photovoltaic (PV) evolution due to their higher power conversion efficiency (PCE) potential than currently dominating, but inherently limited, single-junction solar cells. With the emergence of metal halide perovskite absorber materials, the fabrication of highly efficient tandem solar cells, at a reasonable cost, can significantly impact the future PV landscape. The perovskite-based tandem solar cells have already shown that they can convert light more efficiently than their standalone sub-cells. However, to reach PCEs over 30%, several challenges have to be overcome and the understanding of this fascinating technology has to be broadened. In this review, the main scientific and engineering challenges in the field are presented, alongside a discussion of the current status of three main perovskite tandem technologies: perovskite/silicon, perovskite/CIGS, and perovskite/perovskite tandem solar cells. A summary of the advanced structural, electrical, optical, radiative, and electronic characterization methods as well as simulations being utilized for perovskite-based tandem solar cells is presented. The main findings are summarized and the strength of the techniques to overcome the challenges and gain deeper knowledge for further performance improvement is assessed. Finally, the PCE potential in different experimental and theoretical limits is compared with an aim to shed light on the path towards overcoming the 30% efficiency threshold for all of the three herein reviewed tandem technologies.

## 1. Introduction

The installation of photovoltaic (PV) modules has steadily increased over the last decades making PV the fastest growing of all power generation technologies in Germany.<sup>[1]</sup> However, worldwide, only ≈2% of the electricity is produced from photovoltaics.<sup>[2]</sup> In order to keep the global warming below the 2 °C target as fixed in the Paris Agreement on Climate in 2015, we need to utilize significantly more solar energy even without considering the ever-increasing energy consumption and rising number of electric cars. It is therefore of crucial importance to further accelerate the global installation of PV modules and the main lever for success is to reduce the levelized costs of PV energy (LCOE).<sup>[3–6]</sup>

At the moment, the dominating fraction of the PV market are single-junction solar cells that are inherently limited in the power conversion efficiency (PCE) of converting solar to electrical power. On the other hand, different solar materials can be combined into tandem solar cells that are made from two different absorber materials, sharing the incident solar spectrum

and consequently enabling a higher PCE. As they do not induce additional area related Balance-of-System costs, high-efficiency tandem solar cells can be a significant measure to reduce the LCOE in the future.<sup>[3,4,7,8]</sup> However, this requires the gain in PCE to prevail over the additional fabrication costs. Thus, the PV field is searching for new cost-effective and efficient solar cell candidates for tandem integration.

Especially materials such as inorganic-organic metal halide perovskites are highly promising absorber materials to be utilized in next-generation solar cells.<sup>[9–11]</sup> These perovskite materials have emerged as the hottest research topic in solar research with over 7000 reported publications focusing on perovskite solar cells, accumulated by the end of 2019.<sup>[12]</sup> They have a high certified single-junction PCE of 25.2% and they also fulfill the requirement to be a perfect tandem partner with mature technologies, such as crystalline silicon or CIGS. Briefly, these requirements are as follows: complementary solar spectral absorption, tunability of the band gap, high PCE as well as ease of processing and process compatibility with silicon and CIGS technologies. With that, it is possible to achieve the highest

Dr. M. Jošt, Dr. L. Kegelmann, Prof. S. Albrecht  
Helmholtz-Center Berlin  
Young Investigator Group for Perovskite Tandem Solar Cells

Berlin 12489, Germany  
E-mail: steve.albrecht@helmholtz-berlin.de

Dr. L. Korte  
Institute for Silicon Photovoltaics  
Berlin 12489, Germany

Prof. S. Albrecht  
Faculty IV, Electrical Engineering and Computer Science  
Technical University Berlin  
Berlin 10587, Germany

 The ORCID identification number(s) for the author(s) of this article can be found under <https://doi.org/10.1002/aenm.201904102>.

© 2020 Helmholtz-Zentrum Berlin (HZB). Published by WILEY-VCH Verlag GmbH & Co. KGaA, Weinheim. This is an open access article under the terms of the Creative Commons Attribution License, which permits use, distribution and reproduction in any medium, provided the original work is properly cited.

DOI: 10.1002/aenm.201904102

efficiency tandem modules at reasonable costs in the near future.<sup>[3,4,8]</sup> In addition, due to the possibility of bandgap tuning, the perovskites themselves can be combined into all-perovskite tandem solar cells, with both the top and bottom cells using a perovskite absorber. All of these still very young technologies enable remarkable PCEs close to or even above those of the best single-junction cells.<sup>[13–15]</sup> This potential has been recognized not only by various research institutes but also by several start-up companies, such as Oxford PV, Swift Solar, and Tandem PV.

Inorganic–organic perovskites are compounds with the ABX<sub>3</sub> formula containing methylammonium iodide (MAI), formamidinium iodide (FAI), Cs or their mixture as A site cation, Pb, Sn, or a mixture of them as divalent metal (B site) and I and/or Br as halide (X site).<sup>[16]</sup> By compositional engineering, the bandgap can be fine tuned to meet the absorption properties required by a specific tandem architecture, which offers a great advantage to use perovskite materials in different tandem designs such as the wide bandgap top cell or low bandgap bottom cell. Most of these perovskite compound combinations have outstanding optoelectronic properties for integration as solar absorbers, namely high absorption for energies above and very low absorption at energies below the bandgap.<sup>[17]</sup> In addition, a low number of recombination-active defects ensure carrier lifetimes of several microseconds.<sup>[18–21]</sup> With that, all incident light can be absorbed in layers with a thickness of  $\approx 1 \mu\text{m}$  or even less, and charges can easily diffuse toward the selective contact layers and get extracted effectively. With the high optoelectronic quality of the perovskite bulk, the main recombination losses occur at the interfaces to the charge selective layers.<sup>[22–24]</sup> These can be altered by utilizing interlayers, surface modifications, or proper contact materials to enable the highest solar cell PCEs.<sup>[25–30]</sup>

This is further supported by the ease of fabrication and a wide choice of processing techniques: perovskites can be either processed from solution, e.g., by spin coating<sup>[16,31]</sup> or printing techniques,<sup>[32,33]</sup> by vacuum deposition using thermal co-evaporation,<sup>[34–36]</sup> or even by hybrid processes combining both wet and dry processes.<sup>[37–39]</sup> The films are typically crystallized at temperatures  $\approx 100^\circ\text{C}$  or less, not harming the bottom cell, and precursor materials are cheap and abundant. The fabrication routes are thus reasonably cost-friendly and perovskite-based tandem solar cells could be produced at low costs in the future. This is a clear benefit against existing III-V semiconductor tandem solar cells that are restricted by complex and expensive fabrication that hinders mass market entrance.<sup>[38,40]</sup>

**Figure 1a** schematically visualizes the recent improvements and also the potential for Si, CIGS, and perovskite single-junctions, displaying laboratory-scale results on the left side of the figure. While the single-junction PCE improves over time with the steepest rise for perovskites, all single-junctions are not likely to overcome the practical PCE limit at  $\approx 27\%$  on cell level (and slightly lower in modules) in the next years.<sup>[41]</sup> This has triggered the rise of the tandem technology, which has already proven to overcome this single-junction practical limit by reducing losses from thermalization and non-absorbed photons.<sup>[42,43]</sup> In addition, the first perovskite-based triple-junction solar cells have also already been reported as proof-of-concept.<sup>[44,45]</sup> These triple junctions have even higher efficiency potential and will likely enable superior module PCEs in the future, as suggested in Figure 1a.



**Marko Jošt** received the Ph.D. degree from the University of Ljubljana, Ljubljana, Slovenia, and Technical University Berlin, Berlin, Germany, where he investigated light management in solar cells. From 2017 to 2020, he was a postdoctoral researcher with the Young Investigator Group Perovskite Tandem Solar Cells, Helmholtz-Zentrum Berlin, Berlin, Germany. He is currently an assistant lecturer at the University of Ljubljana. His research interest focuses on improving the efficiency of monolithic perovskite/silicon tandem solar cells, with an emphasis on optical optimization and interface engineering, and outdoor operation of perovskite solar cells.



**Lukas Kegelmann** studied perovskite/silicon tandem solar cells already during his master thesis in 2014 and continued this research in his doctorate from 2015 to 2018 within the HyPerCells Graduate School of the Helmholtz-Zentrum Berlin and Potsdam University, Germany. He followed up as a postdoctoral researcher within the group of Prof. Steve Albrecht investigating Perovskite Tandem Solar Cells. His research interest focuses on examining and improving the interfaces in perovskite solar cells and transferring these advances to monolithic perovskite/silicon tandem solar cells.

Figure 1b presents the PCE evolution of perovskite/silicon (purple), perovskite/CIGS (red), and all-perovskite (perovskite/perovskite) tandem solar cells (green) with two- and four-terminal configuration in solid and open (and more transparent) symbols, respectively. These two tandem architectures are dominating the scientific literature, and both have advantages and disadvantages. In this review, the primary focus is on monolithic, two-terminal device architectures. This architecture uses an internal junction to series-interconnect the sub-cells, requiring two external contacts only (2-terminal, 2T), like in single-junctions. This enables similar module related costs as single-junction modules, which is highly relevant for a low LCOE. The other advantages of 2T devices are just summarized quickly here: a lower current needs to be transported at a higher voltage that reduces losses from series resistance, and lateral current flow is only needed in the two external contact layers, reducing the number of heavily doped transport layers

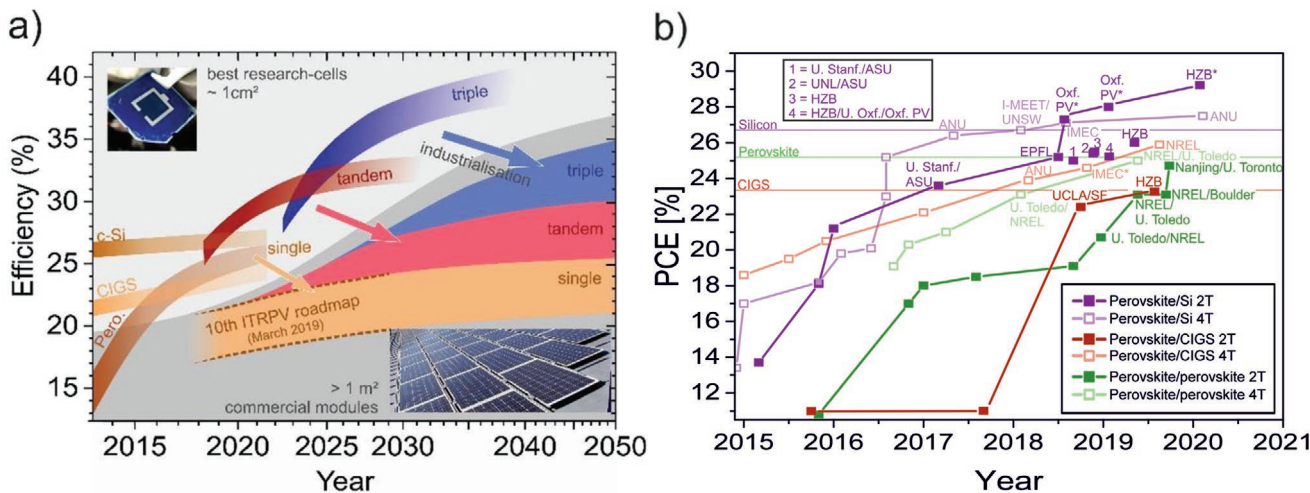


**Figure 1.** a) General outlook of the integration of perovskite-based multi-junctions into highly efficient solar modules based on trends for best reported single and multijunction solar cells as well as predictions from roadmaps. The figure is an update from Albrecht and Rech<sup>[41]</sup>; b) Efficiency evolution from press releases (marked with \*) or published papers for perovskite based tandem solar cells in 2-terminal (2T) and 4-terminal (4T) configuration with Silicon (Si), Cu(In,Ga)Se<sub>2</sub> (CIGS), or perovskite bottom cells. The most recent 2T tandem data can be found in Table 1.

for vertical charge transport. With the latter, lower parasitic absorption and thus higher PCEs could practically be realized. A detailed explanation of the various tandem architectures and a comparison can be found elsewhere.<sup>[8]</sup>

All three monolithic tandem technologies reviewed here were first reported in 2015 and underwent a fascinating improvement within this 4 year timescale. With PCEs between 11% (perovskite/CIGS and all-perovskite) and 14% (perovskite/silicon) in the beginning, all reported first tandem PCEs were well below those of best single-junctions, which is the benchmark for any tandem technology. Recently, the certified PCE for 1 cm<sup>2</sup> active area devices improved to 29.2%, 23.3%, and 22.3% for perovskite/silicon, perovskite/CIGS, and all-perovskite tandems, respectively (see also Table 1). Most 2T tandems were so far reported with silicon as a bottom cell and a steady PCE improvement over time was achieved. Although all three tandem technologies discussed in this review have similarly high-efficiency potentials (see Section 5), the development for perovskite/CIGS and all-perovskite tandem cells was delayed and only recently highly promising results were achieved. The developments in engineering and improved scientific understanding of 2T tandems are described in more detail in Section 3.

With this review, we primarily focus on monolithic perovskite/silicon, perovskite/CIGS, and all-perovskite tandem solar cells. We briefly review the development toward the present status in terms of PCE and device designs and summarize their main scientific and engineering challenges. To overcome these challenges in the near future, we highlight especially the advanced characterization techniques that are utilized in order to further understand and improve these fascinating devices. An improved understanding of the device level is strongly interlinked with more specific and effective characterization methods that help to identify and consequently reduce specific losses. Thus, we present the most important morphological, electrical, electronical, optical, and optoelectronic device characterization and simulation methods for 2T perovskite tandem

solar cells. Finally, we present and compare different efficiency estimates and strategies to overcome a PCE of 30%. This review thus aims at both providing guidelines for scientists who are new to the field, as well as giving a holistic perspective on 2T tandem devices and suitable characterization techniques for perovskite tandem cell experts.

## 2. Main Scientific and Engineering Challenges for 2T Tandem Solar Cells

A monolithic tandem solar cell is typically made from two sub-cells processed directly on top of each other and connected in series via a recombination contact, also termed interconnection layer. The incident spectrum is shared between the wide bandgap front cell (top cell, as seen from the direction of the incident light) that converts the high energy photons (blue light) at a high photovoltage, and the low bandgap bottom cell converting the NIR photons (bottom cell). With that, a broad range of the incident spectrum is harvested with overall reduced thermalization losses. The reduction of fundamental losses using two (or more) different absorber band gaps, increases the theoretical efficiency limit significantly: while the Shockley–Queisser (SQ) limit for a single-junction is only ≈33%,<sup>[46]</sup> that of tandem cells is ≈45% and increases with the number of sub-cells to 50%, 54%, and 65% for three, four, and an infinite number of sub-cells, respectively.<sup>[42]</sup> However, to utilize the full theoretical efficiency potential of monolithically integrated multijunction cells, careful engineering of its components is required: the sub-cells need to be properly connected in series via well-functioning recombination layers, so that sub-cell voltages add up and the overall tandem current is close to that of the limiting sub-cell (see Section 2.4). In order to achieve current matching at the highest photocurrents, further processing and design challenges arise, which are summarized in Figure 2 and discussed in short below.

**Table 1.** Summary of the present reported status for 2-terminal perovskite-based tandem solar cells: perovskite/silicon, perovskite/CIGS, and perovskite/perovskite tandems. The data here refer to Figure 1b.

Reference	Abbreviation in Figure 1.	Published [Y/M]	Certified	Area [cm <sup>2</sup> ]	J <sub>SC</sub> [mA cm <sup>-2</sup> ]	FF [%]	V <sub>OC</sub> [V]	PCE [%]	MPP [%]
Perovskite/Silicon									
Sahlí <sup>[38]</sup>	EPFL	2018/06	Y	1.42	19.5	73.2	1.79	25.5	25.2
Bush <sup>[90]</sup>	U. Stan/ASU	2018/08	N	1.00	18.4	77	1.77	25.0	
Chen <sup>[91]</sup>	UNL/ASU	2019/01	N	0.42	17.8	79.4	1.80	25.4	
Jost <sup>[92]</sup>	HZB	2018/10	N	0.77	18.5	78.5	1.76	25.5	
Mazzarella <sup>[93]</sup>	HZB/U.Oxf./Ox PV	2019/02	Y	1.10	19.0	74.6	1.79	25.4	25.2
Nogay <sup>[94]</sup>	EPFL	2019/03	N	1.43	19.5	74.7	1.74	25.4	25.1
Köhnen <sup>[68]</sup>	HZB	2019/05	Y	0.77	17.8	78.6	1.77	25.0	25.0
Köhnen <sup>[68]</sup>	HZB	2019/05	N	0.77	19.2	76.6	1.77	26.0	26.0
Oxford PV <sup>a)</sup>	Ox PV	2018/12	Y	1.03	19.8	78.7	1.80	28.0	
HZB <sup>b)</sup>	HZB	2020/01	Y	1.06					29.2
Perovskite/CIGS									
Han <sup>[63]</sup>	UCLA/SF	2018/08	Y	0.04	17.3	73.1	1.77	22.4	22.4
Jost <sup>[62]</sup>	HZB	2019/02	N	0.78	18.0	75.7	1.59	21.6	21.6
Al-Ashouri <sup>[14]</sup>	HZB	2019/10	Y	1.03	19.2	71.9	1.68	23.3	23.3
Perovskite/Perovskite									
Zhao <sup>[76]</sup>	NREL/U. Toledo	2018/11	N	0.105	14.0	78.1	1.922	21.0	20.7
Tong <sup>[18]</sup>	U. Toledo/NREL	2019/05	N	0.105	15.0	80.3	1.942	23.4	23.1
Palmstrom <sup>[56]</sup>	NREL/Boulder	2019/05	N		16.0	77	1.88	23.1	23.1
Lin <sup>[15]</sup>	Nanjing/U. Toronto	2019/09	Y <sup>c)</sup>	0.073	15.6	81.0	1.965	24.8	24.5
Lin <sup>[15]</sup>	Nanjing/U. Toronto	2019/09	Y	1.05	14.0	82.0	1.945	22.3	

<sup>a)</sup>Unpublished, from<sup>[95]</sup>; <sup>b)</sup>Unpublished, from<sup>[96]</sup>; <sup>c)</sup>Certification laboratory not recognized according to ref. [97].

## 2.1. Recombination Contact

The recombination layer electrically connects both sub-cells in series: when an electron-hole pair is generated in a sub-cell, one carrier type is subsequently extracted through the external contact of this sub-cell (e.g., the electron leaves, through the “negative” terminal of the 2T tandem). To provide overall charge neutrality and thus allow for efficient charge extraction at this external contact, the recombination layer should balance the loss of the electron by providing an effective recombination (annihilation) pathway for the hole that is left behind: it recombines with a photogenerated electron coming from the other sub-cell. Its hole, in turn, is extracted at the external contact of the second sub-cell (the “positive” terminal). On average, one electron is then transported through the complete tandem stack but at a higher voltage due to the series connection. Thus, the recombination layer must provide very good selectivity for the respective charge carriers as well as the favorable energetic alignment for lossless photovoltage addition and low series resistance. Furthermore, it must also provide high optical transparency for the bottom cell (NIR). Previous realizations of monolithic tandem cells employed different types of recombination contacts: amorphous silicon or III-V semiconductors were realized by heavily p- or n-doped layers of the respective absorber material.<sup>[47–52]</sup> For organic tandems, doped organic charge selective layers were used, partially in combination with solution-processed metal oxides.<sup>[53,54]</sup> For perovskite-based tandem solar cells, similar approaches comprising

recombination layers with highly doped TCOs,<sup>[55]</sup> silicon tunnel junctions,<sup>[38]</sup> and organic recombination layers were utilized.<sup>[34]</sup> In some studies, these layers are combined with ultrathin metal layers acting as recombination centers, but at the cost of NIR transparency.<sup>[15]</sup> TCOs such as ITO are deposited from a sputter process. Therefore, also the sputter damage must be considered and eventually, buffer layers must be integrated into the tandem stack<sup>[56,57]</sup> (see Section 2.2). Therefore, an additional function of the recombination layer stack is to act as a buffer layer and protect the first-processed sub-cell from damage from solvents and surface treatments during processing of the second sub-cell.<sup>[58]</sup>

## 2.2. Tandem Integration

When the monolithic tandem stack is fabricated, the properties of the bottom cell restrict the processes for the fabrication of top cell layers, such as required temperature, utilized solvents, and/or the deposition technique itself. This complicates tandem integration, which is the sum of all required processing steps in the monolithic stack that might interfere with each other. For perovskite tandem solar cells with silicon heterojunctions and CIGS, the allowed temperatures for top cell processing are limited, as the bottom cells degrade at temperatures >200 °C due to degradation of the a-Si:H passivation layers.<sup>[59]</sup> Thus, excluding sintering of metal oxides,<sup>[26,28,30]</sup> which is still being used for the highest efficiency single-junction perovskite cells. This challenge was recently overcome by using different

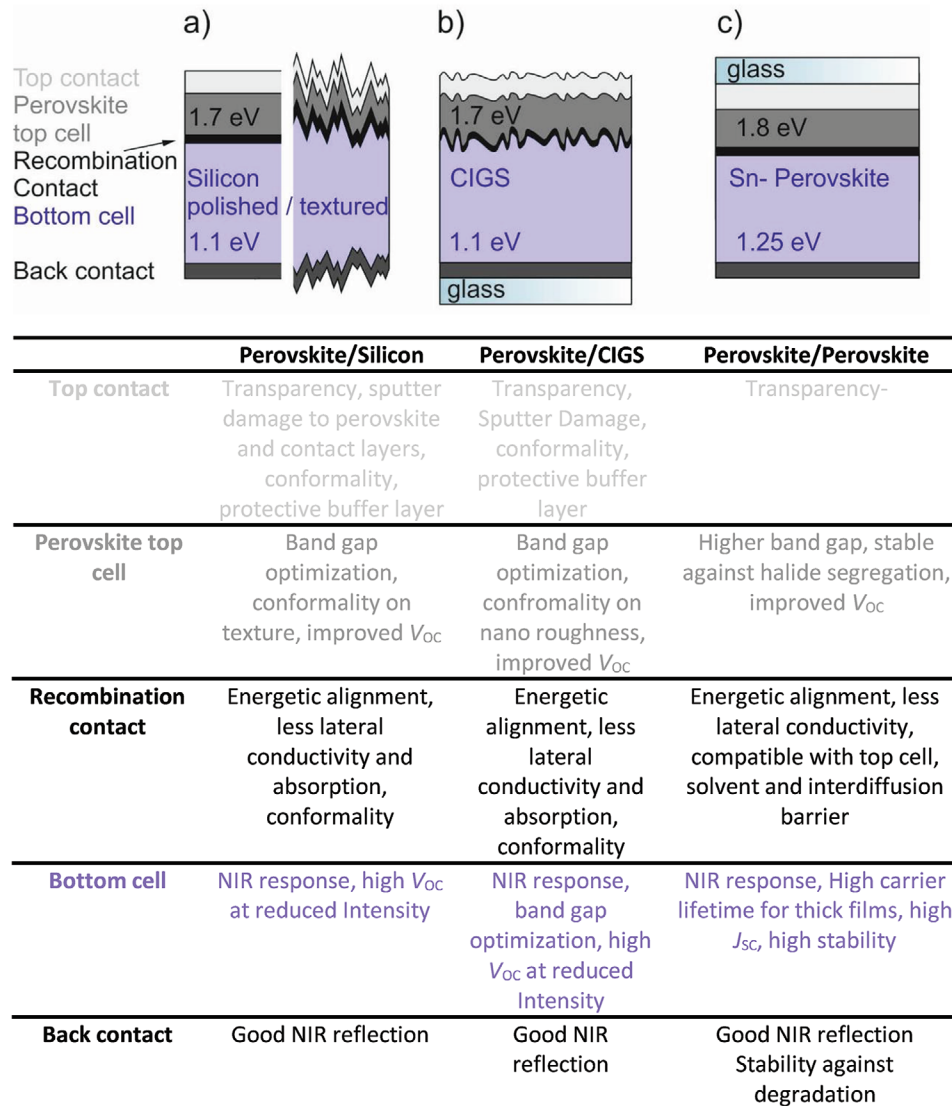


**Figure 2.** Schematic description of monolithic perovskite tandem solar cells with bottom cells made from a) either polished or textured silicon, b) nano-rough CIGS, or c) low band gap (Sn-based) perovskites. The bullet points indicate the scientific and engineering challenges for further development of each tandem architecture.

materials and/or deposition methods such as atomic layer deposition (ALD) for these charge transport layers, and by using different device polarities (p-i-n instead of the regular n-i-p architecture).<sup>[55,60]</sup> For all-perovskite tandem solar cells, the need of solvent resistant buffer layers to ensure stability of the bottom cell against solvents utilized for top cell processing is highly important. Here, metal oxides can be utilized either from solution or from vacuum deposition methods.<sup>[15,56,61]</sup>

### 2.3. Conformal Deposition

Most commonly, perovskite solar cells are fabricated on glass substrates coated with transparent conductive oxide (TCO) of low surface roughness, typically <5 nm), transparent conductive oxide (TCO) coated glass substrates. This allows to use coating

techniques such as spin-coating, inkjet printing, blade, and slot-dye coating. However, as schematically depicted in Figure 2, especially the surface topology and roughness of textured silicon and CIGS may differ strongly from flat. The surface of polished silicon wafers is smoother or similarly rough as typical glass; however, the surface of textured silicon or as grown CIGS is much rough: textured silicon features random pyramids with an angle of 54.7° and typical pyramid heights between several 100 nm and several micrometers, while the surface of typical as grown CIGS absorbers features textures that are rough on the nanoscale, with high root-mean-square (RMS) values and sharp features with high aspect ratio.<sup>[62,63]</sup> For feature heights in the range of or larger than the perovskite absorber thickness (typically 300–800 nm), the deposition method of this layer must be adopted by conformal deposition such as thermal evaporation and hybrid processes between thermal evaporation and

infiltration from solution.<sup>[34,38]</sup> Overcoming the roughness of the substrate can also be done by the utilization of thick perovskite absorber films in the order of one to several microns. These thick films could fully cover rough surfaces or so-called “mild” silicon textures, e.g., small pyramids or photonic light-trapping structures,<sup>[64]</sup> without the need of fully conformal deposition. Several groups have shown that it is possible to fabricate efficient solar cells by growing very thick single crystal-like films<sup>[20,65]</sup> or by inkjet printing thicker films.<sup>[66]</sup> Such thick films could be deposited directly on textured silicon for 2T tandem applications, e.g., by blade coating.<sup>[67]</sup>

The conformal coating of the nanometer thick support layers for the perovskite top cell, especially the thin charge selective layers, must be adapted to this topography by the use of conformal deposition techniques such as ALD,<sup>[62]</sup> thermal evaporation<sup>[34,38]</sup> and/or self-assembly from solution.<sup>[14]</sup> Techniques to determine the morphology and surface coverage will be discussed in the Morphological Characterization section below.

#### 2.4. Current Matching

In order to obtain the maximum power output in a 2T tandem where the sub-cells are interconnected in series, the two sub-cells should operate near current matching, which means that both should generate the same photocurrent. If the photocurrent generation of the sub-cells is imbalanced, the overall tandem current is dictated by the limiting sub-cell and the tandem PCE drops. This is likely to be the case in outdoor operation, where spectral changes occur during the day. However, the current mismatch is partly compensated by the fill factor (FF) increase.<sup>[68]</sup> Thus, the optical design of the monolithic multi-layer stack is highly important to ensure equal photocurrent performance.

#### 2.5. Optical Properties

The monolithic tandem stack consists of two absorber layers, e.g., perovskite and silicon, and several adjacent charge

extraction, contact land antireflection layers. Overall, well over ten layers with different thicknesses and refractive indices play a role in—beneficial—photogeneration and—detrimental—parasitic absorption and reflection. Thus, current matching between the sub-cells at the highest possible photocurrents requires light management strategies that yield an equal distribution of photogeneration in the two sub-cells while minimizing reflection and parasitic absorption losses. Both the optimization of layer stacks in terms of optical properties (refractive indices, film thicknesses) and the implementation of light trapping schemes by, e.g., textured surfaces are crucial for high photocurrents. Optical simulations have become a powerful tool to guide the processing of monolithic tandems toward low parasitic losses and the highest current matching, (see Section 4.2.1).

#### 2.6. Bandgap Tuning

The ability to tune the optical bandgap by manipulating the perovskite composition is one of the most important properties for tandem applications.<sup>[69,70]</sup> The bandgap can be tuned in the range from 1.2 to 2.3 eV by compound engineering.<sup>[71]</sup> However, so far it is not possible to adjust the composition to each bandgap and obtain the highest optoelectronic properties of the film and solar cell stack. **Figure 3** exemplarily presents collected data for the open-circuit voltage ( $V_{OC}$ ) and the short circuit current ( $J_{SC}$ ) as a function of absorption onset or bandgap ( $Eg$ ). The figure includes data from Gharibzadeh,<sup>[72]</sup> Rajagopal,<sup>[73]</sup> as well as Unger et al.<sup>[74]</sup> that were updated with new data from recent reports for the 22–23.7% PCE regime,<sup>[25–30]</sup> the 20–21.6% PCE regime<sup>[75]</sup> in the left figure, and the low bandgap perovskite bottom cell regime in the right figure.<sup>[15,18,76–80]</sup>

The  $V_{OC}$ -to-bandgap loss consists of two contributions, namely, i) the radiative loss due to unavoidable radiative recombination of free charges in the active absorber when being in equilibrium with its surroundings (Shockley-Queisser (SQ) limit, depends on only one material parameter, the band gap), and ii) the nonradiative loss caused primarily by trap-assisted

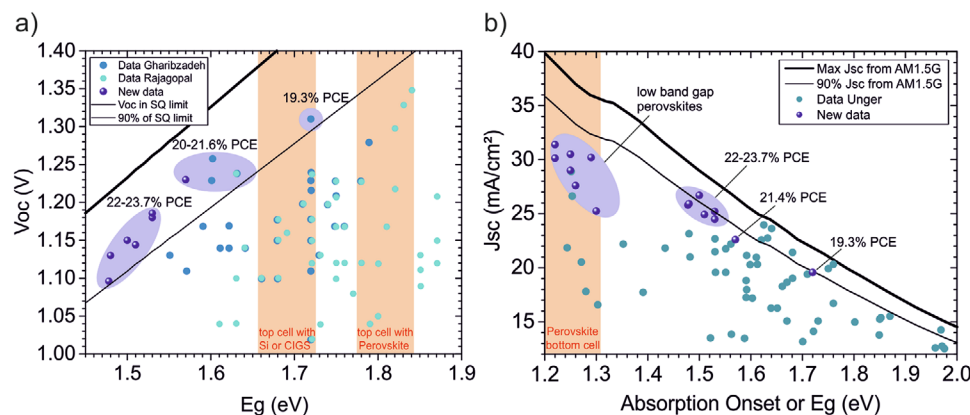


**Figure 3.** a) Open circuit voltage ( $V_{OC}$ ) as function of band gap ( $Eg$ ) or onset of absorption/EQE. The data are merged from Gharibzadeh<sup>[72]</sup> and Rajagopal et al.<sup>[73]</sup> and newer data are added, see text for the references. Orange areas indicate results and their power conversion efficiency (PCE) regime, the orange areas indicate band gap optima for top cells with different bottom cells as indicated. b) Short circuit current ( $J_{SC}$ ) as function of bandgap ( $Eg$ ) or onset of absorption/EQE with data from Unger et al.<sup>[74]</sup> and new data (see references in the text). The orange area indicates the optimum bandgap for perovskite bottom cells.

recombination in the perovskite bulk and at internal interfaces.<sup>[24]</sup> The former defines the radiative limit (SQ limit for perfect absorption quantum efficiency edge)<sup>[81]</sup> in  $V_{OC}$  with the latter reducing the measured  $V_{OC}$  well below. In the plot of experimental  $V_{OC}$ s versus bandgap in Figure 3a, two main features are found. First,  $V_{OC}$  follows the bandgap change in the range between 1.45 and 1.65 eV with high  $V_{OC}$  values well above 90% of the respective SQ limit for each bandgap. However, above 1.65 eV, the  $V_{OC}$  is not increasing linearly with bandgap anymore. For that region, only one value stands out with above 90% of the SQ limit at 1.73 eV.<sup>[72]</sup> At the same time, only one other paper reported high  $V_{OC}$  values (in the presented bandgap range) at bandgap of 1.84 eV that are, however, still well below the 90% SQ limit for this particular bandgap.<sup>[73]</sup> Second, the highest efficiencies well above 20% can only be achieved with the  $V_{OC}$  close to the respective SQ limit and PCEs above 22% are only reported for FAPbI<sub>3</sub> compositions with a bandgap  $\approx$  1.5 eV and below.<sup>[15,18,76–79]</sup> However, for band gaps that are optimized for a tandem top cell, the  $V_{OC}$  values reported so far are well below 90% of the respective SQ limit. This is significantly more loss in  $V_{OC}$  as compared to other bandgap compositions, as indicated by the orange areas in Figure 3a. This is a strong limitation to perovskite-based tandem solar cells. In order to overcome this loss from nonradiative contributions, the perovskite compositions need to be optimized in the near future. Furthermore, a concomitant tuning of the charge selective layers for proper energy level alignment to these optimized perovskites may be required and potential perovskite quantum dot absorbers could also be utilized.<sup>[82]</sup>

Figure 3b displays the short circuit current ( $J_{SC}$ ) as a function of absorption onset or bandgap, compiled from data by Unger et al.<sup>[74]</sup> and newer data (see references above). The bandgap range between 1.45 and 2 eV can generate high currents that are on average 90% of the total available current in the AM 1.5G spectrum for each bandgap. The difference to 100% is due to reflection and parasitic absorption as well as non-perfect absorption onsets. In low bandgap devices that are formed by tin-based perovskites or mixed tin-lead compositions at band gaps around 1.25 eV (orange area), the reported  $J_{SC}$  values are well below the 90% threshold. Comparably short carrier lifetimes that enabled only limited film thicknesses and thus absorption to be used have been considered as a key issue in early reports.<sup>[58]</sup> Recently, higher lifetimes have been reported and external quantum efficiencies improved.<sup>[15,18]</sup> However, the  $J_{SC}$  values for low bandgap perovskite bottom cells around 1.25 eV still have to be improved as these devices have  $J_{SC}$ s well below the 90% threshold. Note that most of the high  $J_{SC}$ , high-efficiency values (purple area in Figure 3b) are enabled with n-i-p solar cell configurations while recent low bandgap perovskite single-junctions and most efficient tandems are fabricated in p-i-n configurations.

### 3. Present Status of 2T Perovskite-based Tandem Solar Cells

In this section, the present status of the perovskite-based monolithic tandem solar cells will be summarized. We focus here on the recent best results for three main different tandem

combinations: Perovskite/Silicon; Perovskite/CIGS and Perovskite/perovskite as found in Figure 1b. In addition, the summary of the highest efficiencies, we add some notable reports for perovskite tandem solar cells, showing proof-of-concept solutions such as textured tandem cells, flexible substrates, or fully solution-processed approaches. For more detailed summaries of the PCE evolution, we refer to the following review papers that focus on different aspects of perovskite/silicon tandem cells: earlier publications, e.g., by Chen et al.<sup>[83]</sup> or Eperon et al.<sup>[84]</sup> were more recently followed by updated overviews, e.g., by Werner et al.,<sup>[8]</sup> Tai et al.,<sup>[85]</sup> Torabi et al.,<sup>[86]</sup> or, most recently, by Song et al.,<sup>[87]</sup> Hu et al.,<sup>[88]</sup> and the progress report by Shen et al. In addition, reviews on all-perovskite tandem solar cells by Wang<sup>[89]</sup> and Leijtens et al.<sup>[58]</sup> can be found, however, to the best of our knowledge, there is no in-depth review on perovskite/CIGS tandem solar cells yet.

#### 3.1. 2-Terminal Perovskite/Silicon Tandem Solar Cells

Crystalline silicon (c-Si) solar cells are currently the leading technology in the global PV market, representing 95% of total production in 2017.<sup>[98]</sup> Therefore, out of the different possible bottom cell technologies for perovskite-based tandem cells, silicon receives by far the highest attention. For silicon single-junction solar cells, the so-called passivated emitter rear contact (PERC) technology is the leading mono-crystalline PV technology, with PCEs well above 20% and  $V_{OC}$ s approaching 700 mV. The current record large cells (M2 format, 15.7  $\times$  15.7 cm<sup>2</sup>) is held by LONGi at 24.06%.<sup>[99]</sup> Also, historically, the first perovskite/silicon 2T tandem was realized on a silicon homojunction solar cell processed with classical high-temperature diffusion processes (albeit not a PERC cell).<sup>[100]</sup> However, when it comes to 2T perovskite/silicon tandem cells, interestingly, the focus is not on manufacturing Perovskite/PERC tandems. Instead, much greater efforts are devoted to developing tandem cells based on silicon heterojunction (SHJ) solar cells. The advantage of Si heterojunction cells lies in their very high efficiency, brought about by a very high  $V_{OC}$ : Today's single-junction Si cell record is held by a heterojunction cell with a certified efficiency of 26.6% and a  $V_{OC}$  of 740 mV.<sup>[101]</sup> However, the device was fabricated with interdigitated back contacts, not suitable for 2T applications. For a both-side contacted device, the record is 25.7% for a TOPCon technology.<sup>[102]</sup> Furthermore, due to difficulties to achieve good passivation of textured hole (majority carrier) contacts in PERC cells, these contacts are usually planar: For the hole contacts in PERC cells, a full area passivating stack of SiO<sub>2</sub>/SiN<sub>x</sub> or Al<sub>2</sub>O<sub>3</sub>/SiN<sub>x</sub> is locally opened, and it has been demonstrated, that the passivation quality of both passivation stacks is significantly degraded on textured surfaces, leading to decreased  $V_{OC}$ s.<sup>[103,104]</sup> Top cells that require planar surfaces for deposition, e.g., due to spin-coated layers, thus need to be in n-i-p configuration. Silicon heterojunction solar cells provide more flexibility in this regard and can be used in either polarity.<sup>[105]</sup> Besides, typical silicon heterojunction cells already feature a front side TCO that can serve as the perovskite's bottom contact similarly as in single-junction perovskite solar cells, allowing for relatively simple process integration. On the other hand, as mentioned, diffused

homojunction cells are dominating the PV market, and there is still room for improvement in PCEs: Certified efficiencies of 24.6% have been reported recently on large area ( $244.6\text{ cm}^2$ ) using another high-temperature contact formation approach, the so-called TOPCon/POLO technology.<sup>[106]</sup> In this approach, the surface of the crystalline silicon wafer is first oxidized, and a thin and highly doped polycrystalline silicon film is then formed on top of the silicon oxide layer. The thin  $\text{SiO}_2$  film provides an improved passivation at the interface to the c-Si wafer, yielding higher  $V_{OC}$ s than diffused homojunctions. At the same time, the oxide is thin enough not to impede carrier transport, and in combination with the high doping of the polySi, good carrier selectivity, and high FFs—on par with diffused junctions—can be achieved.<sup>[107,108]</sup>

In the following sections, we will first review 2T perovskite/silicon tandems on PERC and other diffused junction bottom cells, followed by a section focusing on perovskite/SJH 2T-tandems and finally highlighting tandem results on textures wafers.

### 3.1.1. 2T Tandems on PERC- and Other High Temperature Processed Silicon Cells

Mailoa et al. were the first to realize a silicon/perovskite tandem cell in 2015, on an n-type Si homojunction bottom cell with standard diffused junctions.<sup>[109]</sup> A tunnel junction consisting of highly and oppositely doped crystalline silicon layers ( $n^{++}/p^{++}$  junction) was used to interconnect the top and bottom cells, followed by a stack of an ALD-deposited flat  $\text{TiO}_2$  and a mesoporous  $\text{TiO}_2$  film, which served as the perovskite cell's ETL. The perovskite film was  $\text{MAPbI}_3$ , the top contact consisted of Spiro-OMeTAD and a mechanically transferred mesh of silver nanowires. The cell reached a PCE of 13.7%, strongly limited by its low  $V_{OC}$  of 1.58 V and, most importantly, a low  $J_{SC}$  of  $11.5\text{ mA cm}^{-2}$ ; the FF was 75%. An important cause for the limited  $J_{SC}$  was the thick, doped Spiro-OMeTAD film, which leads to an overall parasitic absorption equivalent to a loss in photogeneration current density of  $\approx 8.4\text{ mA cm}^{-2}$ .

In the following year, Werner et al. demonstrated 16.4% efficient cells using  $\text{ZnSnO}$  as a recombination layer, a stack of sputtered, compact  $\text{TiO}_2$  and mesoporous  $\text{TiO}_2$  as ETL, and  $\text{MAPbI}_3$  as top cell absorber.<sup>[109]</sup> As in Mailoa's cell, the HTL

was Spiro-OMeTAD, but the transparent top contact was now formed with evaporated molybdenum oxides ( $\text{MoO}_x$ ) serving as a buffer layer and a sputtered IO:H/ITO top electrode. Again, absorption in Spiro-OMeTAD at wavelengths  $< 400\text{ nm}$  was limiting the photocurrent density, to  $15.3\text{ mA cm}^{-2}$  in this case ( $V_{OC}$  1.64 V, FF 64.8%; cell area  $0.25\text{ cm}^2$ ). In 2017, Wu et al. reported an improved PCE of 22.5% (MPPT) on  $1\text{ cm}^2$  device area (best J-V parameters: PCE 22.8%,  $V_{OC}$  1.75 V,  $J_{SC}$   $17.6\text{ mA cm}^{-2}$ , FF 73.8%).<sup>[110]</sup> While the top cell stack was similar to Werner's device, the homojunction bottom cell featured passivating  $\text{Al}_2\text{O}_3$  and  $\text{SiN}_x$  films with local contact openings and Cr/Pd/Ag point contacts, covered on the front with an ITO blanket layer. Such passivation/point contact schemes are very similar to those in industrial PERC/PERT Si cells. The optical properties of the  $\text{Al}_2\text{O}_3/\text{SiN}_x$  stack were tuned to achieve similar photocurrents in the top and bottom cell, and a textured silicone foil was placed on the cell to further optimize light in coupling.

A year later in 2018, Zheng et al. demonstrated substantially larger devices, again with the same top cell but now with an interconnecting layer of  $\text{SnO}_2$  processed by spin coating from a colloidal precursor and annealing at  $150\text{ }^\circ\text{C}$ , similar to processes used in silicon heterojunction based tandems (see below). A reverse scan PCE of 17.6% and an MPP-tracked PCE of 17.1% were demonstrated on  $16\text{ cm}^2$  device area, whereas on  $4\text{ cm}^2$  a PCE of 21.0% under reverse scanning and a stabilized PCE of 20.5% was shown.<sup>[111]</sup> Later that year, the same group demonstrated a steady-state efficiency of 21.8%, again on  $16\text{ cm}^2$  with  $(\text{FAPbI}_3)_{0.83}(\text{MAPbBr}_3)_{0.17}$  as perovskite.<sup>[112]</sup> In a somewhat different approach, Shen et al. implemented an interconnecting layer stack consisting of  $\approx 54\text{ nm}$  ALD-grown compact  $\text{TiO}_2$ , followed by a mesoporous  $\text{TiO}_2$  layer, on two different high-temperature processed front p/n junctions: their n-type c-Si cells had either a diffused front ( $p+/n$ )c-Si homojunction, or a ( $p+$ ) polysilicon/silicon oxide/(n)c-Si front junction (POLO/TOPCon contact, cf. introduction of this section). The perovskite in the tandem was  $\text{CsRbFAMAPbI}_3\text{Br}_x$  ( $E_g = 1.63\text{ eV}$ ), and the front contact was a “classical” Spiro-OMeTAD/ $\text{MoO}_x$  buffer/sputtered ITO stack. With an antireflection foil, the  $1\text{ cm}^2$  cell with polySi contact reached an MPP-tracked efficiency of 24.1% (best J-V parameters: PCE 24.5%,  $V_{OC}$  1.76 V,  $J_{SC}$   $17.8\text{ mA cm}^{-2}$ , FF 78.1%) whereas the homojunction-based tandem had a PCE of 22.9%.<sup>[113]</sup> The device structure and best AM1.5G J-V data are reproduced in Figure 4.

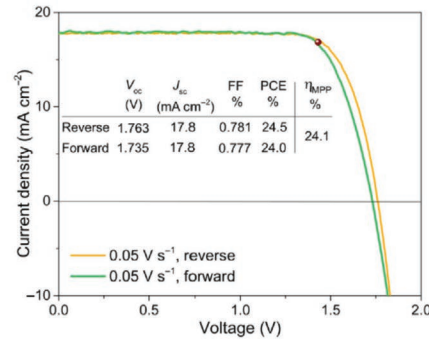
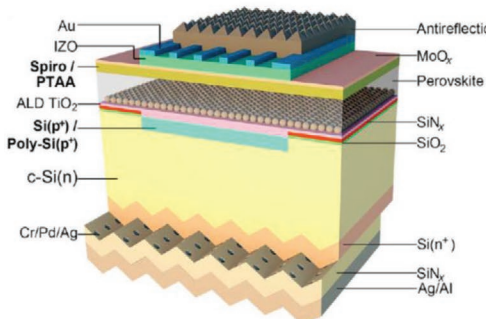


**Figure 4.** Schematic (left) and best J-V curves measured under AM1.5g illumination (right) of the monolithic 2T polySi/perovskite tandem solar cell fabricated by Shen et al. These best cells use PTAA [poly[bis(4-phenyl)(2,4,6-trimethylphenyl)amine]] as the top hole-selective layer instead of Spiro-OMeTAD (Spiro). Reproduced with permission.<sup>[113]</sup> Copyright 2018, The Authors, published by American Association for the Advancement of Science.

Finally, in 2019, Zheng *et al.* published the highest 2T perovskite/silicon-homojunction tandem solar cell PCE on >1 cm<sup>2</sup> device area to date, with a 4 cm<sup>2</sup> cell showing a steady-state efficiency of 23.0% (best J-V parameters: PCE 23.1%, V<sub>OC</sub> 1.73V, J<sub>SC</sub> 16.5 mA cm<sup>-2</sup>, FF 81%). As compared to their earlier devices, the innovation consisted of incorporating a down-shifting phosphor into the PDMS antireflective film, which absorbs UV photons and re-emits green light, however yielding an as yet rather marginal improvement of J<sub>SC,EQE</sub> by ≈0.3 mA cm<sup>-2</sup>.<sup>[114]</sup>

### 3.1.2. 2T Tandems on Silicon Heterojunction Cells

As mentioned above, the majority of efficient perovskite/silicon 2T tandem cells rely on silicon heterojunction (SHJ) bottom cells. In this subsection, we do not aim at a thorough and chronological review of all reported 2T perovskite/SJH results. Instead, we report on the first such devices as well as the current best results, together with a discussion of the most important steps that were taken to reach the current state of the art.

The first monolithically integrated 2T perovskite/silicon heterojunction tandems were demonstrated in 2015 by Albrecht *et al.*<sup>[60]</sup> On an SHJ cell processed from an n-type, double-side polished float zone (FZ) c-Si wafer with a (p,i)a-Si:H front emitter, the p/n recombination junction interconnecting the sub-cells was formed between the (p)a-Si:H film and a layer of indium tin oxide (ITO), i.e., a well-established contact stack for single-junction cells of this type. The perovskite cell was then processed at temperatures below 120 °C in order to avoid degradation of the SHJ cell: the ITO was covered by an ALD-processed SnO<sub>X</sub> film, which was the electron contact of the perovskite sub-cell. With a stack of ≈600 nm thick FAMAPb(I<sub>83</sub>Br<sub>17</sub>)<sub>3</sub> perovskite ( $E_g \approx 1.57$  eV) processed by spin-coating/spin-coated Spiro-OMeTAD as HTL/thermally evaporated MoO<sub>X</sub> buffer/sputtered ITO, the device design followed previously established recipes for semi-transparent single-junction perovskite cells (see, e.g.,<sup>[115]</sup>). A final LiF film was evaporated on top of the ITO as an antireflective coating. On an area of 0.16 cm<sup>2</sup>, a stabilized efficiency of 18.1% could be demonstrated (best J-V parameters: PCE 19.9%, V<sub>OC</sub> 1.79V, J<sub>SC</sub> 14.0 mA cm<sup>-2</sup>, FF 79.5%). At the time, this was the highest reported PCE for a monolithically integrated perovskite/silicon 2T tandem cell. Later that year, Werner *et al.*<sup>[116]</sup> showed an improved efficiency in a similar device: they used an almost identical SHJ cell, but with the front emitter covered by a sputtered indium zinc oxide (IZO). The perovskite top cell, again in n-i-p configuration, consisted of a polyethylenimine (PEIE)/phenyl-C<sub>61</sub>-butyric-acid-methyl-ester (PCBM) bilayer as electron contact, MAPbI<sub>3</sub> as the perovskite absorber, and a top contact of Spiro-OMeTAD/MoO<sub>X</sub> buffer/IO:H/ITO. On 1.22 cm<sup>2</sup>, an MPP-tracked PCE of 19.2% could thus be demonstrated (best J-V parameters: PCE 19.5%, V<sub>OC</sub> 1.70V, J<sub>SC</sub> 16.1 mA cm<sup>-2</sup>, FF 70.9%). On a smaller device of 0.17 cm<sup>2</sup>, a remarkable PCE of 21.2% was reached.

Between these early cells and the current best results, the efficiency of 2T perovskite/SJH tandems has increased by almost one third, and we report here the published results with efficiencies of 25% and above (cf. Table 1). The key achievement toward efficiencies above 25% was the change in tandem polarity from n-i-p top cells with front emitter SHJ bottom

cells to rear junction SHJ and p-i-n top cells first implemented by Bush *et al.* in 2017<sup>[55]</sup>. With that, significantly less parasitic absorption in the n-type front contact could be achieved by thinner and less absorbing layers, as well as a more favorable refractive index grading,<sup>[69]</sup> resulting in a J<sub>SC</sub> of 18.1 mA cm<sup>-2</sup> and PCE of 23.6%.<sup>[55]</sup>

In mid-2018, Bush *et al.* improved this architecture further and demonstrated 25.0% efficient cell with 1 cm<sup>2</sup> active area (V<sub>OC</sub> 1.77V, J<sub>SC</sub> 18.4 mA cm<sup>-2</sup>, FF 77%).<sup>[90]</sup> In their device structure, a front side planar, rear side textured, rear-emitter SHJ cell is paired with a p-i-n type perovskite cell with a cell stack of PTAA as HTM, a 1.68 eV bandgap perovskite (FA<sub>0.75</sub>Cs<sub>0.25</sub>Pb(I<sub>0.8</sub>Br<sub>0.2</sub>)<sub>3</sub>) and a C<sub>60</sub>/SnO<sub>2</sub>/ITO front contact, covered by a polydimethylsiloxane (PDMS) stamped with a random, pyramidal texture to reduce reflection losses, an optical improvement that has been demonstrated before in perovskite/Si tandem<sup>[117]</sup> and Si-based multi-junction devices.<sup>[118,119]</sup> Such textured polymer layers might however not be suitable for rooftop application due to polymer degradation or dust accumulation. Around the same time, Sahli *et al.* published certified cell results for a slightly larger (1.42 cm<sup>2</sup>), 25.5% efficient cell (V<sub>OC</sub> 1.79V, J<sub>SC</sub> 19.5 mA cm<sup>-2</sup>, FF 73.2%) that was also MPP-tracked at 25.2%.<sup>[38]</sup> In this work, the main achievement lies in fabricating a perovskite cell on top of the random pyramid texture of a silicon bottom cell, which is instrumental in achieving the high J<sub>SC</sub> of this device, see upper row of **Figure 5** (details are discussed in Section 3.1.3). Later that year, Jost *et al.* reported devices with a stable 25.5% efficiency (both J-V and MPP-tracked; V<sub>OC</sub> 1.76 V, J<sub>SC</sub> 18.5 mA cm<sup>-2</sup>, FF 78.5%).<sup>[92]</sup> Here, the main findings are a significant improvement in cell efficiency for a front side planar, rear side textured tandem cell, by 2.1%<sub>abs</sub>, through the use of a textured light management (LM) foil. Furthermore, sophisticated simulation studies based on ray tracing are used to demonstrate that the LM foil has significant advantages under diffuse illumination conditions, with potential benefits, e.g., in building-integrated PV. Also in 2018, Oxford PV announced their 28.0% efficient tandem cell (1.03 cm<sup>2</sup> cell area), which was surpassed recently by Helmholtz-Zentrum Berlin (HZB) with a certified efficiency of 29.15% at 1.06 cm<sup>2</sup> active area, being the highest reported certified perovskite tandem efficiency to date.<sup>[96,120]</sup> However, for both results, the scientific publications with all relevant details are not yet published.

In early 2019, Chen *et al.* published a 25.4% efficient 2T perovskite/SJH cell with a V<sub>OC</sub> of 1.80V, but with a different trade-off in V<sub>OC</sub> (and FF) vs. J<sub>SC</sub>. Whereas the FF of 79.4% is among the highest reported so far, the J<sub>SC</sub> is more moderate at 178 mA cm<sup>-2</sup>, optimized for current matching through tuning perovskite bandgap and thickness. The high V<sub>OC</sub> in the wide bandgap triple-cation perovskite absorber (Cs<sub>0.15</sub>(FA<sub>0.83</sub>MA<sub>0.17</sub>)<sub>0.85</sub>Pb(I<sub>0.75</sub>Br<sub>0.25</sub>)<sub>3</sub>, E<sub>g</sub> = 1.64 eV) is achieved by grain engineering through introduction of MACl and MAH<sub>2</sub>PO<sub>2</sub> additives into the perovskite precursor. The addition of MACl enables preferential grain growth and large grain sizes, while MAH<sub>2</sub>PO<sub>2</sub> appears to reduce the trap density at grain boundaries. Later that year, two publications with highly efficient cells followed: Mazzarella *et al.* demonstrated the use of an optical interlayer consisting of nanocrystalline silicon oxide, which has a refractive index of 2.6 (at 800 nm) and therefore

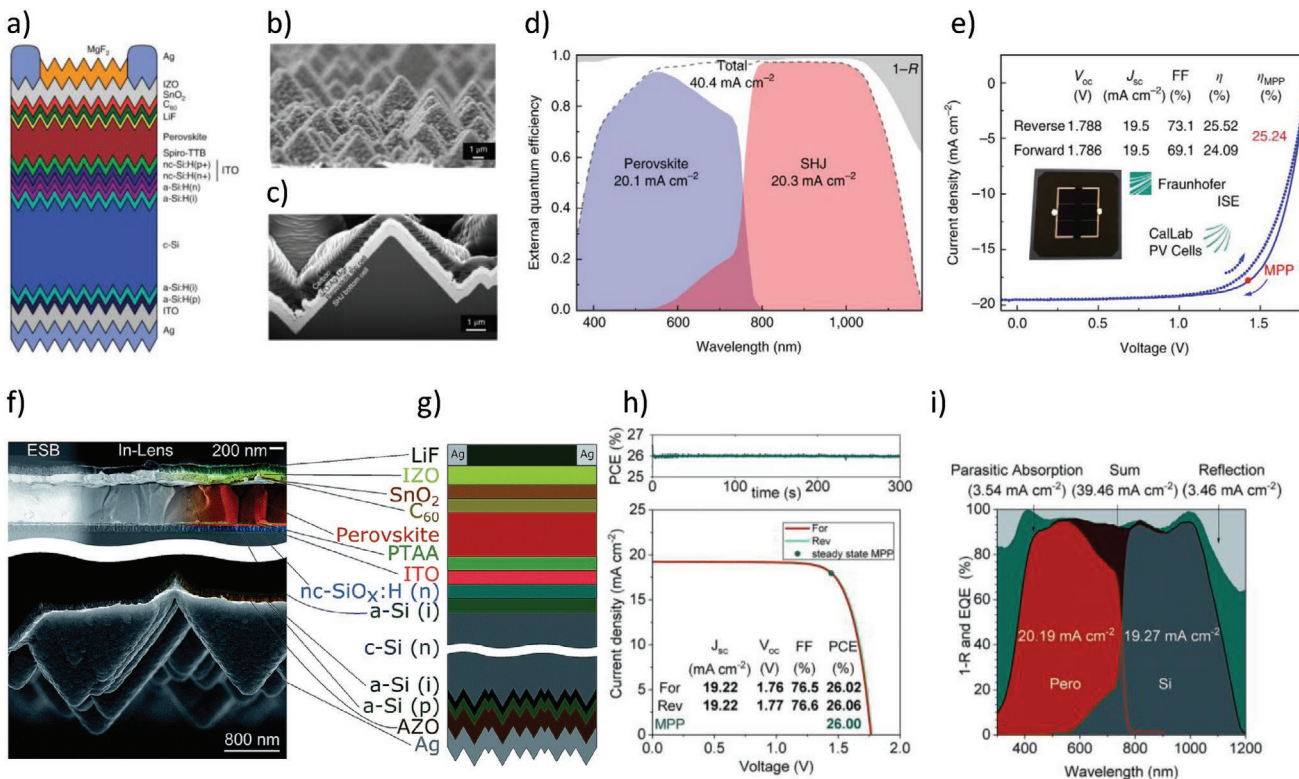


**Figure 5.** Perovskite/silicon heterojunction solar cells with highest published efficiencies to date on both side textured wafers (upper row, Sahli et al., Reproduced with permission.<sup>[38]</sup> Copyright 2018, Springer Nature.) and rear side only textured wafers (lower row, Köhnen et al., Reproduced with permission.<sup>[38]</sup> Copyright 2019, The Royal Society of Chemistry). a) Schematic; b,c) SEM image of the perovskite layer (b) and a cross-section of the full perovskite top cell deposited on the SHJ bottom cell (c); d) EQE and 1-R curve, both excluding front grid losses; e) Corresponding certified J-V data (1.42 cm<sup>2</sup> aperture area, device shown in the inset). Lower row: f) Colored cross-sectional SEM image of the top cell (upper panel) and backside of the bottom cell (lower panel) the tandem cell on single side texture. Note that scale bars in the top and bottom panel are different as indicated; g) schematic device layout; h) J-V-characteristics of the 26% cell (not certified) and 5 min MPP-track; i) EQE and reflection of the same cell with integrated current densities and their sum. Loss in current density due to parasitic absorption (as the difference between sum of the EQE and 1-reflectance) and reflection are also shown.

can help to reduce reflection losses in tandem cells processed on a flat silicon substrate. A current gain of 1.4 mA cm<sup>-2</sup> in the silicon bottom cell is demonstrated, yielding a top cell + bottom cell total current density of 38.7 mA cm<sup>-2</sup> (certified cell parameters: PCE 25.4%, V<sub>OC</sub> 1.79V, J<sub>SC</sub> 19.0 mA cm<sup>-2</sup>, FF 74.6%; MPP-tracked efficiency: 25.2%).<sup>[93]</sup> Nogay et al. reported 25.4% (25.1% MPP-tracked) on a tandem solar cell with 1.43 cm<sup>2</sup> active area (V<sub>OC</sub> 1.74 V, J<sub>SC</sub> 19.5 mA cm<sup>-2</sup>, FF 74.7%). Here, a different type of silicon heterojunction bottom cell was used: Instead of using low-temperature PECVD-grown a-Si:H or nc-Si:H films for the c-Si cell's contacts, a TopCon/POLO/poly-Si-based cell was employed. This is similar to what Shen et al. have reported (see Section 3.1.1,<sup>[113]</sup>), but here, a p-type c-Si substrate was used. A top cell similar to Sahli's from the year before<sup>[38]</sup> was implemented on front-side textured bottom cell: the perovskite was grown on spiro-TTB as HTL with a hybrid method that combines the co-evaporation of CsBr and PbI<sub>2</sub>, before spin-coating an organo-halide solution and annealing at 150 °C. The planar back-side was utilized for better passivation as described above. Finally, the currently highest PCE reported in a scientific publication was achieved by Köhnen et al., at 26.0%, both in J-V and MPP-tracked (V<sub>OC</sub> 1.77V, J<sub>SC</sub> 19.2 mA cm<sup>-2</sup>, FF 76.6%).<sup>[68]</sup> The tandem combines a triple cation, mixed halide

perovskite, Cs<sub>0.05</sub>(MA<sub>0.17</sub>FA<sub>0.83</sub>)Pb(I<sub>0.83</sub>Br<sub>0.17</sub>)<sub>3</sub> in a p-i-n configuration (HTL:PTAA; ETL:C<sub>60</sub>, covered with SnO<sub>2</sub> and IZO front electrode) with a rear emitter, rear side textured SHJ cell fabricated from an (n)c-Si wafer, cf. the lower row of Figure 5. The main scientific achievement in this work lies in elucidating the mutual dependency of J<sub>SC</sub> and FF though current matching in the perovskite/silicon tandem. As evidenced through both experiments and simulations, the reduced J<sub>SC</sub> in unmatched conditions is partially compensated by an enhancement of the FF. This will be discussed in more detail in the characterization section below.

Up to this point, small perovskite/Si tandems with typical sizes  $\approx$ 1 cm<sup>2</sup> have been discussed. However, upscaling of the reported high efficiencies to industrially viable large areas is an important challenge. Not many attempts at upscaling beyond 10 cm<sup>2</sup> have been reported to date. We have mentioned Zheng's 17.1% efficient perovskite/silicon homojunction cell in the previous section. For comparison, the highest efficiency for large perovskite/SJH cells is 22.6% on 57.4 cm<sup>2</sup> (J-V: PCE 22.6%, V<sub>OC</sub> 1.72 V, J<sub>SC</sub> 17.5 mA cm<sup>-2</sup>, FF 75%), reported in 2019 by Kamino et al.<sup>[121]</sup> Here, the main achievement lies not only in the impressive tandem cell size—a “full area” cell was manufactured from a 4” wafer, which was cut to a pseudosquare

shape—but in implementing a front side metal grid using a low-temperature silver paste applied by screen-printing. Also, for small-area tandem devices with such printed front metallization, only minimal thermal degradation is demonstrated when annealed up to 140 °C in air, resulting in silver bulk resistivity of  $<1 \times 10^{-5} \Omega \text{ cm}$ .

### 3.1.3. Results on textured Silicon Wafers

Efficient light trapping in single-junction silicon solar cells is implemented by texturing the c-Si wafer during saw damage etching. For monocrystalline silicon, random pyramid textures with a height and base length of a few micrometers are typically used.<sup>[122]</sup> However, such feature sizes are incompatible with the usual spin-coating processes used in perovskite top cell manufacturing with typical thicknesses of well below 100 nm for the charge selective layers. Therefore, additional chemical and/or mechanical polishing is required to planarize the Si surface and enable perovskite spin coating atop.<sup>[123]</sup>

There are relatively few reports on implementing perovskite cells on bottom cells with random pyramid textures on both wafer sides, despite the potential advantages not only in optical properties, but also in terms of process compatibility to standard silicon cell technology. As mentioned already briefly above, the first and only cell was reported in 2018, by Sahli et al.<sup>[38]</sup> (Figure 5, upper row). They fabricated their perovskite top cell in a p-i-n configuration, using thermally evaporated 2,2',7,7'-tetra(N,N-di-tolyl)amino-9,9-spiro-bifluorene (Spiro-TTB) as the HTL. Interestingly, they find that this also requires them to change from standard ITO as the final film of the SHJ to an (n<sup>+</sup>/p<sup>+</sup>)nc-Si:H junction: On the ITO, no conformal coating by Spiro-TTB could be achieved, whereas it was possible on the (p<sup>+</sup>)nc-Si:H film. To achieve a conformal coating of the perovskite film, they used a hybrid process<sup>[124]</sup> consisting of first co-evaporating the inorganic species PbI<sub>2</sub> and CsBr to form a porous film, which was then infiltrated by a spin-coated solution of FAI and FABr and annealed at 150 °C to form the Cs<sub>x</sub>FA<sub>1-x</sub>Pb(I,Br)<sub>3</sub> perovskite film ( $E_g = 1.65 \text{ eV}$ ). Interestingly, spin coating the organic components on top of the textured and conformally covered (with PbI<sub>2</sub> and CsBr) wafer yields a conformal perovskite film. The top contact consisted of thermally evaporated LiF/C<sub>60</sub>/SnO<sub>2</sub> and a sputtered IZO front electrode; an additional MgF<sub>2</sub> film further reduced reflection losses. The final tandem cell has a certified MPP-tracked PCE of 25.2% (J-V scan: PCE 25.5%,  $V_{OC}$  1.79 V,  $J_{SC}$  19.5 mA cm<sup>-2</sup>, FF 73.1%). Indeed, the reflection losses are minimal between 400 and 1100 nm (Figure 5d), and the EQE shows low parasitic losses as well as a good current matching between the sub-cells. In revision phase of this review paper, Chen et al. reported on blade coating of perovskite absorber layers on top of sub-micron textured silicon bottom cells. The mild texture enabled coating of completely covering and planarizing perovskite films and a remarkable monolithic tandem efficiency of 26.1% (J-V scan: PCE 26.2%,  $V_{OC}$  1.82 V,  $J_{SC}$  19.2 mA cm<sup>-2</sup>, FF 75.3%).

Regarding light trapping at the silicon cell's rear side, the perovskite cell process poses no constraints. Therefore, standard texturing processes can be used on the rear side, and indeed, most of today's perovskite/SHJ tandem cells are

processed on rear side textured, front side polished wafers, thus combining beneficial light trapping in the IR with ease of fabrication for the perovskite cell. The first simulation studies of 2T perovskite/SHJ tandems with such a random pyramid textured rear side were published in 2016: Jost et al. estimated a possible current density gain by  $\approx 0.7 \text{ mA cm}^{-2}$  if a rear side texture is present,<sup>[125]</sup> and Santbergen et al. came to similar conclusions, predicting a matched photocurrent density of 18.6 mA cm<sup>-2</sup> for front side flat/rear side textured cells.<sup>[126]</sup> Later that year, Werner et al. indeed demonstrated experimentally a gain of 0.77 mA cm<sup>-2</sup> by implementing such a texture.<sup>[127]</sup> More recently, Jost et al. carried out more sophisticated optical simulations of perovskite/SHJ tandems on flat, rear side and both side textured silicon wafers, also considering an optimization of the perovskite bandgap.<sup>[92]</sup> They find, a difference of  $\approx 0.5 \text{ mA cm}^{-2}$  in photocurrent density between optimized rear side texture and a double side textured cell, cf. section "optical simulation" below for more details.

### 3.2. 2T Perovskite/CIGS Tandem Solar Cells

Another interesting candidate for the application as a bottom cell is CIGS (Cu(In,Ga)Se<sub>2</sub> or similar chalcopyrites). It is a well-established technology, having around 2% of the PV market<sup>[98]</sup> in 2017 with the module fabrication almost doubling in 2018. With the bottom cell being available in market, this makes CIGS a relevant technology in the scope of perovskite-based tandem solar cell research.

CIGS, similarly to silicon, has an almost perfect bandgap for the bottom cell of 1.1 eV that can be tuned by compositional engineering, as for perovskites.<sup>[128]</sup> The bandgap can be lowered down to 1 eV, which is more advantageous for tandem applications, compared to a perovskite (yet reported) and silicon limit of 1.25 eV and 1.1 eV, respectively. Due to the direct bandgap of CIGS and the resulting significantly reduced absorber thicknesses, the technology enables low material and energy consumption. A combination of perovskite and CIGS could, therefore, enable an all thin-film tandem technology with high PCE at low costs. The current CIGS single-junction solar cell PCE record is 23.35%,<sup>[95]</sup> which is lower than the PCE of the best silicon devices. Consequently, the energy yield simulations have shown that compared to perovskite/Si tandem solar cells, the perovskite/CIGS tandem devices have an estimated 10% lower yearly energy yield.<sup>[129,130]</sup> Nevertheless, if the deposition of highest quality perovskite absorber on top of the pyramidal texture proves to be too challenging, front-side polished silicon substrates will have to be used. There, the highest PCE obtained is 22.1%,<sup>[131]</sup> thus lower than for the CIGS. At the same time, there are some advantages of CIGS over silicon-based tandem solar cells. Both CIGS and perovskite are thin-film technologies, which allows the fabrication of flexible devices with a high power-to-weight ratio. Both are also proton radiation hard and therefore suitable for space applications.<sup>[132,133]</sup> Additionally, since the configuration and processing of perovskite top cell are similar for both silicon and CIGS, the added PCE due to a tandem might reduce the relative cost difference between silicon and CIGS, going from single-junction to tandem architecture.

The typical device structure of CIGS is substrate/Mo/CIGS/CdS/ZnO, where CIGS/CdS forms a p-n junction. Due to this defined polarity, only the p-i-n (inverted) perovskite solar cell configuration can be used in monolithic tandem devices (compared to silicon where depending on the silicon wafer doping and the contact polarity, both p-i-n and n-i-p perovskite top cells can be used). Nevertheless, this is rather a smaller issue as due to lower optical losses, the p-i-n top cell configuration is preferable at the moment in perovskite-based tandem solar cells (see above).

Overall, only a few reports on monolithic perovskite/CIGS tandem solar cells can be found in the literature, with best ones stated in Table 1. There are several reasons for that, such as polarity restrictions, and processing restrictions, namely CIGS temperature limit of around 200 °C due to Cd diffusion into CIGS absorber at high temperatures.<sup>[134]</sup> Finally and most importantly, the deposition of CIGS absorber results in a relatively rough surface, in the range of  $\sigma_{\text{RMS}} = 50\text{--}200 \text{ nm}$ , with typical lateral feature sizes in the order of 500 nm to 1  $\mu\text{m}$ , depending on the details of the processing.<sup>[135,136]</sup> While the perovskite absorber is thick enough to fully cover the nano-rough surface, high-performance hole selective layer for the top perovskite cell, commonly deposited from solution, is not. This results in a high probability of shunting the top cell, making fabrication of a monolithic perovskite/CIGS tandem very challenging. Thus only three reports have been published with above 20% efficiency for this tandem technology, see Table 1.

The first monolithic perovskite/CIGS tandem device reported a PCE of 11%.<sup>[137]</sup> This tandem was enabled by a bottom cell being processed from solution instead of typical sputtering or co-evaporation processes, thus reducing the surface roughness. As a hole selective layer between top and bottom cell a thick PEDOT:PSS was used, further smoothening the surface. While this protected the top cell from shunting, the overall tandem cell performance might have suffered from reduced  $V_{\text{OC}}$  due to the PEDOT:PSS/perovskite interface.<sup>[138]</sup> Similar approaches were also adopted: fabricating copper indium di-selenide (CIS) by electrodeposition or spin-coating resulted in a smoother bottom cell surface and enabled monolithic tandem solar cell PCEs of 11.0% and 8.55%, respectively.<sup>[139,140]</sup> Both devices were also fabricated with PEDOT:PSS as a hole selective layer.

Recently, three reports on highly efficient monolithic perovskite/CIGS tandem solar cells have been presented, where the tandem PCE is higher than the PCE of single-junction sub-cells. Han et al. presented a solution similar to the one used in perovskite/silicon devices, where the front surface is polished to obtain a flat surface.<sup>[63]</sup> They sputtered a thick ITO recombination layers on top of the CIGS bottom cell and polished it to reduce roughness as shown in Figure 7a. In this way, the spin-coating of perovskite and very thin contact layers can be implemented without losses due to surface roughness. Consequently, a PCE of 20.8% on 0.52  $\text{cm}^2$  was obtained and a certified PCE of 22.4% on 0.042  $\text{cm}^2$  (Figure 6a). The device benefits from a high  $V_{\text{OC}}$  of 1.78 V. This is, to the best of our knowledge, the only report for perovskite/CIGS tandems where the  $V_{\text{OC}}$  of the tandem is exactly equal to the sum of  $V_{\text{OC}}$ s of the sub-cells. Due to the deposition of thick ITO recombination layer, the free carrier absorption increases in the NIR, reducing the current

generated in the bottom CIGS sub-cell, as seen by low  $J_{\text{SC}}$  of only 17.3  $\text{mA cm}^{-2}$  in the tandem device.

Jošt et al. chose a different way. Instead of polishing to obtain flat surface, they conformally deposited a hole transport layer directly on top of the as-grown rough CIGS surface.<sup>[62]</sup> Ten nanometers of ALD grown  $\text{NiO}_x$  was enough to form a conformal, closed layer as confirmed by TEM cross-section measurement (Figure 6b) while the spin-coated polymer PTAA with nominal thickness of 10 nm on flat surfaces agglomerated in the valleys and did not cover the peaks of the rough surface of the bottom cell. The JV measurements of their devices are shown in Figure 6b. The  $\text{NiO}_x$  prevented shunting of the top cell and a  $\text{NiO}_x$ -only device resulted in a PCE of 18.0%. Despite the PTAA not covering all the peaks on the surface, as confirmed by a poor performance of PTAA-only device, the inclusion of PTAA on top of  $\text{NiO}_x$  ( $\text{NiO}_x/\text{PTAA}$  bilayer) improved the detrimental  $\text{NiO}_x/\text{perovskite}$  interface. This enabled the PCE of 21.6% on an area of 0.78  $\text{cm}^2$ . The obtained current was higher than in,<sup>[63]</sup> despite a strong mismatch between the sub-cells, owing to much lower parasitic absorption in the recombination layer, and to rough front contact surface that was induced by the rough bottom cell reducing the overall reflection. The downside of the device is a  $V_{\text{OC}}$  of below 1.6 V.

Al-Ashouri et al.<sup>[14]</sup> took the idea about conformally deposited layers even further. They designed self-assembled monolayer (SAM) acting as the hole selective layer that binds to oxide surfaces (e.g., ITO, ZnO). Despite being only a single molecular layer, the strong binding affinity and self-assembly ensures closed layers even on rough surfaces. The almost lossless SAM/perovskite interface additionally resulted in an improved  $V_{\text{OC}}$ , which, combined with improved current management, yielded a certified current record PCE for perovskite/CIGS tandems of 23.3% on a  $>1 \text{ cm}^2$  area (Figure 6d).

Finally, Fu et al.<sup>[141]</sup> presented a proof-of-concept perovskite/CIGS flexible tandem solar cell. The device reached a decent  $V_{\text{OC}}$  of 1.75 V, however, the PCE was limited to 13.2% due to a low FF of 46%. (Figure 6c). The main reason for lower FF was most likely not connected to the flexible design, but originates from non-closed spin-coated PTAA, resulting in a low shunt resistance. Potentially, a different HTL, such as SAM or ALD deposited NiO could be used, possibly resulting in high PCEs also in flexible tandem devices.

The results above show that perovskite/CIGS tandem solar cells also have great potential for different applications. Assuming best JV parameters from the publications described above,  $J_{\text{SC}}$  of 19.2  $\text{mA cm}^{-2}$ ,<sup>[14]</sup>  $V_{\text{OC}}$  of 1.78 V,<sup>[63]</sup> and 75.7% FF,<sup>[62]</sup> a PCE of 25.9% should realistically already be reachable, approaching the PCEs obtained in perovskite/silicon tandems. Combined with radiation hardness and flexibility there is a broad range of applications where perovskite/CIGS tandems could have an advantage over perovskite/silicon devices.

### 3.3. 2T Perovskite/Perovskite Tandem Solar Cells

In the previous two sections, we discussed perovskite tandems in combination with two well-established inorganic PV technologies. However, by tuning the perovskite bandgap, also two perovskite absorbers can be combined to form **all-perovskite**

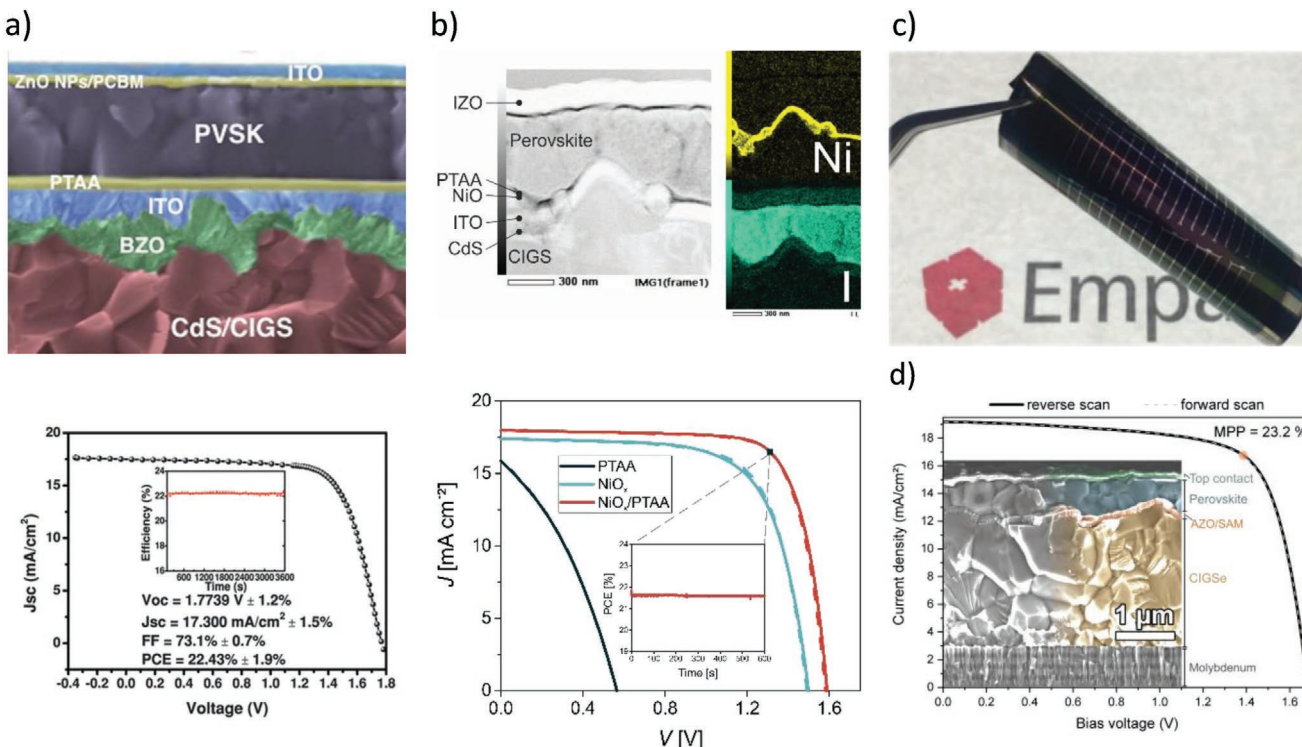


**Figure 6.** Best performing perovskite/CIGS tandems. a) perovskite/CIGS tandem enabled by deposition of thick recombination ITO layer and subsequent polishing. top: the SEM cross-section image where polishing process can be easily distinguished. Bottom: certified J–V measurement. Reproduced with permission.<sup>[63]</sup> Copyright 2018, American Association for the Advancement of Science. b) perovskite/CIGS tandem enabled by conformal deposition of NiO hole transport layer via ALD. top: TEM cross-section images showing conformal coating of NiO on top of rough surface. Bottom: J–V measurements with different hole transport combinations (PTAA-only, NiO-only and PTAA/NiO bilayer). Reproduced with permission.<sup>[62]</sup> Copyright 2019, ACS Publications. c) Photo of a proof-of-concept of a flexible perovskite/CIGS solar cell. Reproduced with permission.<sup>[141]</sup> Copyright 2018, Wiley-VCH. d) Perovskite/CIGS tandem enabled by conformal coating of a self-assembled monolayer on the rough ZnO surface. Reproduced with permission.<sup>[14]</sup> Copyright 2019, Royal Society of Chemistry.

tandem solar cells. In addition, perovskite/organic photovoltaic devices have been realized. Similar to CIGS, these tandem solar cells can be manufactured by low-temperature thin-film deposition techniques that enable light-weight, flexible devices and high throughput production. However, the all-perovskite tandem solar cells make use of the broad bandgap tunability of both sub-cells and the unprecedented progress in single-junction device efficiencies. In addition, cheap and simple fabrication methods for the absorber such as blade coating or ink-jet printing might offer a cost advantage over the previously introduced tandem technologies.<sup>[142–144]</sup>

As discussed in Section 2.2, a critical engineering challenge is to prevent bottom cell damage during top cell processing. This particularly accounts for all-perovskite tandems due to their lower chemical stability as compared to Si or CIGS, especially regarding their thermal budget and solubility in diverse solvents. Similarly to silicon heterojunction and CIGS, also perovskite bottom cells are restricted to processing temperatures below 200 °C. This again requires all contact layers to be deposited at low temperatures. So far this has been realized in all-perovskite tandem solar cells both for n-i-p<sup>[34,77,145,146]</sup> and p-i-n<sup>[15,56,76,78,147,148]</sup> sub-cell architectures, with the latter one being employed more frequently and having achieved the highest efficiencies so far. Typically utilized low-temperature contacts are evaporated C<sub>60</sub> or spin-coated PCBM as electron

and spin-coated PEDOT:PSS or PTAA as hole selective contacts, respectively.

Concerning the solubility of the bottom cell, several strategies have been presented: i) lamination of two individual subcells by sandwiching the substrates facing towards another with their contacts touching.<sup>[150]</sup> ii) Solvent-free fabrication of the top cell by vacuum deposition.<sup>[34,145]</sup> iii) Utilization of orthogonal solvent systems for the top stack. For example, fully solution-processed 2T all-perovskite triple junction tandem solar cells have been enabled with the perovskite being deposited from an acetonitrile/MA based solvent system.<sup>[45]</sup> iv) The most frequently used method: introduction of chemically resilient barrier layers on top of the bottom cell to provide sufficient protection during the subsequent processing. Such buffer layers have been realized in form of photo-cross-linked polymers,<sup>[77]</sup> film transfer-laminated PEDOT:PSS<sup>[146]</sup> or TCO layers, mostly from sputter deposition.<sup>[18,56,76,147,148]</sup>

The TCO layers typically also feature the recombination contacts of the tandem stack, thereby resolving the second engineering challenge as introduced in Section 2.1. Although few reports have shown direct sputter deposition of TCOs on perovskite cells,<sup>[148,150]</sup> an additional buffer layer such as ALD-deposited SnO<sub>2</sub>,<sup>[78,80,147]</sup> AZO,<sup>[56]</sup> or an evaporated Ag/MoO<sub>x</sub> layer stack<sup>[76]</sup> is often required to protect organic layers from sputter damage. Alternatively, sputter-free recombination layers

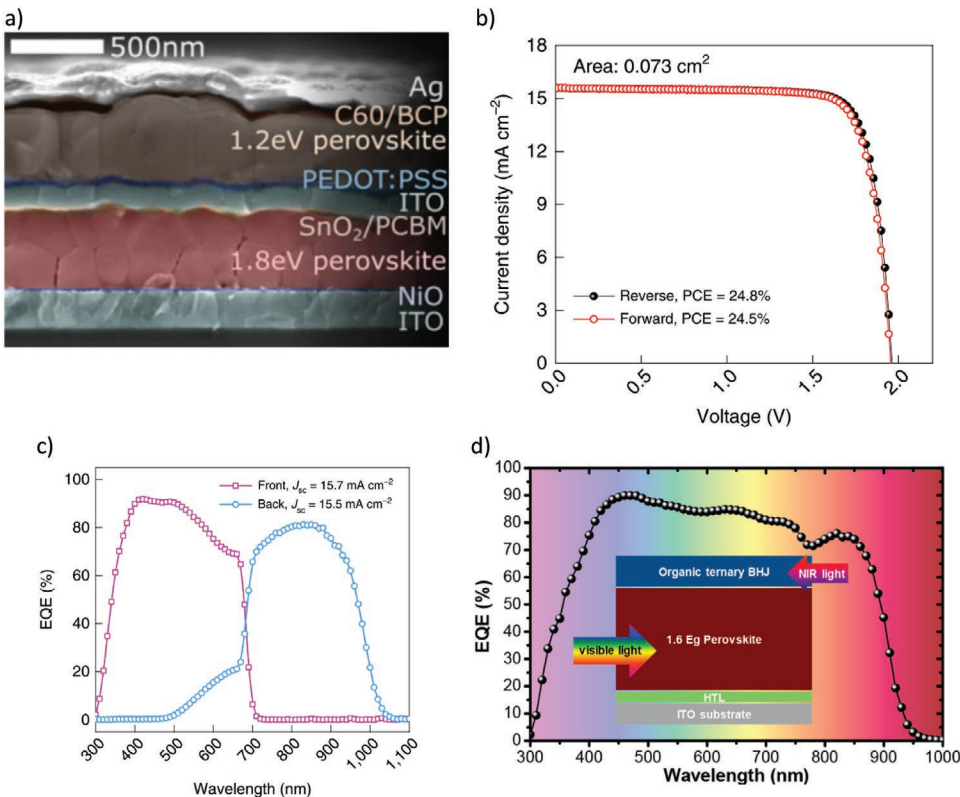


**Figure 7.** a) Scanning electron microscopy image of a monolithic perovskite-perovskite tandem solar cell, comprising a Sn-Pb mixed absorber ( $\text{FA}_{0.75}\text{Cs}_{0.25}\text{Sn}_{0.5}\text{Pb}_{0.5}\text{I}_3$ ) with a low bandgap of 1.2 eV as bottom cell and a 1.8 eV wide band gap top cell from  $\text{FA}_{0.83}\text{Cs}_{0.17}\text{Pb}(\text{I}_{0.5}\text{Br}_{0.5})_3$ . Reproduced with permission.<sup>[147]</sup> Copyright 2016, American Association for the Advancement of Science. b) Current–voltage characteristics of the current best-performing monolithic all-perovskite tandem solar cell under one-sun illumination and c) corresponding EQEs of the top and bottom cells. Reproduced with permission.<sup>[155]</sup> Copyright 2019, Nature Publishing Group. d) Device schematic and external quantum efficiency (EQE) of a two-terminal multi-junction device comprising a 1.6 eV perovskite absorber and an organic bulk heterojunction (BHJ) solar cell without recombination layer between the two sub-cells. Reproduced with permission.<sup>[155]</sup> Copyright 2019, American Chemical Society.

from ALD-SnO<sub>2</sub>/Au/PEDOT:PSS stacks were shown to provide excellent electrical functioning and chemical resilience.<sup>[15]</sup> However, comprising thin metal layers in the tandem device also induces considerable parasitic absorption losses and thus impairs the quantum yield. Further, metal layers were shown to hamper the device stability either due to corrosion by ions from the perovskite layer<sup>[151,152]</sup> or due to metal diffusion into the absorber.<sup>[153,154]</sup> Alternatively, also recombination junctions from highly doped organic layers have been realized.<sup>[14,77,145,146]</sup>

First all-perovskite tandem solar cells were demonstrated in late 2015, with PCE values of 6.6%<sup>[146]</sup> and 10.4%.<sup>[149]</sup> The main limitation of these cells stems from poor light harvesting with tandem  $J_{SC}$  values below 10  $\text{mA cm}^{-2}$ . The cells comprised absorber layers of MAPbI<sub>3</sub> and MAPbBr<sub>3</sub> with bandgap energies of around 1.55 and 2.25 eV, respectively. As discussed before, combinations of such large band gaps are unfavorable for application in tandem solar cells and wide parts of the solar spectrum were simply not being absorbed.

Lower band gaps for bottom cells, below 1.5 eV, can be realized by Pb-Sn mixed perovskites, as mentioned in Section 2.6. The minimum bandgap of around 1.2 eV can be achieved for Sn contents in the range of 60–80 mol% with respect to the sum of Pb and Sn in the composition.<sup>[156,157]</sup> The absorber bandgap increases again for higher amounts of Sn. This nonlinearity

is referred to as bandgap bowing. Due to this bowing effect, a wide range of Pb-Sn mixed perovskite compositions can enable low band gaps  $\approx 1.22\text{--}1.25$  eV.<sup>[156–158]</sup> Note, that reported optical band gaps can strongly depend on the utilized measurement technique, as discussed in detail by Wang et al.<sup>[159]</sup> They can range, e.g., from 1.17<sup>[159]</sup> to 1.24 eV<sup>[157]</sup> for  $\text{MAPb}_{0.5}\text{Sn}_{0.5}\text{I}_3$ . However, for a bottom cell bandgap in the range of 1.22–1.25 eV, the ideal top cell would have an  $E_g$  of  $\approx 1.75\text{--}1.85$  eV. Yet, as depicted in Figure 3a, such wide-bandgap perovskites as well as low-bandgap compositions often suffer from higher nonradiative  $V_{OC}$  losses. Regarding the Pb-Sn mixtures, large defect densities and nonradiative recombination losses in perovskite thin films are widely attributable to oxidation of  $\text{Sn}^{2+}$  to  $\text{Sn}^{4+}$  resulting in high background hole densities and short carrier lifetimes.<sup>[15,89]</sup> For wide-bandgap perovskites in the range of 1.75–1.85 eV, photo-induced halide segregation, Br-related trap states, and non-optimized contact layers are considered as the main origins of voltage losses.<sup>[58,74,160,161]</sup>

In 2016, Eperon, Leijtens et al. were the first to utilize a Pb-Sn mixed perovskite ( $\text{FA}_{0.75}\text{Cs}_{0.25}\text{Sn}_{0.5}\text{Pb}_{0.5}\text{I}_3$ ) with a low bandgap of 1.2 eV to extend the spectral absorption range in all-perovskite tandems to wavelengths above 1000 nm (device structure depicted in Figure 7a).<sup>[147]</sup> While the tandem  $J_{SC}$  was enhanced to 14.5  $\text{mA cm}^{-2}$ ,  $V_{OC}$  (1.66 V) and FF (70%) strongly

limited the overall PCE (17.0%). Subsequent works thus focused on reducing the defect densities in the low-bandgap perovskites. Recent publications managed to substantially reduce the defect densities in Pb-Sn mixed perovskites and suppress Sn<sup>2+</sup> oxidation by adding chlorine,<sup>[76]</sup> CdI<sub>2</sub>,<sup>[80]</sup> guanidinium thiocyanate (GuaSCN),<sup>[18]</sup> or metallic tin<sup>[15]</sup> to the perovskite precursor solution or by post-deposition treatment of absorber films with MACl vapor.<sup>[78]</sup> This enabled high-quality absorbers with large grains and diffusion lengths above 3 μm, resulting in single-junction solar cell PCEs above 20%. Additionally, the long diffusion lengths also allowed to increase the absorber thickness to above 700 nm and thus enhanced IR light harvesting and consequently the  $J_{SC}$  of low bandgap perovskite cells as highlighted before in Figure 3b. Also highly efficient all-perovskite tandem solar cells were realized with a certified PCE of 24.8% ( $J_{SC} = 15.6 \text{ mA cm}^{-2}$ ,  $V_{OC} = 1.965 \text{ V}$ , FF = 81%) for a FA<sub>0.7</sub>MA<sub>0.3</sub>Pb<sub>0.5</sub>Sn<sub>0.5</sub>I<sub>3</sub> perovskite bottom cell at 1.22 eV bandgap and a FA<sub>0.8</sub>Cs<sub>0.2</sub>Pb(I<sub>0.6</sub>Br<sub>0.4</sub>)<sub>3</sub> top cell at 1.77 eV, respectively.<sup>[15]</sup> The corresponding JV and EQE curves of these all-perovskite tandem solar cells are shown in Figure 7b,c, respectively. Additionally, the wide bandgap top cell has been optimized recently. Introducing a bulky dimethylammonium cation into the perovskite composition allows to raise the bandgap without increasing the Br content. As a result, photo-stable perovskite compositions with 1.7 eV bandgap and low voltage losses have been achieved, enabling 21.3% efficient 2T-tandem cells on flexible substrates<sup>[56]</sup> as well as 25% PCE in 4T configuration.<sup>[18]</sup> All-perovskite 2T tandems thus already exceed the record PCE of CIGS/perovskite tandems and are closing the gap to the current perovskite single-junction efficiency record of 25.2%.

Apart from all-perovskite tandems, there are also some reports on monolithic tandem solar cells combining perovskite and organic solar cells with however moderate efficiencies around 10%.<sup>[162,163]</sup> Also, 2T-multiplication devices without recombination layer were introduced, which do not require sub-cell current matching. In this case, an organic bulk-heterojunction (BHJ) interfacing the perovskite absorber has a dual function of selective charge extraction from the perovskite and additional generation of free carriers by absorption of long-wavelength light (Figure 7d). This concept was first demonstrated in 2015 with a PCE of 14.3%<sup>[164]</sup> and ascended to 20.6% in 2019 with a  $J_{SC}$  of 28 mA cm<sup>-2</sup> for a 1.6 eV perovskite absorber.<sup>[155]</sup> Although representing noticeable concepts, the better performance of perovskite as compared to organic solar cells as well as the inherent benefits of series-connected multi-junction devices, as introduced before, renders all perovskite tandem solar cells as a more promising strategy towards highest PCEs.

## 4. Advanced characterization of 2T tandems

### 4.1. Morphological, Structural, and Compositional Characterization

Gaining insights into morphological and structural properties of functional layers allows to assess their quality in terms of morphology, topology, surface coverage, chemical composition, crystallinity, or phase purity. These characteristics are particularly relevant for perovskite tandem solar cells in order to identify

shunt paths due to incomplete surface coverage, e.g., on rough surfaces of CIGS bottom cells,<sup>[62]</sup> phase impurities upon bandgap tuning,<sup>[165]</sup> as discussed in Section 2.6, but also layer thicknesses and surface topologies in order to optimize the optical properties of a tandem solar cell. The following section therefore presents suitable methods to gather such information together with application examples in literature on tandem solar cells.

Scanning electron microscopy (SEM) utilizes a focused electron beam in vacuum directed onto a specimen with a spot size of a few nanometers and kinetic energies in the order of 10<sup>2</sup>–10<sup>5</sup> eV. Depending on their kinetic energy and the material properties (density, atomic numbers), irradiated electrons can penetrate several hundreds of nanometers to few micrometers into the sample. The electron beam can interact with the material in the form of reflection by elastic scattering, Auger electron, and X-ray emission or emission of secondary electrons by inelastic scattering. The latter can be selectively detected owing to their comparably low kinetic energy. Variations in the composition or the angle of the sample surface typically affect the emission spectrum of secondary electrons. Therefore, by scanning a surface with an electron beam and detecting the corresponding intensities of secondary electron emission allows to create an image of a sample surface or cross section with a resolution down to 1–10 nm.<sup>[166]</sup>

For tandem applications, SEM top view and cross-section images of samples allow to assess grain sizes and the coarse morphologies of perovskite absorbers, surface coverages, and layer thicknesses. Enlarging grain sizes has for example been an effective method both in Sn-Pb based low bandgap<sup>[18,76,78]</sup> as well as wide bandgap<sup>[91]</sup> perovskite absorbers to reduce non-radiative recombination losses and enhance the device  $V_{OC}$ . Besides, determining the layer thicknesses in a tandem solar cell stack is crucial for their optical optimization, as discussed in more detail in Section 4.2.2. An exemplary SEM cross-section image of a perovskite top cell on a Si bottom cell is depicted in Figure 8a. All functional layers are well distinguishable even the rather thin ones of SnO<sub>2</sub> and MoO<sub>3</sub> with thicknesses of 15 and 27 nm, respectively.

Transmission electron microscopy (TEM) is comparable to SEM but instead detects electrons that are transmitted through the specimen and not getting scattered or diffracted. Typically high voltages (80–200 keV) accelerate a focused electron beam onto a solid sample with thicknesses around 10–200 nm depending on the atomic number of the examined material and the accelerator voltage. Scanning across the sample (STEM) then allows to create an image with a resolution down to the nuclear scale for high-resolution TEMs or HRTEM.<sup>[167]</sup> To achieve the required electron transparency, thin lamellas of samples are often cut out of the investigated material by a focused ion beam (FIB), usually Ga<sup>+</sup>-ions accelerated at around 30 kV, lifted off with a needle and mounted onto a TEM grid.<sup>[168,169]</sup> Subsequent thinning of the lamella, again with a FIB, can be performed under less acceleration voltage (5 kV) to reduce the damage on the sample, which is especially relevant for the more sensitive hybrid perovskite materials.<sup>[169,170]</sup>

STEM imaging can be used to determine layer thicknesses more accurately and with a higher resolution than in SEM, which is again pivotal for optical simulations of tandem solar cells. Also, the morphology and surface coverage of functional

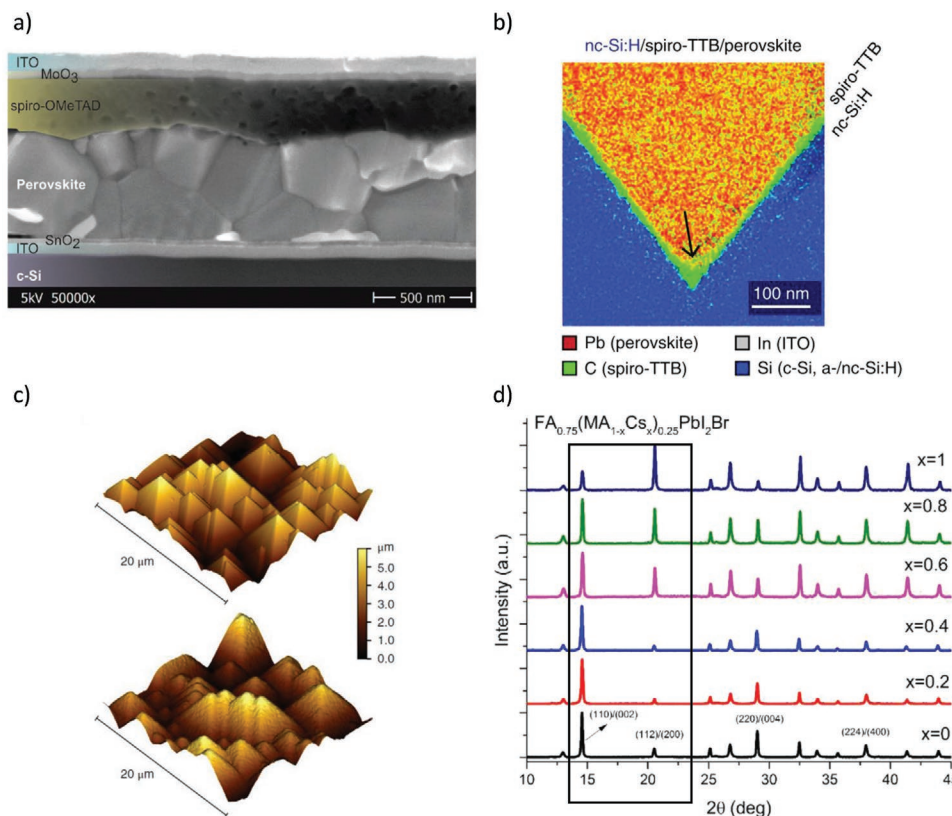


**Figure 8.** a) Cross-section scanning-electron microscopy (SEM) image of a perovskite-silicon tandem solar cell. All functional layers of the thin film top cell are highlighted and well distinguishable, even for the thinnest layer of  $\text{SnO}_2$  with 15 nm thickness. Reproduced with permission.<sup>[60]</sup> Copyright 2016, Royal Society of Chemistry. b) Energy-dispersive X-ray spectroscopy in a scanning tunneling electron microscope (STEM EDX) revealing full coverage of an only 12 nm thin transport layer between a pyramidal textured Si bottom cell and the perovskite top cell. Reproduced with permission.<sup>[38]</sup> Copyright 2019, Nature Publishing Group. c) Atomic force microscopy (AFM) image of a random pyramidal textured Si wafer (top panel) and a similar surface conformal covered with a perovskite top cell (bottom panel). Reproduced with permission.<sup>[38]</sup> Copyright 2019, Nature Publishing Group. d) X-ray diffractograms of  $\text{FA}_{0.75}(\text{MA}_{1-x}\text{Cs}_x)_{0.25}\text{PbI}_2\text{Br}$  wide bandgap ( $E_g \approx 1.74$  eV) perovskite thin films with the black square highlighting a transition in the peak intensities related to the  $(110)\backslash(002)$  and  $(112)\backslash(200)$  symmetry planes and thus a change in preferred crystallographic orientation depending on the composition. Reproduced with permission.<sup>[180]</sup> Copyright 2018, Royal Society of Chemistry.

layers can be investigated more thoroughly owing to the high magnification.<sup>[171,172]</sup> It allowed to investigate the AZO buffer layer growth in all-perovskite tandems on either bare  $\text{C}_{60}$  or  $\text{C}_{60}/\text{PEIE}$ .<sup>[56,173]</sup> Besides that, HRTEM allows to identify crystalline phases as used on Si bottom cells to investigate nc-Si:H<sup>[38]</sup> or partially crystallized a-Si:H films<sup>[100]</sup> as well as  $\text{TiO}_2/\text{p}^+/\text{Si}$  tunnel recombination junctions.<sup>[113]</sup>

Besides detecting electrons in SEM and TEM, also the X-rays being emitted from a sample can be analyzed by an X-ray dispersive detector in so-called energy-dispersive X-ray spectroscopy (EDX or EDS). The electrons being irradiated onto a sample can thereby excite or completely eject electrons from inner atomic shells of the analyzed material. The hole left in the inner shell is subsequently filled with electrons from higher energy levels, releasing their excess energy in the form of X-ray radiation with discrete energies according to the atomic structure of the respective element. EDX thus allows to qualitatively characterize the atomic composition of the probed sample volume. Further, evaluating the intensities of the X-ray emissions also permits to estimate the relative abundance of atoms and thus a quantitative elemental analysis. Note, that the detection limit typically restricts the quantitative analysis to elements

with an atomic number greater than four, so starting from boron.<sup>[174,175]</sup>

In SEM setups, the probed volume is typically a tear drop shaped sphere with a few cubic micrometers in size below the surface and therefore thicker than the usual perovskite top cell. Thus, SEM-EDX detects the superimposed chemical composition from all layers of a thin film stack and has been used for example to prove a loss of Cl during crystallization of  $\text{CH}_3\text{NH}_3\text{PbI}_{3-x}\text{Cl}_x$  absorbers.<sup>[176]</sup> However, SEM-EDX cannot resolve between individual layers of a perovskite top cell. On the other hand, in TEM the sample size (depth) is substantially smaller, in the order of a few tens to hundreds nanometers and the resolution of EDX measurements is greatly enhanced. This enables to determine elemental distributions in sample cross sections even for thin film layer stacks, which has been utilized to examine the surface coverage of specific layers as exemplarily shown in Figure 8b for a 12 nm thin hole transport layer on a pyramidal textured Si surface. STEM-EDX on such cross sections has further been used on perovskite solar cells to visualize phase inhomogeneities within the absorber,<sup>[177]</sup> diffusion of elements throughout the device,<sup>[172]</sup> or compositional changes upon thermal degradation.<sup>[178]</sup>

Further, the surface topology of a sample can be probed by atomic force microscopy (AFM). The method utilizes a nanometer thin measurement tip, usually from Si,  $\text{SiO}_2$ , or  $\text{Si}_3\text{N}_4$ , which is attached to a cantilever. When approaching a surface, the tip and the cantilever gets deflected by forces like mechanical contact forces, van der Waals forces, and electrostatic forces. Detecting this deflection, e.g., by measuring the angular change in reflection of a laser being irradiated onto the cantilever, allows to determine the sample surface topography with resolutions down to the atomic scale.<sup>[179]</sup> The topography is decisive for the deposition method or the required thickness of the subsequent layers. In an extreme example, the random pyramidal textured Si surface shown in the top panel of Figure 8c, with a roughness in the micrometer range, requires either a comparably thick subsequent layer or a conformal deposition of the top layers. In this specific case, as discussed in Section 3.1, the complete perovskite top cell was conformally deposited onto the Si bottom cell with the corresponding AFM image being shown in the bottom panel of Figure 8c. Besides that, the surface topography can strongly affect light scattering and thus reflection and interference in a layer stack. Knowing the topography of the interfaces in a tandem solar cell thus can increase the accuracy of optical simulations, as further discussed in section Optical Simulations.

Secondary ion mass spectrometry (SIMS) allows to analyze the chemical composition of a sample and create elemental depth profiles from a few angstroms to tens of micrometers. Therefore, the sample surface is atomically eroded by sputtering with a beam of energetic primary particles, typically ions such as  $\text{Ar}^+$ ,  $\text{Ga}^+$ , or  $\text{Cs}^+$ . Secondary ions being ejected from the sample can subsequently be analyzed in a mass spectrometer with resolutions down to sub-ppm trace levels. By progressively sputtering into the sample, an elemental depth profile of the specimen can be acquired. Typically, quadrupole or time-of-flight (TOF-SIMS) analyzers are employed as SIMS mass spectrometers. The latter one provides high mass resolution but requires a pulsed primary particle beam with only few atoms being removed from the sample at each pulse. An additional sputter beam is thus required for depth profiling in TOF-SIMS.<sup>[181,182]</sup> In perovskite tandem solar cells, SIMS has been employed to investigate the dopant concentration along an  $n^{++}/p^{++}$  Si tunnel recombination junction<sup>[100]</sup> or to determine the segregation of  $\text{Gua}^+$  and  $\text{SCN}^-$  ions toward grain boundaries in low-bandgap perovskites with  $\text{GuaSCN}$  as additive for enhanced performance and stability.<sup>[18]</sup>

Finally, X-ray diffraction (XRD) is a technique to determine the atomic structure of crystals or crystalline phases. Equally, if the crystal structure of a certain material is known, XRD allows to identify crystalline phases and the preferred crystallographic orientation of this material sample. XRD measurements use monochromatic X-ray beams, typically the  $\text{K}\alpha$  and  $\text{K}\beta$  line of a Cu anode ( $\lambda = 0.15406 \text{ nm}$ ), which are elastically scattered by the electronic shells of atoms in a solid. Due to the periodicity of atoms in crystal structures, incoming X-rays are scattered under the same angle but with different path lengths according to the lattice spacing. This results in a phase shift between the reflected X-rays and thus a characteristic diffraction pattern following Bragg's law for constructive interference:

$$2d \times \sin \theta = n\lambda \quad (1)$$

where  $d$  is the spacing between the crystal planes,  $\theta$  is the glancing angle of the incident beam,  $n$  is an integer, and  $\lambda$  is the wavelength of the incident X-rays.<sup>[183]</sup>

The intensities of the constructive interference peaks can reveal the preferred orientation of crystal domains in polycrystalline samples. Moreover, the full width at half maximum (FWHM) of a peak in an X-ray diffractogram can provide information about the domain size of the crystalline particles as well as the strain or stress induced onto the crystals. In brief, smaller domains or higher strain causes a line broadening of the interference peaks and thus a larger FWHM in the diffractogram. The mathematical description is given by the modified Scherrer equation named after Williamson and Hall that can be found elsewhere.<sup>[184]</sup>

For perovskite tandem solar cells, XRD measurements have not only been used to examine the crystallinity of TCO layers,<sup>[57,185–187]</sup> but also to determine existing crystalline phases in absorber layers during band gap tuning and thin film optimization. It allowed to monitor the final composition, crystallinity, and average domain size of absorber layers,<sup>[89,188,189]</sup> detect phase segregation in wide bandgap mixed halide perovskites,<sup>[190]</sup> and unravel the presence of photo inactive phases, e.g., the undesired  $\delta$ -phase in  $\text{CsPbI}_3$  perovskites.<sup>[191]</sup> As an example, Figure 8c illustrates the change in preferred crystal orientation from  $(110)/(002)$  to  $(112)/(200)$  with increasing amounts of Cs in  $\text{FA}_{0.75}(\text{MA}_{1-x}\text{Cs}_x)_{0.25}\text{PbI}_2\text{Br}$  wide bandgap ( $E_g \approx 1.74 \text{ eV}$ ) perovskite thin films (highlighted by a black box). Besides that, XRD can provide process and stability control, as it allows to detect unreacted species after absorber formation<sup>[38,57]</sup> or decomposition products upon stressing a device.<sup>[77,192]</sup> For perovskites, both can for instance be identified by  $\text{PbI}_2$  peaks in the X-ray diffractograms.

## 4.2. Optical Analysis and Simulations

The tandem solar cell stack is composed of two active layers and many additional charge transport and recombination layers as shown in Figure 5. A critical condition for the optimal photon-electron performance of monolithic tandem solar cells is that supporting layers absorb parasitically as little light as possible, while the absorption in both active layers is maximized in a way that both sub-cells generate equal amounts of current, i.e., current matching condition. Current matching is the most efficient condition, since due to a series connection, the sub-cell producing less current is limiting the current of the tandem device. Consequently, not all the charges are extracted, resulting in a performance loss and also potential degradation of sub-cells due to charge accumulation. Ensuring close to current matching conditions and extracting as many charges as possible are requirements for high PCE tandems.

A lot of focus has therefore been put on optical analysis of the tandem stack and optical design has been the main driving force behind the PCE improvements in perovskite/silicon tandem solar cells. The improvements are mostly achieved by minimizing reflection through interference engineering and the parasitic absorption. One of the main benefits of optical

simulations is insight into parasitic losses of the solar cell stack and contribution of each layer. Since the optical design can effectively be tested and improved using optical simulations, a lot of experimental time and material are saved.

For correct modeling, three requirements are needed. 1) the investigated stack has to work electrically. This already gives a constraint on the 2) thicknesses and band alignments of all the layers. 3) Optical constants (complex refractive indices  $n$  and  $k$ ) have to be known. Additionally, the investigated absorber layers must have internal quantum yields (how many of the absorbed photons are converted into electrons) close to unity (or at least known), which is thankfully the case for Si, CIGS, and perovskite. To determine the thickness of the layer, one can either choose one of the morphological methods, such as SEM, TEM, or AFM, or the optical methods that are discussed below. There, we will first describe optical characterization methods and then their application in optical simulations.

#### 4.2.1. Optical Characterization

The main optical characterization techniques for the analysis of perovskite-based tandem solar cells are spectrally resolved reflection ( $R$ ) and transmission ( $T$ ) measurements using a photospectrometer. Using a setup with an integrating sphere, all the light is captured and detected. If the additional ports of the integrating sphere are used, one can disentangle between direct and diffuse

light, obtaining also information about the light scattering properties of the sample. The method enables determination of absorption ( $A$ ) in the layer, using the equation  $A = 1 - R - T$ . Knowing the reflectance of the tandem device or the transmission of the layer stack are key components of tandem optimization.

For the  $n, k$  spectra extraction, there are two main methods: ellipsometry, and reflection and transmission (R&T). Additionally, one can also determine the absorption coefficient using photothermal deflection spectroscopy (PDS).<sup>[17]</sup> Spectroscopic ellipsometry is an optical method, primarily used for the determination of the complex refractive index and thickness of thin films. The sample under evaluation is usually illuminated with white linearly polarized light at an oblique angle, and the reflected light is characterized using a rotating polarizer (called analyzer) or compensator and a monochromator. The ellipsometer thus measures the spectral change in polarization, which is typically described by the relative change in polarization angle ( $\psi$ ) and phase shift ( $\Delta$ ), as shown in Figure 9a. Different incidence angles can be used to maximize the change in polarization and increase sensitivity. The sample structure can then be described using the transfer matrix method and the polarization data can be compared/fitted to an assumed thickness value and a suitable dispersion model, e.g., Tauc-Lorentz oscillator or Drude model, from which the complex refractive index can be extracted.<sup>[193]</sup> In the R&T method, the complex refractive index is back calculated from the reflection and transmission measurements using transfer matrix method.<sup>[194]</sup> Usually, more than

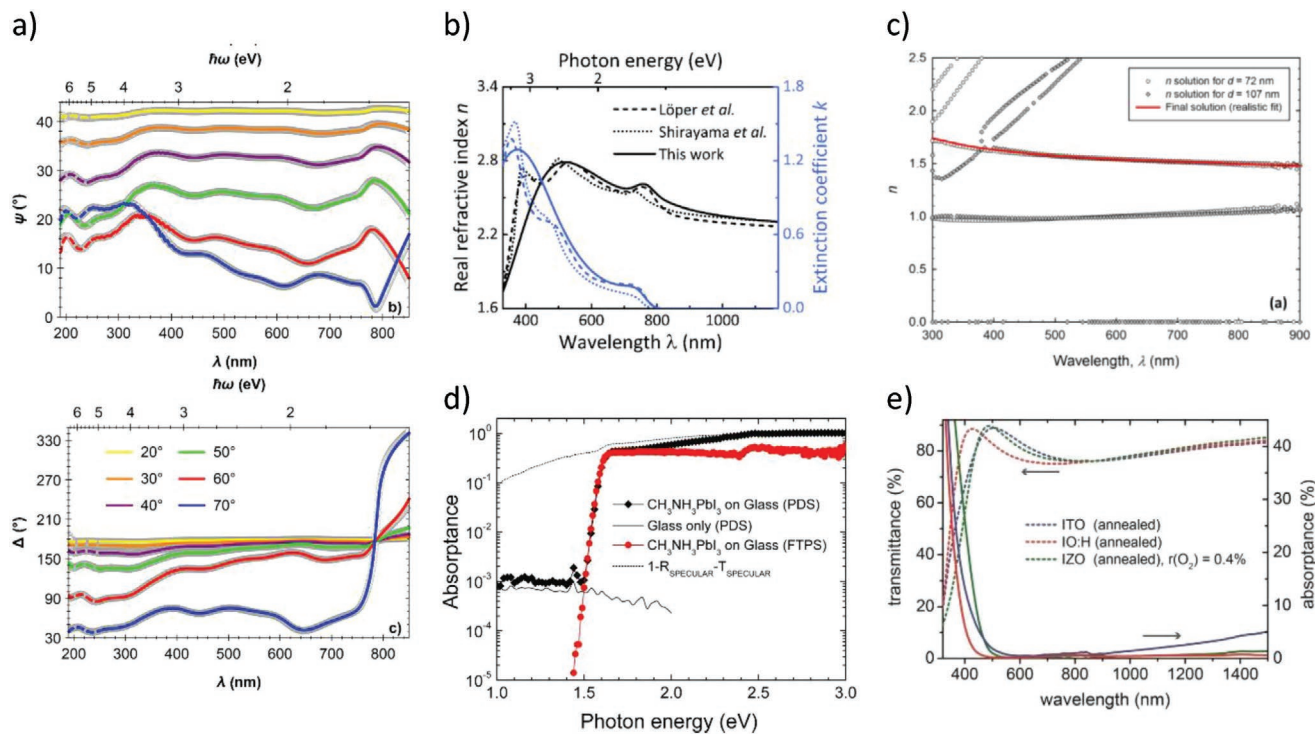


**Figure 9.** a) Spectral ellipsometry variables  $\psi$  and  $\Delta$  and fits for  $\text{FA}_{0.83}\text{Cs}_{0.17}\text{PbI}_3$  for different incident angles. Reproduced with permission.<sup>[195]</sup> Copyright 2018, AIP Publishing. b)  $n, k$  spectra comparison of  $\text{MAPbI}_3$  films from three different reports. Reproduced with permission.<sup>[196]</sup> Copyright 2017, Wiley. c) Determination of the refractive index of PEDOT:PSS by using the R&T method. Multiple solutions (black, white) are obtained from the R and T measurements, from which a realistic solution (red) is extracted. Reproduced with permission.<sup>[197]</sup> Copyright 2017, OSA Publishing. d) PDS, FTPS, and  $1 - R - T$  spectra of  $\text{CH}_3\text{NH}_3\text{PbI}_3$  perovskite thin films. Reproduced with permission.<sup>[17]</sup> Copyright 2014, ACS Publications. e) Optical transmittance and absorptance of ITO, IO:H, and a-IZO thin films. Reproduced with permission.<sup>[198]</sup> Copyright 2015, Electron Devices Society.

one solution is obtained, however, only one of them is realistic (Figure 9c). Both methods, spectral ellipsometry and R&T, are very precise and also give information about layer thickness. However, knowing the thickness beforehand, the model accuracy can be greatly improved. The requirements for successful modeling are homogeneous, isotropic, smooth ( $\sigma_{\text{RMS}} < 1/10$  of the probing wavelength) and non-scattering films. Potentially, also multilayers can be measured, however, optical constants of other layers in the stack have to be known. Nevertheless, a single layer is preferred, which is the case for the R&T method for samples deposited on transparent substrates. In PDS, the sample is illuminated with monochromatic light. Wavelengths above the bandgap are absorbed, thus the film locally heats up. Even this minor temperature change causes the deflection of a laser that is positioned in parallel to the sample, allowing to determine the absorptance from the deflection.

Ellipsometry is often used to determine optical constants of perovskites. The first paper analyzing perovskites using ellipsometry was published by Löper et al. where they analyzed  $\text{MAPbI}_3$  films.<sup>[199]</sup> Erdan et al.<sup>[196]</sup> and Shirayama<sup>[200]</sup> also analyzed  $\text{MAPbI}_3$ , and in Figure 9b, a graph comparing n&k spectra of  $\text{MAPbI}_3$  perovskite from the three reports is shown. All three spectra match well, confirming great accuracy and also repeatability of the perovskite films produced by different groups. With the development of perovskite absorber layers, other reports followed, focusing on more complex chemical composition of the absorber. Ndione et al. studied different methylammonium, formamidinium, and formamidinium cesium lead halide alloys, respectively, with different iodide to bromide ratios.<sup>[201]</sup> Similar analyses were also performed by Werner et al.<sup>[124]</sup> and Tejada et al.,<sup>[195]</sup> who analyzed FACs-based perovskites with different ratios of FA:Cs and I:Br. Using the method developed by Tejada et al., the analysis of not only flat but also rough, wrinkled films is possible. These wrinkles often appear with FACs compositions.<sup>[202]</sup> In all three reports, by Ndione, Werner, and Tejada, a clear shift in the bandgap onset and in the whole spectral range can be observed when changing the chemical compositions of the perovskite (Figure 9c). Following this, in case of unknown exact n&k spectra for a specific bandgap, a simple artificial bandgap shift, as also justified in refs. [203] and [204], could be performed with a sufficient accuracy, which is often the case in optical modeling. From the obtained absorptance or absorption coefficient spectra, the determination of the bandgap is usually done applying Tauc method<sup>[205]</sup> in the absorption onset region, where the absorption coefficient  $\alpha$  is proportional to  $\sqrt{h\nu - E_g} / h\nu$ . However, it has recently been suggested to use the inflection point of the EQE spectra as the most suitable way of extracting the bandgap of devices.<sup>[81]</sup> (see EQE spectra section).

Besides absorbers, the characterization of supporting layers is also important, since they can significantly contribute to parasitic absorption or induce interference. One of the most important layers is the front TCO, the only layer where all the light passes through. The main absorption in the TCO is in the UV, connected with material's bandgap, and in the NIR due to free carrier absorption. Since in the TCO the free carriers are needed for electrical transport and they cause significant parasitic absorption, which increases with the wavelength, the relation between optical absorbance and electrical conductivity has to be balanced. Especially, the mobility of the TCO is often

a bottleneck since no annealing above 100 °C is allowed due to perovskite degradation. Thus the most commonly utilized TCOs for perovskite-based tandems are ITO.<sup>[55,63,116,206]</sup> and IZO,<sup>[38,68,91,92,110]</sup> sputtered at low temperatures. Especially IZO is promising, since it already has a high mobility in the unannealed, amorphous state and consequently also lower parasitic absorption than, e.g., ITO and comparable to IO:H.<sup>[198]</sup> The transmittance and absorbance of the tree TCOs are compared in Figure 9c, showing the superior optical properties of IO:H, with IZO not far behind especially in terms of NIR absorption. There are some reports using a IO:H/ITO bilayer,<sup>[116,127]</sup> nevertheless, to achieve optimal IO:H properties, annealing at >150 °C is needed. Besides IZO and ITO, zirconium doped Indium oxide has recently been reported as a well-working top electrode.<sup>[207]</sup> Another interesting candidate is ZnO:Al, which is already used as a recombination layer in perovskite/CIGS tandem solar cells, however, no reports on it as a top contact could be found. To get the best properties, several processing parameters can be tuned, one of the main ones being additional oxygen, which makes films more oxide-rich (less metallic) and therefore more transparent; e.g., Morales Masis et al. and Könen et al. found a good balance between conductivity and parasitic absorption of the IZO by adding oxygen to the process, especially in the near infrared where the free carrier absorption starts to kick in.<sup>[68,198]</sup> This shows that optical analysis goes hand-in-hand with electrical characterization, which is discussed in Section 4.3.

#### 4.2.2. Optical Simulations

The optical simulations of perovskite/silicon solar cells are usually done using combined ray and wave optics models.<sup>[208,209]</sup> The two models enable simultaneous simulations of the whole device stack consisting of a thick- and a thin-film stacks. The thick layers (thickness larger than the wavelength of light,  $>1 \mu\text{m}$ ), e.g., silicon, glass, encapsulant, or light management foils, are simulated using ray-tracing and assume incoherent light propagation, where phase information of the light is lost. All the other layers are considered as thin-film. Here, coherent light propagation is assumed and handled using transfer matrix formalism. For periodic textures where dimensions are still within the wavelength of light, also finite element method (FEM) can be used.<sup>[64]</sup> The outputs of the optical simulations are total reflectance, parasitic absorption in each layer, and finally the current generated in each of the sub-cells. The latter is also the main goal in simulations, i.e., maximized and equal photocurrent in both active layers of the tandem. The simulated photocurrent in ideal case corresponds to the EQE measurement and the optical simulations are only relevant, when they can be backed up by experimental results, namely EQE and reflection measurements. Several groups have already shown good matching between simulations and experiments.<sup>[90,92,130,210]</sup>

Optical simulations have already provided some valuable guidelines for tandem development. First, due to strong parasitic absorption of spiro-OMeTAD over the whole wavelength range but mainly in the UV/blue region,<sup>[211]</sup> which is further enhanced by the doping<sup>[212]</sup> and a lack of an alternative, more transparent HTL, the p-i-n design has recently prevailed over

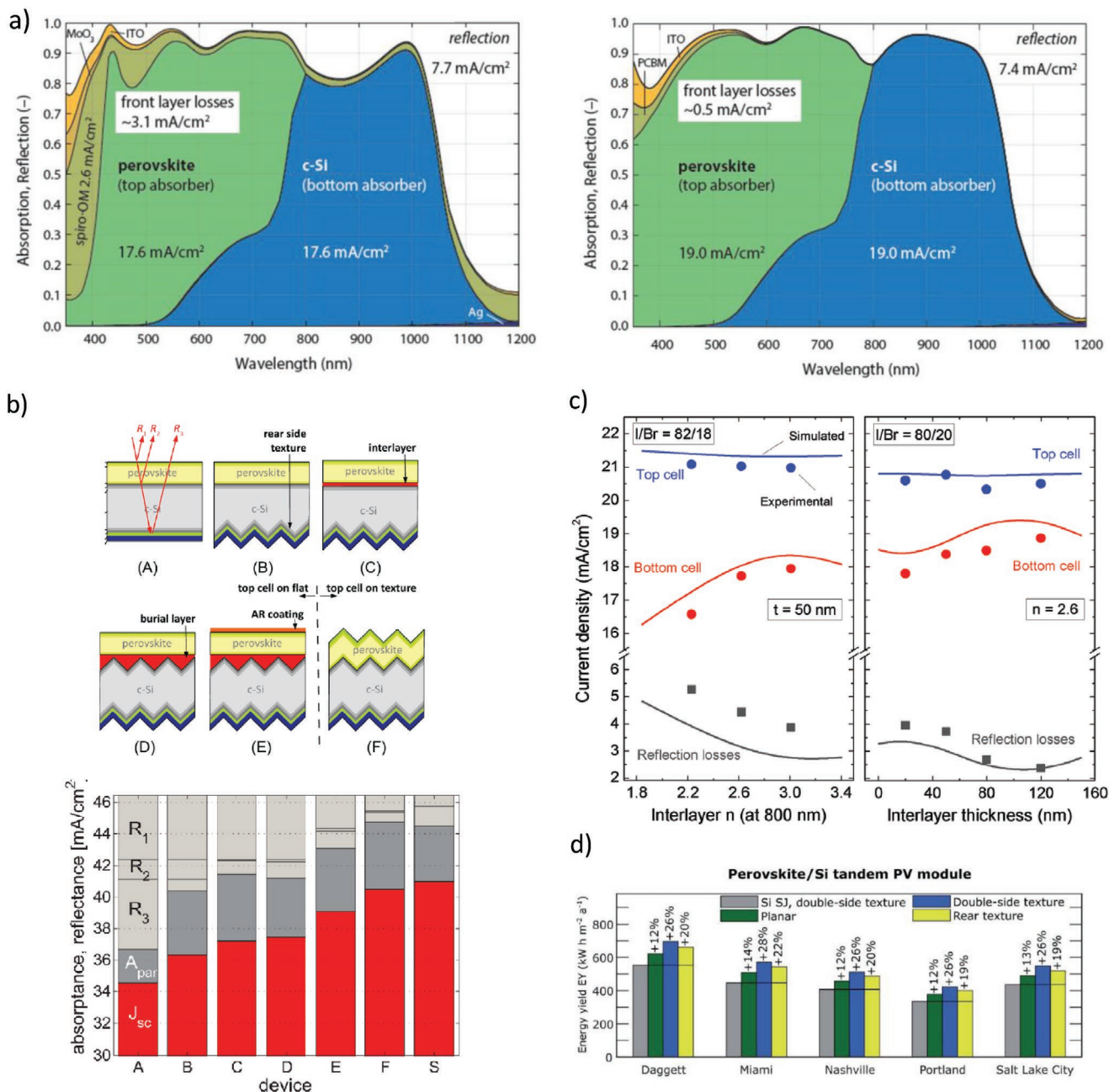


**Figure 10.** a) Comparison between optimized (left) n-i-p and right) p-i-n perovskite/silicon tandem architecture. In both cases, both-side polished silicon wafer was assumed. Reproduced with permission.<sup>[69]</sup> Copyright 2017, OSA Publishing. b) Analysis of anti-reflection options. Top: schematics of compared designs. Bottom: current distribution analysis. Reproduced with permission.<sup>[126]</sup> Copyright 2016, OSA Publishing. c) Effect of nc-SiO<sub>x</sub> on perovskite/silicon tandem performance. Left: dependence on the  $J_{SC}$  for different nc-SiO<sub>x</sub> refractive indices for a thickness of 50 nm. Right: effect of nc-SiO<sub>x</sub> layer thickness for the refractive index of 2.6. Reproduced with permission.<sup>[93]</sup> Copyright 2019, Wiley. d) Energy yield analysis for 5 different locations. Reproduced with permission.<sup>[129]</sup> Copyright 2018, Royal Society of Chemistry.

n-i-p.<sup>[69]</sup> The inclusion of spiro-OMeTAD layer in perovskite-based tandem solar cells is therefore not desired and, until a more transparent replacement HTM is found, is one of the main reasons why the highest PCE tandem devices are fabricated with a top cell of p-i-n architecture. This is not highly relevant for single-junction devices, since light reaches the perovskite layer prior to the spiro-OMeTAD. On the other hand, C60 and PCBM as the electron selective materials in the p-i-

architecture also have a strong absorption in the blue region.<sup>[213]</sup> However, the C60 thickness needed in p-i-n type solar cells is only 10–20 nm, thus the overall absorption is much lower compared to the thick spiro-OMeTAD layer. Optimized optical stacks of the n-i-p (left) and p-i-n (right) architectures based on flat silicon wafers are compared in Figure 10a; 1.4 mA cm<sup>-2</sup> are gained by inverting the polarity and avoiding spiro-OMeTAD. Replacing spiro-OMeTAD in n-i-p tandem devices by less

absorbing materials, such as PTAA or spiro-OMeTAD/PEDOT mixtures,<sup>[214,215]</sup> is possible, however, their performance is lower and their deposition is still done using solvent processing. This automatically means thicker, more absorbing films due to rougher perovskite films that need to be fully covered. Second, a big improvement in current management of the p-i-n design has been achieved by introducing nano-crystalline SiO<sub>x</sub>:H as the front side field of the silicon sub-cell instead of (n) a-Si. By tuning the oxygen content, we can efficiently change the refractive index of the nc-SiO<sub>x</sub>:H and thus improve the refractive index gradient between the recombination ITO ( $n \approx 2$ ) and silicon ( $n = 4$ ). An index of  $n = 2.6$  has proven to be the most beneficial and by also adjusting the thickness of the nc-SiO<sub>x</sub>:H layer, the interferences are damped and the reflection is minimized.<sup>[93,216]</sup> A current increase of  $>1 \text{ mA cm}^{-2}$  can be obtained this way as shown in Figure 10c. Third, light management using textured interfaces can improve the stack.<sup>[90,92,126,217]</sup> Textures cause light scattering and/or refracting, prolonging the optical path in the absorber. The researchers have thus quickly turned from both side polished silicon wafer to a back-side textured one since the backside considerably improves the NIR response and does not constrain the solvent-processing on the front side. Optically superior is a tandem fabricated on double-side textured silicon wafers, however, experimentally this has so far been proven to be challenging. Sahli et al. did so by utilizing a hybrid perovskite deposition process. The obtained combined current from both sub-cells exceeded  $40 \text{ mA cm}^{-2}$  with minimal reflection of only  $1.6 \text{ mA cm}^{-2}$ , however, the tandem suffered from low FF.<sup>[38]</sup> Whether this electrical limitation, arising from the deposition on the textured surface could be overcome remains to be seen. If not, front side flat devices have to be utilized. The simulations predict the possible current yield of  $20.6 \text{ mA cm}^{-2}$  for the double-side textured tandem and around  $20 \text{ mA cm}^{-2}$  for the front-side polished tandem. The effect of front-side texture has also been integrated through light management foils.<sup>[90,92,116,127]</sup> The effect of different anti-reflection options is depicted in Figure 10b, showing superior optical properties of double-side textured configuration. Another interesting approach is also to utilize nanophotonic light management using, e.g., periodic pillar arrays or sinusoidal textures, on top of which spin coating is still possible.<sup>[64,218,219]</sup> An overview of light management in perovskite/silicon tandem solar cells was recently published by Xu et al.<sup>[220]</sup> Fourth, the optimal bandgap of the top cell with the Si bottom cell has been estimated to be  $\approx 1.66\text{--}1.7 \text{ eV}$ . Similar should also apply to CIGS based tandem cells. While the bandgap does not alter the current output (current matching can then be achieved by tuning the thickness), the benefit is in the increased  $V_{OC}$ . Thus it is critical to prevent the halide segregation as discussed in the introduction. Exceeding the bandgap of  $1.7 \text{ eV}$ , however, will prevent the current matching due to not enough current generated in the top cell, regardless of the absorber thickness.

Further optical improvements lie in reducing the parasitic absorption in the UV and NIR. In the UV region, the front TCO and C<sub>60</sub> still absorb more than  $2 \text{ mA cm}^{-2}$ . Therefore, a more transparent ETM is needed, preferably also evaporable to ensure conformal coating of the surface. PCBM, for example, has a lower parasitic absorption but can only be solution-processed.

Several TCO materials have already been tested, however, the temperature sensitivity of the perovskite is a major obstacle as discussed above. An important optical aspect is also moving towards industrially relevant silicon bottom cells. Therefore, the silicon bottom cell is thinner ( $\approx 140\text{--}180 \mu\text{m}$ ) than in laboratory experiments and most of simulations ( $250 \mu\text{m}$ ). As a result, the absorption in silicon is lower and the optimal bandgap of perovskite increases. Consequently, changing one or two layers in the stack changes the optics of the whole device and also the optimal bandgap of the top cell.

Finally, the main criterion of the device is its energy output over the year, i.e., energy yield. While the experimental measurements and simulations are done under standard testing conditions (AM1.5G), in reality, the irradiance, incidence angle, and spectral distribution of light change. This makes the analysis more complex, especially as the current generation in both sub-cells changes and potential mismatch occurs. Changing irradiation conditions thus affects current, voltage, and FF of the devices. It is possible that in some cases the device optimized under STC conditions does not produce the most energy. Instead, a slight current mismatch between sub-cells, either perovskite or bottom cell limited, might prove to be better. Thus, in parallel to the STC optimization, also energy yield has to be analyzed.

Several papers have recently discussed this.<sup>[70,92,129,130,221,222]</sup> The energy yield calculation is based on optical simulations, where in addition to perpendicular incidence also oblique incidence and diffuse irradiance are considered, depending on the time of the day. From an integrated product of absorptance spectra in spectrally resolved irradiance, the  $J_{SC}$  can be obtained. For  $V_{OC}$  and FF,  $J$ -Vs under different light intensities have to be measured or calculated using the diode models. The methodology behind the energy yield modeling is nicely described by Schmager et al.<sup>[222]</sup> Providing that weather data are available, energy yields for any location can be calculated using optical simulations. In Figure 10d, an example of energy yield calculations for five different locations and four different cell designs is depicted.<sup>[129]</sup> The results show that monolithic tandems outperform single-junction devices and that front-side texture can further improve the energy yield by  $>5\%$  compared to a front-side flat device. These findings are also supported by results from other publications.<sup>[92]</sup> Using energy yield calculation, the concerns that current mismatch due to spectral changes significantly reduces the energy output were rejected.<sup>[223]</sup> While the loss due to current mismatch is there, it is almost negligible and further reduced by FF improvement under current mismatch, compensating the current loss. In the future, temperature effects will have to be added to energy yield analysis. Despite being a crucial parameter, it has been neglected due to lack of reliable parameters needed for temperature integration. The inclusion of temperature will drastically change the optics of tandem device, since perovskite bandgap widens with temperature, while, e.g., silicon's becomes narrower. This will additionally complicate the evaluation of energy output and potentially make optimal tandem design very location and climate dependent. Following this, the complex optics of tandem devices, the energy yield procedure seems to be a suitable way of optimizing tandem solar cells.

### 4.3. Electrical and Electronic Characterization

In order to understand the functionality of perovskite-based devices (and of electronic devices in general), information about the electronic properties of thin films and their interfaces is needed: for the perovskite absorbers, carrier recombination lifetimes, which are governed by the density and distribution of defect states in the bandgap, determine cell  $V_{OC}$  and fill factor. These defects can be located both in the film's bulk, including grain boundaries, and at its interfaces. For the fill factor, transport properties for both electrons and holes, which are governed by charge carrier densities and their mobilities, are equally important parameters. This is also true for the carrier selective contact materials, i.e., electron and hole transport layers, as well as for additional contact layers such as transparent conductive oxides (TCOs). Furthermore, not only the bulk film properties will be important, but also those of the various heterointerfaces in the cell stack. Here, both interfacial defect densities and band offsets between the materials forming the heterointerface are crucial for recombination and transport properties.

This section will give a brief overview of electrical and photo-emission techniques that can be used to probe the mentioned quantities, while the following section will focus on radiative characterization techniques that give deeper insight into charge carrier recombination.

Electrical resistivity,  $\rho$ , is the most basic parameter to assess the suitability of thin films, e.g., as transport layers.<sup>[224]</sup> When the film thickness  $t$  is unknown, a sheet resistance  $R_s = \rho/t$ , in units  $\Omega \text{ sq}^{-1}$ , is reported. Several contact geometries are common for measuring this quantity in thin films:<sup>[225]</sup> In four-point current-voltage measurements, four equally spaced, point-like contacts are connected to the sample. Often, these contacts are a set of spring-loaded needles that are simply pressed onto the sample. A current  $I$  is applied between the two outer contacts, and the voltage  $V$  is measured between the inner contacts. Then, for  $t$  much smaller than the tip distance, the film resistivity  $\rho \sim t \times V/I$  and the proportionality factor contains corrections accounting for the sample geometry. The advantage of the four-point-probe technique lies in the fact that the contact resistance  $\rho_c$  between the metal contacts and the sample plays no role in measuring the potential difference. This technique is often used, e.g., to measure the resistivity of TCOs. A similar approach to measuring film resistivity, but this time also yielding the contact resistance, is the so-called transition line method (TLM). Here, parallel stripe contacts are deposited on or under the thin film, and the resistance  $R$  between them is plotted as a function of their lateral distance. Then,  $\rho$  is obtained from the slope of  $R$  versus distance, the contact resistance  $\rho_c$  can be calculated from the intercepts with the axes. Finally, another common contacting method for resistivity measurements is the so-called van der Pauw geometry. Here, the sample can be of arbitrary shape, and the four probes can be located anywhere on its periphery, as long as they are small compared to the sample size. Moreover, the van der Pauw theorem requires homogeneous, thin, isotropic, and singly connected films. The latter requirement means that the sample is not allowed to have isolated holes. Again, the proportionality given above applies, and for symmetric samples, the proportionality factor is simply  $\pi/\ln 2$ .

Regarding the application of such measurements in both single-junction and tandem cells, a frequent use case is to assess the suitability of transparent conductive electrodes, e.g., TCOs,<sup>[226]</sup> conductive polymers,<sup>[227]</sup> graphene,<sup>[228]</sup> thin metal films or meshes,<sup>[229]</sup> etc. Often, a trade-off must be made between high enough conductivity and/or low contact resistance on the one hand, and sufficient optical transparency on the other. This is because an increased conductivity is usually accompanied by increased parasitic absorption in the IR part of the optical spectrum: the conductivity is given by  $\sigma = 1/\rho = e(\mu_n n + \mu_p p)$ , with  $e$  the elementary charge and  $\mu_n$  ( $\mu_p$ ) and  $n$  ( $p$ ) being the mobility and concentration of electrons (holes), respectively. Since the mobilities usually cannot be changed much for a given TCO, the carrier concentration needs to be increased for high conductivity. For example, when commonly used TCOs such as indium-tin oxide (ITO) or zinc oxide doped with aluminum (ZnO:Al) are deposited by sputtering, this is possible, e.g., by changing the oxygen content in the sputter gas. However, these free carriers absorb IR photons, which for most TCOs is well described by the Drude model. Qualitatively, it states that with increasing carrier density the IR absorption not only increases, but also its onset shifts toward shorter wavelengths, potentially yielding parasitic absorption in wavelength regimes that can be utilized by the solar cell. In organic electrode materials, increasing parasitic absorption upon doping is known.<sup>[227,230]</sup> However, here it usually yields localized absorption bands corresponding to changing oxidation states. Nevertheless, similar trade-offs between optical and electrical properties are required.

To gain deeper insights into the mechanisms of electrical conductivity, Hall measurements are often used: four electrical probes are brought in contact with the thin film, most frequently in the van der Pauw configuration. Then, a current  $I$  passed through two contacts, and a magnetic field with strength  $B$  is applied perpendicular to the plane of the film. The resulting so-called Hall voltage  $V_H$  is measured at the remaining two contacts, and the Hall mobility  $\mu_H$  of the majority charge carriers can be calculated from this voltage. When  $\mu_H$  as well as the conductivity  $\sigma$  are known, it is straightforward to compute the majority carrier density  $n$  or  $p$  of n- or p-type semiconductors, respectively. Furthermore, from systematic variations of film parameters such as doping or surface roughness, as well as external parameters—notably, the sample temperature—detailed information on scattering mechanisms in the film can be obtained. For example, in nonpolar semiconductors such as silicon, the scattering of charge carriers with acoustic phonons is dominating the temperature dependence of the mobility, with a characteristic dependence  $\mu \approx T^{-3/2}$ . However, at lower temperatures and sufficiently high densities of ionized impurities (e.g., dopant atoms) are responsible for the dominant scattering mechanism, yielding a dependence  $\mu \approx T^{3/2}$ . Thus, the mobility is highest at an intermediate temperature. For TCOs, the dependence of carrier density and Hall mobility on doping has been investigated intensively, we cite for ZnO:Al<sup>[231,232]</sup> and for ITO.<sup>[233,234]</sup> These are the most frequently used TCOs in silicon heterojunction solar cells that are also suitable for tandem applications. Hall measurements have also been used to investigate metal halide perovskite films, see, e.g.,<sup>[19]</sup> or the comprehensive review on mobility measurements

(also using other techniques, cf. below) in metal halide perovskites by Herz.<sup>[235]</sup> Hall mobilities show a wide spread, between several 10 and several 100 cm<sup>2</sup> V<sup>-1</sup> s<sup>-1</sup> in state of the art polycrystalline films, and up to 2000 and 300 cm<sup>2</sup> V<sup>-1</sup> s<sup>-1</sup> for electron and holes, respectively, as shown in the case of CH<sub>3</sub>NH<sub>3</sub>SnI<sub>3</sub> single crystals.<sup>[236]</sup> However, as also noted in,<sup>[235]</sup> it appears that at least in some cases, erroneous values due to non-ideal contacts and effects such as ion-migration in the applied electric fields cannot be excluded.

To assess the electronic quality of the absorber materials and their interfaces for both, perovskite and silicon, information on charge carrier lifetimes and diffusion lengths is required. In wafer-silicon, transient photoconductance decay (PCD)<sup>[237]</sup> is a contactless standard technique for measuring the dependence of effective minority charge carrier lifetime,  $\tau_{\text{eff}}$ , on the excess minority charge carrier density,  $\Delta n$  or  $\Delta p$  (for p- or n-type doped wafers, respectively). Usually, symmetrical samples, i.e., c-Si wafers coated on both sides with the relevant contact or passivation layer stack, are analyzed to facilitate data analysis: in the case of high wafer quality as well as good interface passivation and hence low interface recombination velocity  $S_{it}(\Delta p)$ ,  $S_{it}$  can simply be calculated from the approximation  $\frac{1}{\tau_{\text{eff}}} = \frac{1}{\tau_{\text{bulk}}} + 2 \frac{S_{it}}{W}$ .<sup>[238]</sup>

Here, W is the wafer thickness, and the bulk minority carrier lifetime  $\tau_{\text{bulk}}$  in the wafer is usually measured beforehand for the specific wafer material, but coated with excellent passivation layers such as SiO<sub>2</sub>/SiN<sub>x</sub> stacks or hydrogenated amorphous silicon, a-Si:H. These coatings yield  $S_{it} \approx 0$ , thus the measured  $\tau_{\text{eff}} \approx \tau_{\text{bulk}}$ . Advanced interface recombination models can be used to extract further information such as interfacial band bending, fixed charges, densities and carrier capture cross sections of defects in the c-Si bandgap.<sup>[239,240]</sup> Note that since the photoconductance is not only dependent on carrier density but on the mobility-carrier density products,  $\mu_p \Delta p + \mu_n \Delta n$ , reliable information on  $\mu$  is necessary to extract quantitative information on excess charge carrier densities.

The PCD technique relies on measuring the areal density—thus, integrated over the absorber thickness—of photogenerated charge carriers in an absorber. Therefore, the simple approach used on wafers, where a resonance circuit couples inductively to the photogenerated charges via a coil, is not sensitive enough for very thin films such as perovskite and CIGS. This is why other methods are frequently used that can probe the densities  $n$  and  $p$  of free carriers, or the mobility-density products  $\mu_n n$ ,  $\mu_p p$ , and their evolution versus time directly. To obtain information on recombination in thin-film absorbers, and specifically in perovskites, the most widely used technique is probably transient photoluminescence, which is discussed in detail below. Furthermore, such methods include transient reflection and absorption spectroscopy (TRS/TAS),<sup>[241–243]</sup> terahertz spectroscopy,<sup>[244,245]</sup> transient microwave conductivity (TRMC),<sup>[246–248]</sup> and surface photovoltaic spectroscopy (SPV).<sup>[161]</sup> If electrical contacts to the sample are available, impedance spectroscopy,<sup>[249,250]</sup> open-circuit voltage decay (OCVD),<sup>[251]</sup> and space charge limited current (SCLC)<sup>[252,253]</sup> measurements can be applied as well. These techniques have been used to elucidate, among others, the mechanisms of mono-molecular (Shockley-Read-Hall) charge-recombination at shallow traps (tens of

millielectronvolts) for hybrid lead iodide perovskites, to extract charge-carrier mobility values and investigate their dependence on perovskite composition and morphology, to calculate charge-carrier diffusion lengths, as well as to obtain such information on transport layers.

Photoelectron spectroscopy is a powerful tool for obtaining information on both film composition and electronic properties: With X-ray photoelectron spectroscopy (XPS), i.e., using photons with energies in the X-ray range for excitation, information about film stoichiometry and the local bonding environment can be obtained. Typical XPS lab sources use  $h\nu = 1586.6$  eV (Al K $\alpha$ ) and  $h\nu = 1253.6$  eV (Mg K $\alpha$ ). Using excitation with UV photons (UPS, most common: He I emission at  $h\nu = 21.2$  eV), the valence band region close to the Fermi level can be analyzed in order to obtain the position of the valence band edge ( $E_V$ ) of inorganic semiconductors or, for organic semiconductors, the binding energy of the highest occupied orbital, HOMO. Furthermore, UPS of the so-called secondary electron cut-off (SECO) provides information about the work function, WF or  $\phi$ , of the sample surface, i.e., the energetic distance between the surface Fermi level and the vacuum level,  $E_{\text{vac}}$ . Combining these values, the ionization energy (IE)  $I^* = E_{\text{vac}} - E_V$  (equivalently,  $E_{\text{vac}} - E_{\text{HOMO}}$ ) can be calculated. If the bandgap is known, e.g., from optical absorption, the electron affinity  $E_A = E_{\text{vac}} - E_C$  (or  $E_{\text{vac}} - E_{\text{LUMO}}$ ) can also be computed.

Three important sources of error should be kept in mind when applying photoelectron spectroscopy techniques to metal halide perovskites. First, when applying XPS and UPS to perovskite absorbers, as with other semiconductors, the effects of surface photovoltage need to be considered: Under the intense UV- or X-ray illumination, the photogenerated electrons and holes lead to a splitting of quasi-Fermi levels and a change in band bending relative to the bands in the dark, giving rise to the so-called surface photovoltage. This may lead to errors in the determination of the energy positions of  $E_V$  and  $E_F$ , or of core level positions. Another issue is more specific for perovskites. It has been shown that they can exhibit—sometimes very pronounced—instabilities under UV/X-ray illumination.<sup>[254]</sup> While the responsible degradation mechanisms are probably similar to those seen under intense illumination in the near-UV during standard solar cell device testing, it has been postulated that threshold energies in the UV exist for certain additional degradation pathways.<sup>[133]</sup> Both problems, i.e., pronounced photovoltages as well as degradation under illumination, can be remedied by low-intensity illumination combined with highly sensitive photoelectron detectors, as recently demonstrated for both XPS<sup>[257]</sup> and UPS.<sup>[256]</sup> Finally, we mention that an additional issue lies in the correct determination of the valence band edge in perovskites: When in standard UPS measurements on polycrystalline perovskites, the valence band edge  $E_V$  is determined as usual by linear extrapolation of the leading edge of the spectrum, this yields a too large energetic distance between the Fermi level and  $E_V$ , e.g., see ref. [257]. Obviously, this will also lead to systematic errors in determining band offsets to such perovskites. The reasons are strongly dispersive features in the band structure of halide perovskites, particularly along the X-R direction of the Brillouin zone, which yield

**Table 2.** Absolute energy level positions in tin- and lead-based halide perovskites.

	Pb based			Sn based			
	I	Br	Cl	I	Br	Cl	
$E_{g,\text{opt}}$	1.72	2.31	2.99	1.25	1.81	2.88	
I*	6.25	6.53	6.80	5.69	5.82	6.44	Cs
EA	4.47	4.17	3.77	4.38	4.07	3.47	
$E_{g,\text{opt}}$	1.59	2.30	3.04	1.24	2.13	3.50	
I*	5.93	6.60	6.92	5.39	5.67	6.85	MA
EA	4.36	4.25	3.77	4.07	3.42	3.36	
$E_{g,\text{opt}}$	1.51	2.25	3.02	1.24	2.63	3.55	
I*	6.24	6.7	6.94	5.34	6.23	7.33	FA
EA	4.74	4.51	3.98	4.12	3.6	3.83	

I\*, ionization energy; EA, electron affinity. Reproduced from<sup>[265]</sup> with permission.

comparatively small contributions from the global valence band maximum located at R to the measured UPS spectrum.<sup>[258]</sup> As already proposed by Endres et al.,<sup>[257]</sup> it is therefore preferable to use the onset of the UPS signal on a semi-logarithmic scale to determine  $E_V$ .

Such XPS and UPS data are the basis for a number of studies and reviews that highlight the importance of both film stoichiometry and surface/interface properties in perovskites, see, e.g., refs. [259–266] or the recent comprehensive overview by Schulz et al.<sup>[22]</sup> The correlation between perovskite film stoichiometry and its ionization energy has been studied by Emara et al.<sup>[266]</sup> They investigated  $\text{CH}_3\text{NH}_3\text{PbI}_3$ -based perovskites, varying the  $\text{PbI}_2:\text{MAI}$  mixing ratio from 0.6 to 1.4, and found a change of the ionization energy by almost 1 eV, from 5.7 to 6.4 eV. Later, similar studies including Cs and Formamidinium on the cation site as well as Sn-based perovskites, in combination with DFT calculations, culminated in the set of absolute energy level positions for all primary, stoichiometric tin- and lead-based perovskites reproduced in **Table 2**.<sup>[265]</sup> Furthermore, it could be demonstrated that energy level variations are primarily determined by the relative positions of the atomic energy levels of metal cations and halide anions, and to a lesser degree by the cation–anion interaction strength.

In a next step toward understanding the energetics of full devices, the band alignment between the perovskite absorber and the electron and hole transport materials needs to be considered. For ETLs, in addition to a Fermi position close to the conduction band edge—i.e., high conductivity for electrons—a similar energetic position of the ETL’s conduction band edge (or LUMO) and the perovskite’s conduction band edge is desired. Similarly, a Fermi level close to the valence band edge and  $E_V/\text{HOMO}$  close to the perovskite’s  $E_V$  are considered to be preferable for the HTLs. Again, photoelectron spectroscopy in combination with, e.g., optical spectroscopy can provide the relevant information on band edge positions. Inspired by similar plots for organic semiconductors, such information has been compiled into overviews such as **Figure 11a**, and it is often used to estimate band offsets between the perovskite and transport materials using the so-called Anderson rule.<sup>[267]</sup>

Here, the band edges are referred to the vacuum level, and conduction and valence band offsets between materials A and B are calculated as  $\Delta E_C = E_{A,A} - E_{A,B}$  and  $\Delta E_V = I^*_A - I^*_B$ , respectively. However, Anderson’s overly simplistic model disregards the existence of surface/interface states, chemical reactions at the interfaces, etc. It has been shown to be of limited value to predict the band offsets in inorganic semiconductors (III-V or Si-based heterostructures). Similarly, also for perovskite/ETL or HTL interfaces, a more complex picture has emerged in recent studies. We show an example in the lower panel of **Figure 11**,<sup>[268]</sup> where five different potential contact materials were deposited onto  $\text{CH}_3\text{NH}_3\text{PbIBr}_2$  perovskite films, and their band offsets were investigated using UPS. The formed heterojunctions show very different band lineups and interfacial dipoles (panel c). Using UPS, the alignment can be rationalized qualitatively from the work function dependence of charge transfer at the interface: where the perovskite work function, as measured on the bare perovskite film (**Figure 11b**, lowermost curve), is initially smaller than the electron affinity (EA) of the HTMs (i.e., for  $\text{F}_{16}\text{CuPC}$ , HAT-CN, and  $\text{MoO}_3$ ),  $E_F$  in the perovskite would lie above the LUMO (or CBM) of the HTM when both materials come into contact. Spontaneous charge transfer will occur across the interface, resulting in the formation of an interface dipole, i.e., a potential step, and a corresponding shift in the energy levels. Thus, the energy level offset is different from that predicted by Anderson’s rule (vacuum level alignment). Note that in both the  $\text{F}_{16}\text{CuPC}$  and HAT-CN layers, a gradual change of the vacuum level position is found as the thickness increases until the equilibrium electron affinity is attained at a sufficient distance from the interface. Lately, the deliberate creation or modification of such interface dipoles, or of charge-transfer doping effects upon modification of perovskite interfaces, e.g., using oxidizing agents<sup>[259]</sup> or by introducing alkali metals<sup>[269]</sup> has been studied. Finally, we note that photoelectron spectroscopies using either much lower or much higher photon energies than in conventional UPS can be advantageous to directly measure the valence band edges of both, substrate and thin film at the same time, for film thicknesses of up to a few nanometers. This is because of the strong variation of the photoelectron

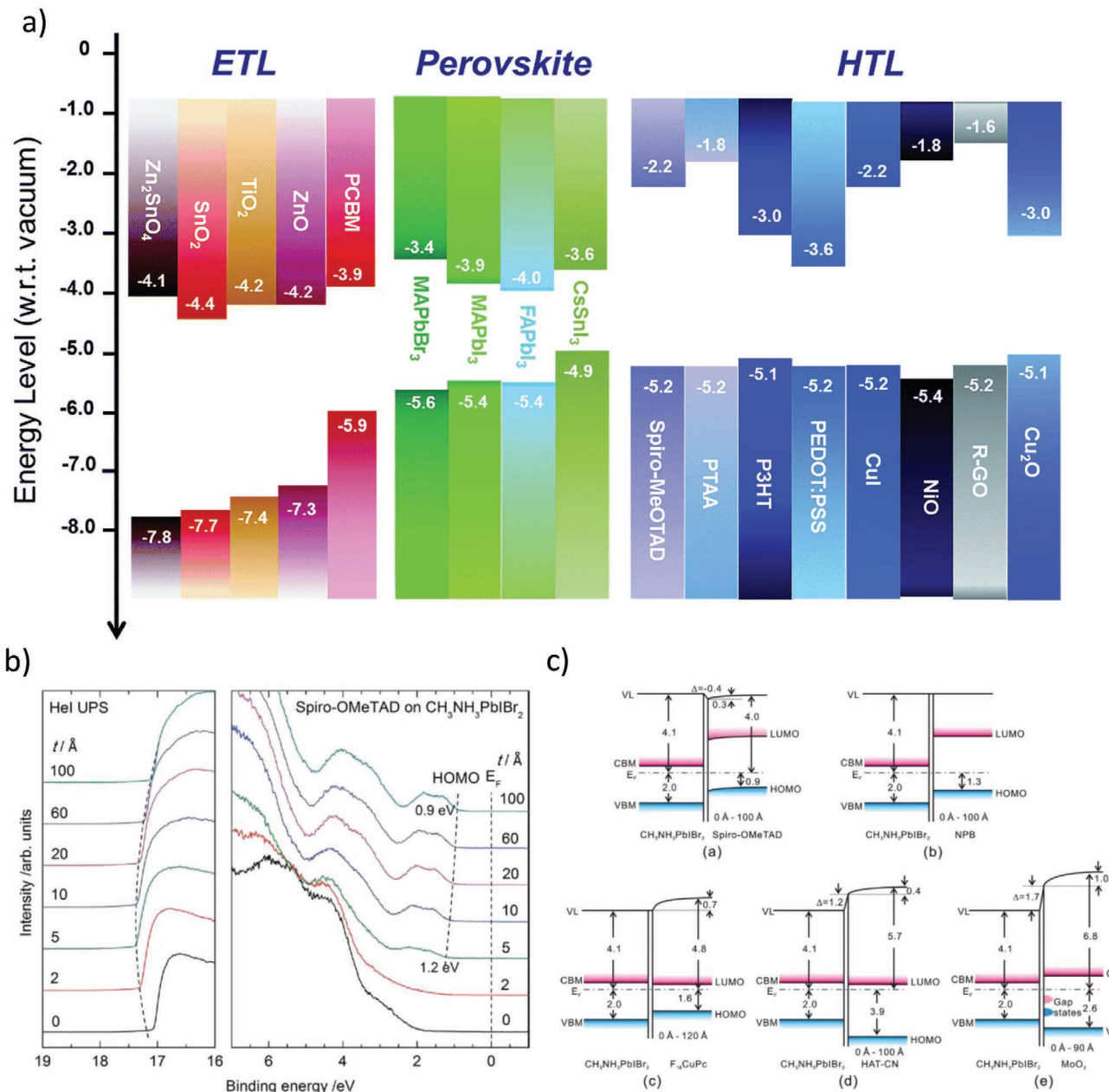


**Figure 11.** Top graph: Overview of electron affinities and ionization energies of common perovskites, electron (ETL) and hole (HTL) transfer layers. Reproduced with permission.<sup>[273]</sup> Copyright 2017, The Royal Society of Chemistry. Lower panel: a) Thickness (*t*) dependence of UPS spectra of spiro-OMeTAD on CH<sub>3</sub>NH<sub>3</sub>PbI<sub>3</sub>Br<sub>2</sub>. The left panel displays the SECO region and the right panel displays the HOMO region. b) Schematic energy level diagrams of i) CH<sub>3</sub>NH<sub>3</sub>PbI<sub>3</sub>Br<sub>2</sub>/Spiro-OMeTAD, ii) CH<sub>3</sub>NH<sub>3</sub>PbI<sub>3</sub>Br<sub>2</sub>/NPB, iii) CH<sub>3</sub>NH<sub>3</sub>PbI<sub>3</sub>Br<sub>2</sub>/F<sub>16</sub>CuPc, iv) CH<sub>3</sub>NH<sub>3</sub>PbI<sub>3</sub>Br<sub>2</sub>/HAT-CN, and v) CH<sub>3</sub>NH<sub>3</sub>PbI<sub>3</sub>Br<sub>2</sub>/MoO<sub>3</sub> interfaces. All values in eV. The energetic positions of the vacuum level (VL), HOMO, and VBM relative to E<sub>F</sub> are extracted from UPS measurements, CBM and LUMO levels are derived by taking into account the charge transport gaps. Reproduced with permission.<sup>[268]</sup> Copyright 2015, Wiley-VCH.

inelastic mean free path (IMFP), with energy: the IMFP determines the information depth of photoelectron spectroscopy. It is minimal at typical UPS  $h\nu$  of a few 10 eV, therefore UPS probes only the upper one to two monolayers. However, the IMFP increases to both lower and higher photon energies. If it is larger than the film thickness, the band edges of both film and substrate,  $E_{V,film}$  and  $E_{V,sub}$ , can be evaluated in the

measured spectrum. Then, the valence band offset is simply  $\Delta E_V = E_{V,film} - E_{V,sub}$ . Using this direct approach, for example,  $\Delta E_V$  between amorphous (a-Si:H) and crystalline silicon (c-Si) has been measured to  $\approx 0.45$  eV with excitation in the near-UV range ( $h\nu \approx 4.07$  eV),<sup>[270,271]</sup> and monochromatized XPS ( $h\nu = 486.74$  eV) was used to measure  $\Delta E_V = 2.7(1)$  eV between ALD-deposited ZnO and a-Si:H.<sup>[272]</sup>

#### 4.4. Electrical Simulations

The electrical simulations of semiconductor devices in general, and of solar cells specifically, can be carried out on different levels of sophistication: one extreme consists in simulating the full semiconductor physics of all materials and their interfaces, often using advanced semiconductor device simulation software such as the commercial Synopsis TCAD,<sup>[275]</sup> or freeware such as PC1D,<sup>[276]</sup> SCAPS,<sup>[277]</sup> or AFORS-HET<sup>[278]</sup> that apply the drift-diffusion model (examples for silicon solar cells:<sup>[278,279]</sup> for perovskites:<sup>[23,280]</sup>; for organic bulk heterojunction cells:<sup>[281]</sup>). Such simulations help to gain detailed insights into the interplay of carrier generation, recombination, and transport in the device, and can yield information on performance-limiting factors such as internal barriers at heterojunctions, sensitivity to the density of recombination centers at different locations in the device, etc. The use of simplifying assumptions (e.g., low injection conditions, constant photogeneration throughout the absorber, etc.) allows finding semi-analytical solutions,<sup>[282]</sup> which can decrease computational cost at the expense of generality. Also, for the case of perovskites, coupled simulations of ion migration, and the concomitant redistribution of free charges have been carried out in order to understand hysteresis and degradation effects, see e.g. ref. [283] and [284]. Again, simplifying assumptions for the ion distributions can yield analytical solutions,<sup>[285]</sup> which would lend themselves, e.g., to multiparameter variation studies. A detailed review of the different approaches to such coupled drift and diffusion (of ions) and drift-diffusion (of electrons and holes) modeling as applied to perovskite cells can be found in ref. [286].

A caveat of such simulations is that they usually require a detailed understanding of the involved materials and interfaces: among others, the valence and conduction band energies need to be known as well as effective masses, carrier mobilities, energy levels, capture cross sections of defects, etc. This is not necessary for the network simulations that are at the other end of the spectrum of computational approaches. Here, equivalent circuit networks of current generators, diodes, and resistors represent the photogeneration current, carrier-selective junctions, and parallel and series resistances, respectively. Their J-V response is described by suitably parametrized analytical equations such as Ohm's law for resistors or the 1-diode equation for rectifying junctions, where the parameters can, e.g., be obtained from fits to experimental data. Such circuit simulators are often based on the approach first implemented in the SPICE software.<sup>[287]</sup> A modern, non-commercial implementation often used in microelectronics and PV is LTspice.<sup>[288]</sup> An example of such modeling to understand hysteresis in perovskite cells was published by Cojocaru,<sup>[289]</sup> where the specific Schottky diode equivalent circuit model is under debate, however.<sup>[290]</sup> Note, that similarly simplified network descriptions are used in analyzing impedance spectroscopy data to understand electronic and ionic processes in the bulk and at the interfaces of cells.<sup>[250]</sup>

Both drift-diffusion and network simulations of tandem and multijunction cells have been widely used to understand III-V multijunction,<sup>[291–294]</sup> III-V on Si<sup>[295,296]</sup> and amorphous/microcrystalline tandem solar cells, see e.g. ref. [297]. We note that a specific challenge in multijunction simulations using

drift-diffusion models often lies in the proper description of the internal tunnel-recombination junction, which usually requires models for field-dependent charge carrier mobilities and/or non-local trap-assisted tunneling models to describe charge transport and recombination in this high-E-field region.<sup>[292]</sup> In equivalent circuit network models, such tunnel junctions, also called Esaki diodes,<sup>[298]</sup> are often simply described with a series resistance. A more realistic approach is to use arbitrary J-V responses that correspond to a measured characteristic,<sup>[293]</sup> which then also allow to model the characteristic negative differential resistance of such tunnel diodes.

When it comes to electrical simulations specifically for perovskite-based tandem cells, to date the number of publications is quite limited. In the following, we briefly discuss three examples:

Rolland et al. have published drift-diffusion modeling of 2T perovskite/silicon tandem cells,<sup>[274]</sup> cf. Figure 12, top row. They explicitly model the all-silicon n<sup>++</sup>/p<sup>++</sup> tunnel junction interconnecting the sub-cells and find that doping levels of  $5 \times 10^{19} \text{ cm}^{-3}$  are sufficient to achieve good tunneling properties. Furthermore, they demonstrate an optimization of perovskite thickness and bandgap, yielding optimum values of 300–400 nm and 1.7 eV, respectively.

Regarding detailed drift-diffusion simulations of perovskite-perovskite cells, we mention the work by Singh and Gagliardi.<sup>[299]</sup> They use the finite element drift-diffusion implementation of the commercial TiberCAD package to simulate such tandems, varying parameters such as layer thicknesses and the work functions of contact materials. They assume a planar device stack of NiO as HTL/top cell perovskite/PCBM as ETL/recombination layer/PEDOT:PSS/bottom cell perovskite/C<sub>60</sub> as ETL. Using ideal absorbers, an optimum bandgap combination of 1.55 eV for the top and 0.95 eV for the bottom cell is found, with a PCE of 36.6%. Furthermore, the influence of various non-idealities such as bulk and interface traps, varying energy alignments at various interfaces in the device stacks as well as changing doping levels are investigated, using top and bottom perovskite thicknesses as free parameters.

Finally, we highlight Köhnen et al.'s equivalent circuit modeling used to understand the impact of current mismatch in 2T tandem cells: For the 2D device shown in Figure 5 (lower panel), the equivalent circuit model in Figure 12 was parametrized using measurements on individual cells. This allowed to model an effect found experimentally, namely an increase in the tandem's fill factor upon increasing current mismatch (Figure 12d), leading to a PCE that is less sensitive to current density mismatch (e).

#### 4.5. Radiative Characterization

The radiative characterization of solar cells provides insights into charge carrier recombination processes and allows to assess the quality of a semiconductor or the charge carrier dynamics at its interfaces. It is, therefore, a powerful tool to identify loss mechanisms in a device and gain implications about the electronic properties of an absorber. The methods described in the following are nowadays widely used for quality

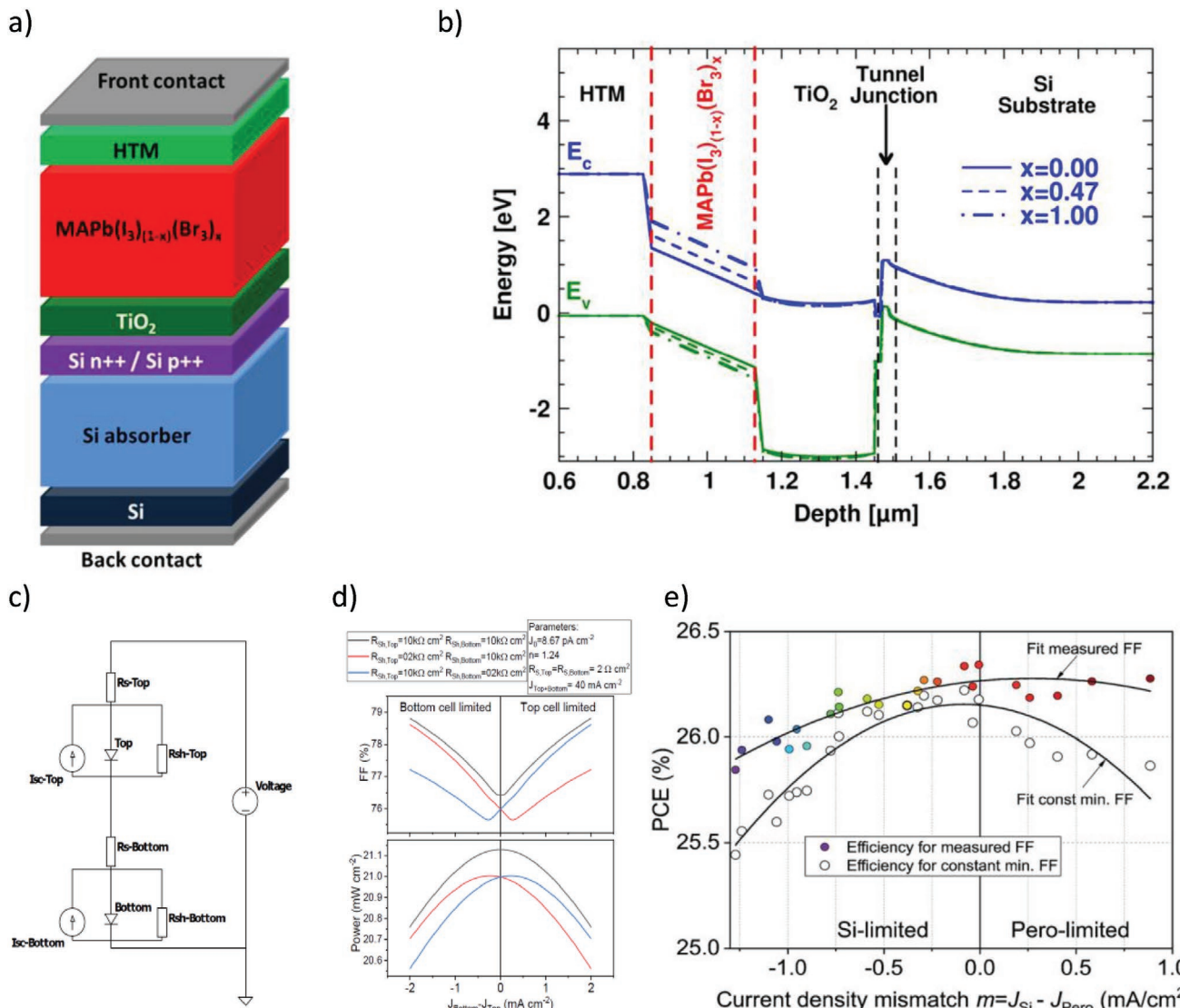


**Figure 12.** Drift-diffusion (top) and equivalent circuit (bottom) simulations of 2T perovskite/silicon tandem cells. Top: a) Schematic and b) simulated energy band diagrams. The position of the top cell absorber is highlighted between red dashed lines. The effect of halide composition on the bandgap in the HOP absorber  $\text{CH}_3\text{NH}_3\text{PbI}_{3(1-x)}\text{Br}_{3x}$  is illustrated for  $x=0.0$  (solid line), 0.47 (dashed line), and 1.0 (dashed dotted line). Reproduced with permission.<sup>[274]</sup> Copyright 2017, Springer Science+Business Media, LLC, part of Springer Nature. Bottom: c) Equivalent circuit, simulated fill factor and power output as a function of current density mismatch between top and bottom cell, and d) measured and simulated PCEs as a function of this mismatch, where also power density is shown when assuming that the  $\text{FF} = \text{FF}_{\min}$  and does not change with changing mismatch. Reproduced with permission.<sup>[68]</sup> Copyright 2019, The Royal Society of Chemistry.

control and failure analysis not only in research but also in PV industry, which highlights their significance.<sup>[300–302]</sup> Also, in perovskite tandem solar cells, those methods allowed to distinguish loss channels in the device or helped to enhance absorber qualities as discussed in more detail hereafter.

Photoluminescence (PL) measurements represent the most widely used technique to determine the radiative behavior of a solar cell. Photons are irradiated onto an absorber to excite electrons that can then recombine radiatively with holes and release their excess energy by emitting a photon. Alternatively, also cathodo- (CL) or electroluminescence (EL) measurements are possible. In these cases, photoemission is stimulated by exciting the sample with an electron beam or via electric

current injection, respectively. Detecting the emitted photons externally gives information about the quantity of radiative recombination events from the luminescence intensity and the energy of the recombined electron-hole pairs from the emission wavelength. These luminescence measurements, therefore, are a noninvasive, nondestructive characterization technique. In addition, PL and CL does not require a complete solar cell but can already be performed starting from a bare absorber. Besides, both sub-cells in tandem solar cells can be characterized individually by multiwavelength PL measurements to selectively excite charge carriers in the top or bottom cell by photons with energies well above or below the top cell bandgap energy, respectively.

As mentioned before, the emission wavelength of radiative recombination largely correlates with the absorber bandgap, as electron–hole pairs usually thermalize to the band edges before recombination. PL measurements have thus been used in photovoltaics to determine local variations in the absorber composition by PL mapping<sup>[303,304]</sup> or for perovskites to assess the bandgap energy or identify phase segregations upon bandgap tuning.<sup>[56,124,165,215,305]</sup>

Furthermore, the intensity of the luminescence depends among others (incident photon flux, carriers extracted from or injected to the cell) on the amount of nonradiative recombination. Ideally, all charge carriers excited in a solar cell under open circuit conditions recombine radiatively. However, imperfections such as defects within the absorber or at its surfaces can give rise to nonradiative recombination losses, which lower the radiative efficiency of the device and thus its maximum performance potential. More profound considerations on this topic can be found in refs. [24,306], and [307].

Qualitative comparison of the steady-state PL emission intensity from perovskite layers under constant illumination was for example used in low bandgap Sn-Pb mixed compositions to prove enhanced electronic quality and reduced nonradiative carrier losses upon addition of metallic Sn to the precursor solution.<sup>[15]</sup> Further, also perovskite/charge selective layer interfaces have been studied. Good contact layers should provide high PL emission at  $V_{OC}$ , i.e., low nonradiative interface recombination losses, but strong luminescence quenching at MPP conditions that correlates to efficient charge extraction.<sup>[310]</sup> The fullerene derivative IC<sub>60</sub>BA as contact layer for low bandgap MAPb<sub>0.5</sub>Sn<sub>0.5</sub>I<sub>3</sub> perovskites (without external voltage) was for instance shown to provide higher PL intensities as compared to C<sub>60</sub> and consequently allowed better  $V_{OC}$  values in an all-perovskite tandem device.<sup>[148]</sup>

Besides, PL intensity maps under constant illumination have therefore been demonstrated as a useful technique to determine spatial variations in the charge carrier recombination dynamics in tandem solar cells. Selectively exciting the individual sub-cells, as described above, allows to attribute loss regions to the top or the bottom cell. As an example, Figure 13a presents PL intensity maps for a monolithic perovskite-Si tandem solar cell with excitation wavelengths of 640 and 905 nm to individually probe the top and bottom cell, respectively.<sup>[308]</sup> The darker spots reveal regions in each sub-cell with higher non-radiative recombination losses and thus poorer electronic quality. PL intensity mapping can thus provide meaningful hints for further process optimizations.

To perform absolute PL measurements, the described method can be extended by utilizing a well-calibrated system that illuminates the sample under a one-sun equivalent excitation and detects the absolute, spectrally resolved number of photons being emitted from the sample. In this case, the emission spectrum can be related to an electrochemical potential of charge carriers in the absorber (or quasi-Fermi level splitting QFLS) that represents the maximum achievable  $V_{OC}$  of the solar cell.<sup>[311,312]</sup> This technique has already been applied to a range of PV technologies<sup>[304,313]</sup> and has recently lead to fundamental gains in understanding charge carrier dynamics in perovskite solar cells.<sup>[23,314,315]</sup> Also for tandem solar cells, absolute PL measurements can provide essential insights. Exemplarily,

such a measurement is presented in Figure 13b for a monolithic perovskite/CIGS tandem solar cell. The PL imaging technique reveals rather homogeneous PL emission with an average QFLS for the CIGS bottom cell of 0.613 eV (excitation wavelength 850 nm) and for the perovskite top cell of 1.086 eV (excitation wavelength 450 nm). This potential was however not fully retrieved externally, as the tandem  $V_{OC}$  value of this device measured in JV was around 100 mV lower than the sum of the QFLS divided by the elementary charge. This points toward a loss mechanism apart from the actual absorbers and their direct interfaces, e.g., at the sub-cells' interconnection junction. This example underlines the power of absolute PL measurements to selectively determine the quality of each sub-cell and identify the origin of voltage losses in tandem solar cells.

Besides the aforementioned measurement techniques with constant illumination, it is also possible to excite charge carriers in an absorber with a short light pulse and then monitor the temporal decay of radiative recombination processes after the pulse (transient or time-resolved photoluminescence or TRPL). As this method probes the dynamics of charge transport and recombination, it allows to determine carrier lifetimes in absorbers or get indications about charge extraction at contact layer interfaces.<sup>[24,214,316]</sup> For perovskite tandem solar cells, this method has been used to determine the carrier lifetime in bare absorber layers and thus as a quantitative measure of quality upon optimization of low or wide-bandgap perovskite sub-cells. For wide-bandgap perovskites, it was for instance shown that MACl and MAH<sub>2</sub>PO<sub>4</sub> additives<sup>[91]</sup> or increasing the amount of Cs in 1.74 eV bandgap FA<sub>0.75</sub>(MA<sub>1-x</sub>Cs<sub>x</sub>)<sub>0.25</sub>PbI<sub>2</sub>Br perovskite top cells<sup>[166]</sup> can enhance the TRPL lifetimes of charge carriers in the absorber and thus lead to higher device efficiencies. Similarly for low bandgap Pb-Sn mixed perovskite compositions, adding GuaSCN to the precursor solution (Figure 13c)<sup>[18]</sup> or post-deposition treatment of absorber layers with MACl vapor<sup>[44]</sup> was shown to increase the TRPL lifetime and consequently the  $V_{OC}$  and PCE in all-perovskite tandem devices. Besides, also the quality of contact layers can be evaluated by TRPL. Exemplarily, perovskite layers on a SAM hole selective contact revealed higher TRPL lifetimes as compared to layer stacks with PTAA as p-type contact. This implies lower nonradiative recombination losses at the perovskite/SAM than at the perovskite/PTAA interface and ultimately allowed higher device  $V_{OC}$  and PCE values. Even more, the SAM contact enabled a recent record efficiency for perovskite/CIGS tandem solar cells, as discussed before in Section 3.2.

The thermal emission of a solar cell can be analyzed to detect local hot spots by the so-called lock-in thermography mapping. In dark lock-in thermography (DLIT), a certain voltage is applied to a solar cell in dark with a lock-in frequency of typically few Hz. IR imaging of the device then allows to visualize the spatial change in temperature that typically represents the current distributions. Local hot spots therefore usually show regions carrying high currents (regions of low shunt resistance) in a solar cell.<sup>[302,317]</sup> This is exemplarily shown for an amorphous/microcrystalline (micromorph) Si tandem solar cell in the top left panel of Figure 13d where the labeled bright spots mark the shunted regions of the device.<sup>[309]</sup> However, the shunts detected by DLIT cannot be attributed to the originating sub-cell in tandem solar cells. Instead, selective illuminated

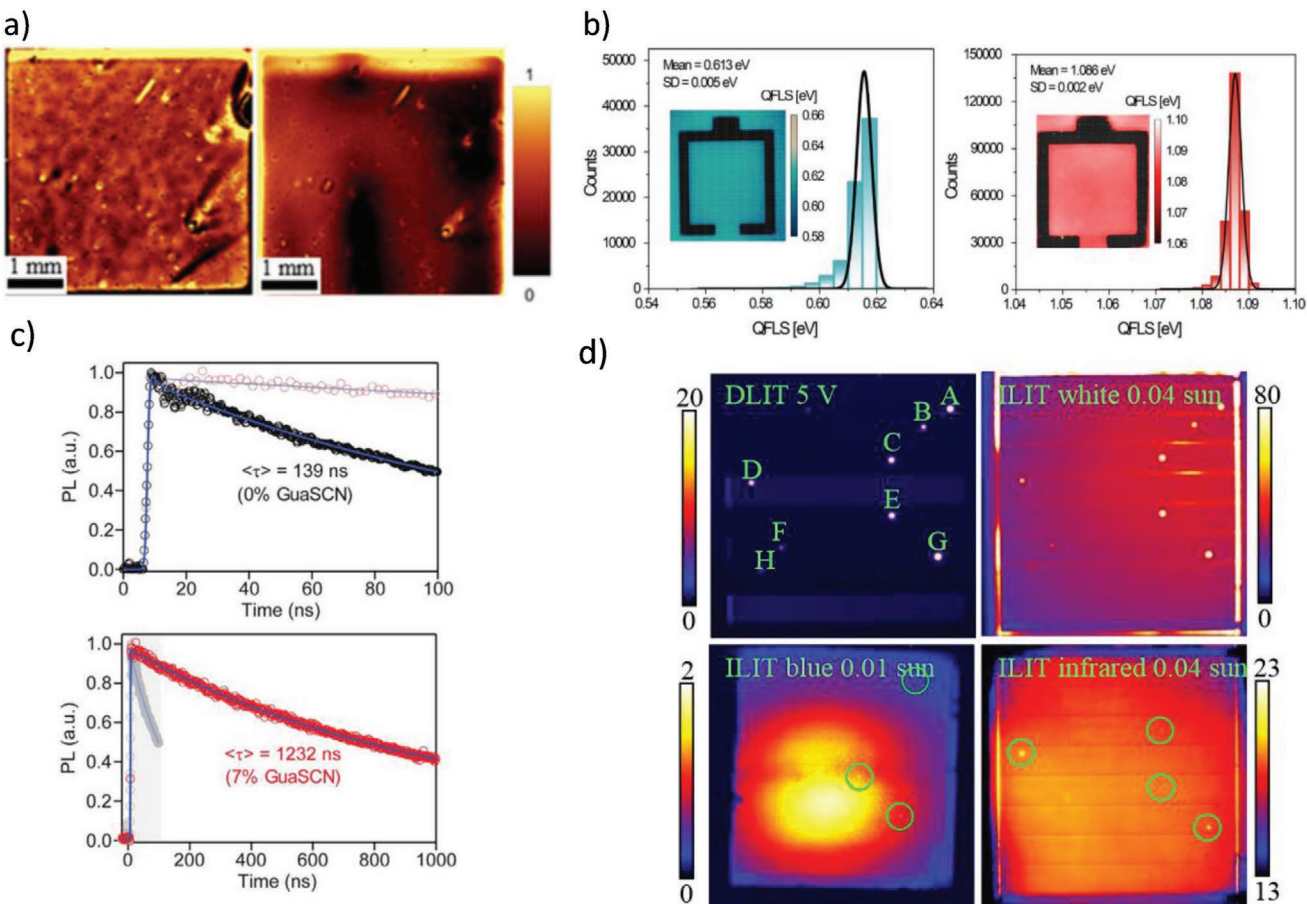


**Figure 13.** a) Photoluminescence (PL) intensity maps of a monolithic perovskite/Si tandem solar cell for different excitation wavelengths  $\lambda_{\text{exc}}$  selectively revealing spatial inhomogeneities in absorber quality for the perovskite top cell (left,  $\lambda_{\text{exc}} = 640 \text{ nm}$ ) and the Si bottom cell (right,  $\lambda_{\text{exc}} = 905 \text{ nm}$ ). Reproduced with permission.<sup>[308]</sup> Copyright 2017, IEEE. b) Hyperspectral PL imaging and corresponding quasi-Fermi level splitting (QFLS) distributions of the CIGS bottom (left,  $\lambda_{\text{exc}} = 850 \text{ nm}$ ) and perovskite top cell (right,  $\lambda_{\text{exc}} = 450 \text{ nm}$ ) for a two-terminal perovskite/CIGS tandem solar cell. Reproduced with permission.<sup>[62]</sup> Copyright 2019, ACS Publications. c) Transient PL measurements of low band gap ( $1.25 \text{ eV}$ )  $(\text{FASnI}_3)_{0.6}(\text{MAPbI}_3)_3$  perovskite thin films revealing a tenfold enhancement in charge carrier lifetime upon addition of 7% GuaSCN to the perovskite absorber. Reproduced with permission.<sup>[18]</sup> Copyright 2019, American Association for the Advancement of Science. d) Top left: Dark lock-in thermography image of a micromorph Si tandem solar cell revealing local shunts as bright hot spots. Top right: Similar shunts can be identified by illuminated lock-in thermography (ILIT) with white light illumination. Bottom: Selectively exciting the top or bottom cell in ILIT with blue or infrared light, respectively, allows to pinpoint shunts to the originating sub-cells. Reproduced with permission.<sup>[309]</sup> Copyright 2011, Wiley.

lock-in thermography (ILIT) measurements can be performed. In this case, the sample is held at open circuit conditions and is periodically illuminated, causing shunted regions with strong nonradiative recombination losses of the excited charge carriers to heat up more than their surroundings. This is depicted for the previously mentioned micromorph tandem cell for a white light illumination in the top right panel of Figure 13d, revealing similar shunted regions as the DLIT measurement. A selective excitation of the bottom or the top cell can be achieved by using lower or higher energy photons similar to the PL measurements introduced before. As illustrated in the bottom panels of Figure 13d, this allows to pinpoint the origin of the shunts across the tandem stack. Although there are so far no reports of DLIT/ILIT measurements on perovskite tandem solar cells, it presents a powerful method to identify shunt losses and optimize device fabrication. It has been widely used for failure analysis of solar modules in photovoltaics<sup>[300,302]</sup> and even for perovskite mini-modules.<sup>[318]</sup>

#### 4.6. External Quantum Efficiency Spectra

The external quantum efficiency (EQE) spectra is a powerful characterization method that allows to measure the efficiency of converting incident photons with certain energy to collected charges in solar cells. With that, important information on absorption losses in the layer stack, charge collection losses can be collected. In addition, the bandgap of the solar cell can be determined from the EQE spectra within the low energy onset region by, e.g., using the inflection point.<sup>[81]</sup> To measure the EQE spectra, typically light from a broad emitting lamp (halogen and/or xenon) is converted to monochromatic, chopped light. This chopped monochromatic light is used to generate the photocurrent that is amplified and detected with the help of a lock-in-amplifier. This helps to be less sensitive against non-chopped, e.g., room or bias light and to improve the signal-to-noise ratio. The intensity of the monochromatic light is typically calibrated with referenced photodiodes that

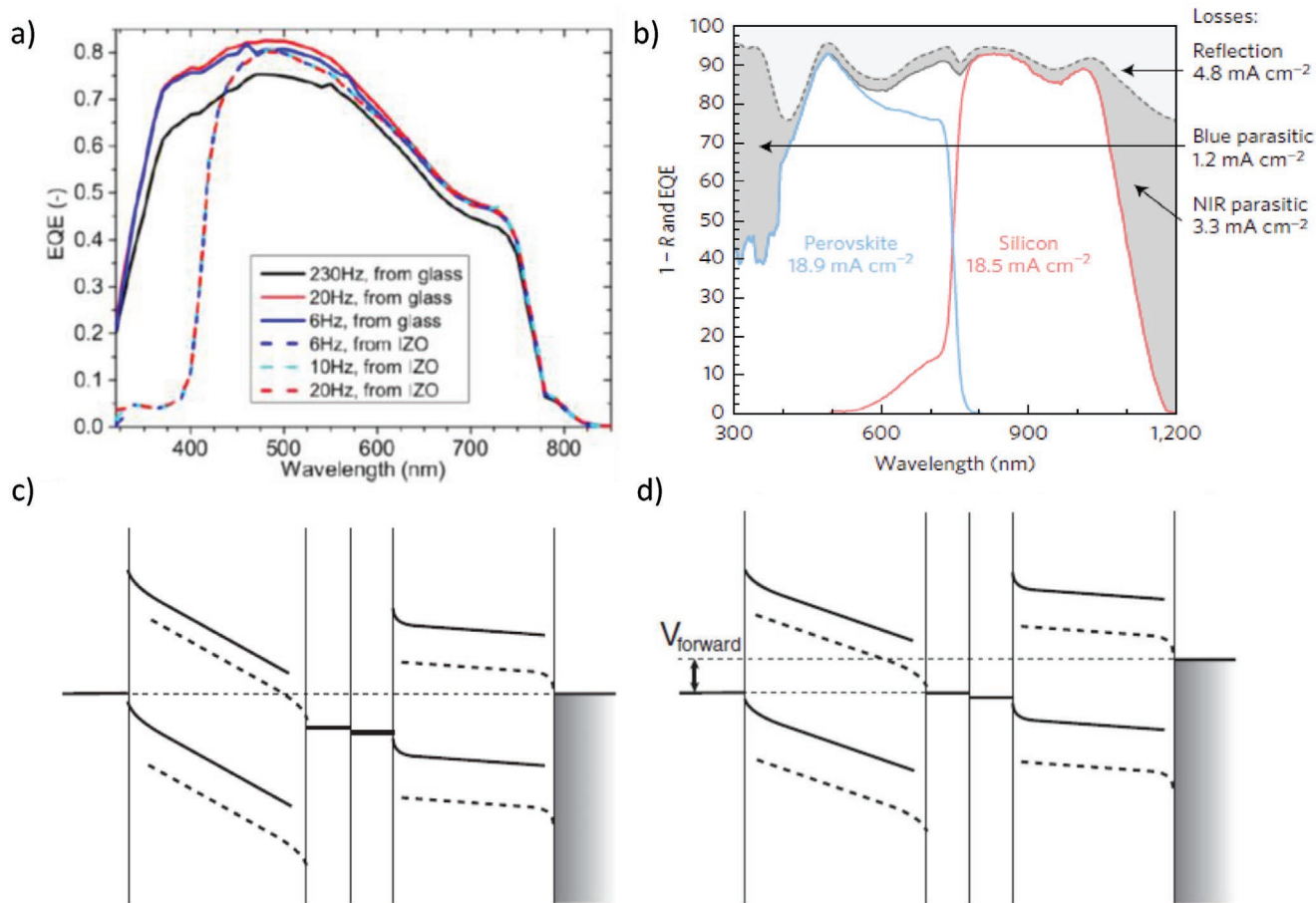


**Figure 14.** a) External quantum efficiency (EQE) spectra of semitransparent perovskite cell measured with different frequencies of chopped light and different illumination conditions as indicated in the legend. Reproduced with permission.<sup>[186]</sup> Copyright 2015, Elsevier. b) EQE spectra together with 1-reflection and the sum of the sub-cell EQEs for a 2T perovskite/Silicon tandem cell. Reproduced with permission.<sup>[55]</sup> Copyright 2017, Springer Nature. c,d) The energy diagram of c) a 2T organic tandem cell under bias illumination and external short circuit and d) by applying a forward to bias to compensate for the photovoltage of the optically biased (right) cell to have the cell under measurement (left) in short circuit. Reproduced with permission.<sup>[53]</sup> Copyright 2010, Wiley.

have been calibrated elsewhere but it is well below that of one sun conditions.

To measure the two sub-cell EQE spectra of a monolithic tandem cell with only two terminals means to selectively address the spectra of the individual sub-cells. This is typically achieved with bias light and voltage conditions as follows:<sup>[53]</sup> First, in addition to the chopped and monochromatic measurement light that is used to selectively measure the response of the bottom cell, an intense monochromatic continuous wave (cw) light source (e.g., a blue LED) is utilized to saturate the top cell. With that, charge carriers are created in the top cell and the charge carriers generated with a monochromatic light in bottom cell have their counterparts in the top cell to recombine and be extracted without losses. However, the saturated top cell will induce a photovoltage and when short circuit conditions are applied to the overall tandem, to measure the EQE at this condition, the bottom cell is shifted toward the negative value of the top cell photovoltage. This can be nicely seen in Figure 14c and was shown by Gilot et al. who specifically summarized the EQE measurements for 2T organic solar cells.<sup>[53]</sup> In order to avoid the cell under measurement to drift away

from short circuit condition, a compensation voltage is applied externally, which compensates the photovoltage of the optically biased sub-cell, see Figure 14d. In addition, the monochromatic measurement light is typically much lower as compared to the intensity under one sun AM 1.5G condition. For sub-cell with strong intensity-dependent charge carrier density, this would lead to over or underestimation of the EQE signal. However, for most well-performing perovskite materials, the dependence of the photocurrent at short circuit condition is rather linear in the range between 0.01 and 10 suns and thus an exact intensity correction, as presented by Gilot et al.,<sup>[53]</sup> is neglected in most perovskite tandem EQE reports.<sup>[319]</sup>

For perovskite tandems that show significant hysteresis (see Section 4.7 for the explanation and further references of hysteresis) for time scales in the order of the chopping frequency used to feed the lock-in amplifier, the frequency dependence should be tested as well. Figure 14a shows a chopper frequency dependence as reported by Werner et al.<sup>[188]</sup> Here, it can be seen that for very high chopping frequencies, a reduction in the EQE spectra is reported, which indicates that photocurrent extraction is hampered by the transient property of ionic motion

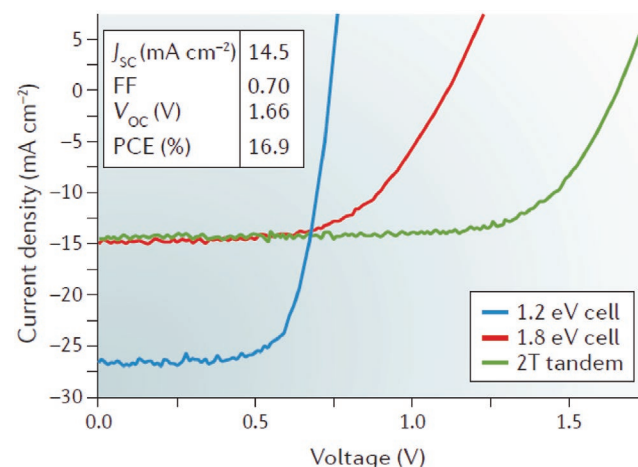
within the absorber layer.<sup>[320]</sup> Another interesting feature is seen in this EQE spectra, namely the response in the UV and blue light region, depending on the illumination direction. When the sample is illuminated from the IZO side (the top contact), strong absorption losses reduce the EQE response in the blue as light is parasitically absorbed in the top contact layers, here MoO<sub>3</sub> and Spiro-OMeTAD, and cannot contribute to photocurrent collection.

Figure 14b displays the EQE spectra of both sub-cells from a 2T perovskite/silicon tandem cell together with the reflection (1-R) and the sum of both sub-cell EQEs.<sup>[55]</sup> This set of data clearly indicates all the important optical losses in the tandem stack. The gray area is parasitic absorption loss amounting to a photocurrent loss of 4.5 mA cm<sup>-2</sup>. This light is absorbed by the contact layers, the recombination contact, and the back electrode. Typically, the UV and blue light are predominantly absorbed by the top contact and the NIR by the back contact. Comparing the sum of the EQE spectra with the reflection should yield a smooth curve that represents the absorption losses as a sum of the individual layers. Comparing this to an optical simulation enables simple quantification of the individual parasitic losses.

Overall, the relative EQE spectra (only the shape, not the absolute values) are highly important for the correct mismatch correction of the JV measurement (see also Section 4.7). In order to adjust the sun simulator spectra to reduce and correct for spectral mismatch of a 2T tandem, the relative EQE spectra of both sub-cells are needed. Therefore, this measurement is needed to report reliable tandem efficiency data and is typically measured in calibration laboratories before J–V characterization and efficiency are certified. Note that for strongly emitting sub-cells with high radiative yields, the relative EQE spectra might be affected by the emission of the sub-cell that is optically biased and a correction might be needed.<sup>[321]</sup>

#### 4.7. Current–Voltage Characterization

A current–voltage (J–V) measurement under simulated AM 1.5G illumination is the standard characterization technique that all solar cells have to undergo to assess their overall device performance and thus efficiency as well as metrics such as short circuit current,  $J_{SC}$ , open-circuit voltage,  $V_{OC}$ , and fill factor, FF. For monolithic tandem solar cells with series connection, the tandem J–V curve is a function of the single-junction or sub-cell curves as shown in Figure 15. The figure shows the typical J–V curves. The low bandgap bottom cell usually provides higher  $J_{SC}$  and lower  $V_{OC}$  due to the low bandgap, as compared to the wider bandgap single-junction. When both sub-cells are combined in the monolithic tandem connected in series, the voltages of each sub-cell add up and the current is that of the limiting sub-cell in good approximation, especially when both sub-cells have high shunt resistances.<sup>[8]</sup> Note that the tandem current can be higher than the limiting sub-cell when this shunt resistance is low. This feature is visually explained by Ameri et al.<sup>[322]</sup> In the tandem configuration, only the light being transmitted by the top cell can be absorbed by the bottom cell and for ideal performance, both sub-cells should be operating close to current matching conditions. Note that



**Figure 15.** Current voltage curves for 1.2 eV low (blue) and 1.8 eV wide (red) band gap perovskite single-junctions and the 2-terminal (green) perovskite/perovskite tandem solar cell. The inset shows the performance metrics extracted from the tandem device. Reproduced with permission.<sup>[84]</sup> Copyright 2017, Springer Nature.

the highest performance is achieved when the currents at MPP are matched ( $J_{MPP\_top} = J_{MPP\_bottom}$ ). This can be different from current matching at short-circuit conditions ( $J_{sc\_top} = J_{sc\_bottom}$ ). The series connected 2T tandem J–V curve can be reproduced fairly well by adding the sub-cell voltages at each current density value.<sup>[60,63]</sup> With that, the predicted and measured J–V curves can be compared and individual losses, e.g., in the recombination layer, can be extracted. This is the case when the tandem  $V_{OC}$  is not close to the sum of the single cell  $V_{OCs}$ .<sup>[62]</sup> For combination of sub-cells with significant differences in FF, the tandem J–V will likely yield FF values limited by the lower FF sub-cell.<sup>[322]</sup> For sub-cells with rather high and equal FFs of the sub-cells, the tandem FF can be even higher than the individual sub-cell's FFs and is a function of mismatch<sup>[68]</sup> (see also the lower panel of Figure 12).

The J–V measurements in general are standardized and, in principle, also provide the basis for certification. Detailed procedures can be found in the IEC Standard 60904-3<sup>[323]</sup> and related guidelines, e.g., for publications on PV devices.<sup>[324]</sup> However, these standards and guidelines were established for “well-behaved” solar cells, i.e., devices that are stable over long periods and give reproducible J–V curves in a wide range of measurement conditions. Yet, it is well established that in perovskite cells, hysteresis effects and/or slow transient phenomena can contribute significantly to the J–V response. Thus, similar effects are also seen in perovskite-based tandems. Such hysteresis is evident in the J–V data presented in the previous sections, e.g., Figure 4, 7, or 5. In devices showing hysteretic behavior, the shape of the J–V curve typically depends on the direction of the J–V sweep (i.e., if it is carried out from the  $J_{SC}$  to the  $V_{OC}$  point (“forward” direction), or in the opposite, “reverse” direction) and the sweep rate (rate of change of the voltage applied to the cell terminals [V s<sup>-1</sup>]). Furthermore, the cell's history prior to the J–V measurement can play a substantial role, e.g., light soaking, applying bias voltages for extended time periods, etc. The reasons for such hysteresis can be broadly categorized into two groups: on the one hand, the redistribution

of ionic charge carriers within the perovskite absorber film can yield changes in the distribution of the electrical field within the perovskite cell.<sup>[320,325,326]</sup> On the other hand, charge carrier trapping/detrapping in defect states at its interfaces to the electron and hole contacts can also influence the local electric field due to recharging, but will also influence recombination and carrier extraction rates at these interfaces.<sup>[327,328]</sup> A detailed discussion of these phenomena on the microscopic level is out of the scope of this manuscript. Instead, we aim at outlining how to perform meaningful  $J$ - $V$  and related measurements in perovskite-based 2T tandem cells despite such hysteresis in the perovskite cell, in order to quantify reliably their electrical performance.

Over the last years, several authors have published recommendations for best practices in (single-junction) perovskite solar cell measurements, at different levels of sophistication.<sup>[329–333]</sup> For a monolithic tandem cell, the procedure differs slightly as follows:

- Measure the active area or the aperture area precisely with an optical microscope, especially for small active areas this might be a source of significant error.<sup>[334]</sup>
- Measure properly the EQE spectrum of all sub-cells (see chapter above), for the mismatch correction only the relative spectrum is needed and no absolute values enter the correction.
- With the EQE spectrum of both sub-cell and your reference solar cells that ideally have low mismatch with your sub-cells, calibrate the illumination source (see description below).
- Record forward and reverse scan  $J$ - $V$  curves ideally at various scan rates and extract metrics such as  $V_{OC}$ ,  $J_{SC}$ , and FF.
- Measure steady-state photocurrent at several voltages near  $P_{MPP}$ , perform a maximum power point tracking over several minutes, track the metrics  $V_{MPP}$  and  $J_{MPP}$ .
- Compare the measured  $J_{SC}$  with the integration of the EQE spectra and check for self-consistency.
- Monitor performance metrics and thus stability over time, the first days to weeks after fabrication.
- Perform statistical analysis across multiple sample sets to verify changes.
- Certify your results by accredited and independent calibration laboratory.

The most critical part for a 2T tandem cell is the correct calibration of the light source in order to account for spectral mismatch.<sup>[335]</sup> Thus certification laboratories usually measure the EQE spectrum first to properly calibrate the sun simulator. Most of the certified tandem results from Table 1 were certified by the accredited calibration labs NREL and Fraunhofer ISE. Both laboratories have slightly different protocols to do the proper mismatch correction, however, with similar results based on direct comparisons.<sup>[335,336]</sup> We describe here the protocol used by Fraunhofer ISE: To do the mismatch calibration for a tandem solar cell (two sub-cells), the sun simulator ideally has two separate light sources (e.g., different lamps or LEDs) that can be independently controlled in intensity. These independent light sources should ideally have low spectral mismatch with the sub-cells such that the photocurrent generation in each sub-cell is mainly caused by one or the other light source. For, e.g., the perovskite/silicon tandem, one light

source should primarily emit in the visible and the other in NIR regime. In addition, a set of certified reference solar cells needs to be used. These reference cells should also have low spectral mismatch to the sub-cells, i.e. by using an appropriate filtered reference cell. With this system, the mismatch correction factors can be calculated and used to set the intensity for each of the two light sources by:<sup>[335]</sup>

$$J_{SC\text{ref,top}} = A_{\text{top}} \int S_{\text{ref,top}}(\lambda) \times e_{\text{sun,top}}(\lambda) d\lambda \quad (2)$$

$$J_{SC\text{ref,bot}} = A_{\text{bot}} \int S_{\text{ref,bot}}(\lambda) \times e_{\text{sun,bot}}(\lambda) d\lambda \quad (3)$$

In these equations,  $e_{\text{sun,top}}(\lambda)$  and  $e_{\text{sun,bot}}(\lambda)$  are the relative sun simulator spectra (only the shape, not the absolute values) for the top and bottom cell light source, respectively.  $S_{\text{ref,top}}(\lambda)$  and  $S_{\text{ref,bot}}(\lambda)$  are the absolute spectral response spectra for the top and bottom cell reference solar cells. The prefactors  $A_{\text{top}}$  and  $A_{\text{bot}}$  are then calculated from the measured relative spectra  $e_i$  and spectral responses  $S_i$  as well as the measured  $J_{SC\text{ref,top}}$  and  $J_{SC\text{ref,bot}}$  for the top and bottom cell reference solar cells, respectively. Then, the solar simulator is adjusted in intensity for each of the light sources independently until both equations above are fulfilled. It is assumed here for simplicity that the change in intensity only changes the absolute values and not the relative spectra  $e_{\text{sun,top}}(\lambda)$  or  $e_{\text{sun,bot}}(\lambda)$  of the light source. If this is not the case, an iterative approach is necessary.<sup>[335]</sup>

#### 4.8. Stability Characterization

As perovskite materials are prone to degradation induced by decomposition reactions catalyzed by moisture, oxygen, and thermal energy, a proper device stack and encapsulation is necessary for the tandem solar cells. In order to enhance the stability, several routes have been published recently on three different levels that we just quickly summarize: i) the intrinsic stability of the neat absorber materials was enhanced by reducing the number of ionic defects in the bulk, passivating the grain boundaries and surfaces as well as applying hydrophobic perovskite surface treatments. Bulk defect reduction can be enabled via additives.<sup>[27,337]</sup> ii) the device stability was improved by applying charge extraction and contact layers that hamper degradation. Here metal oxides from ALD and/or sputtered layers<sup>[192,338]</sup> are a good alternative to metals that either diffuse into the absorber or react with it.<sup>[153]</sup> Thick metal oxide layers help to prevent moisture ingress and effusion of decomposition products.<sup>[338]</sup> iii) single and tandem solar cells are encapsulated properly via glass/glass sheets and sealed with UV curable glue.<sup>[339,340]</sup> For industrialization, though this will not be enough. Instead, a proper encapsulation with encapsulants is needed, for which the commonly used EVA might not be suitable due to acetic acid damaging the perovskite.<sup>[339,341]</sup> A detailed review on the stability of perovskite solar cells can be found in.<sup>[342–345]</sup> Recently, a consensus statement for stability assessment and reporting for perovskite (single-junction) solar cells has been agreed and published.<sup>[346]</sup> The testing and reporting protocols were revised and updated based on similar standardized aging experiments for organic PV. Those protocols

include dark storage, bias stability, light-soaking, outdoor stability, and thermal and/or light cycling. In the literature, each report covers only a small number of the proposed protocols. However, in the future, all the protocols will have to be considered and tested in order to find all the relevant aging conditions for perovskite single-junction solar cells and establish their relevance for testing perovskite-based tandem solar cells.

In order to measure the long-term stability of perovskite single cells and tandems, typically long maximum power point (MPP) tracking over several hundred hours is applied.<sup>[38,63,348,349]</sup> Most stable perovskite single cells reach T80 stabilities (the time when they are degraded to 80% of the initial performance) of >1000 h.<sup>[349,350]</sup> The stability also depends strongly on the measurement conditions, such as regulated device temperature at 25 °C, full illumination including UV irradiation, and the atmospheric conditions such as oxygen and moisture levels. A good practice of writing these conditions directly into the MPP tracking figures has evolved for better comparison.<sup>[351–353]</sup>

Long-term MPP tracking of tandem solar cells is only rarely reported in the literature. **Figure 16** displays the reported data for all three tandem technologies discussed in this review. Figure 16a highlights the data by Sahli et al. and shows the constant MPP tracking of a glass/glass-encapsulated perovskite/silicon tandem cell over the time of 250 h. Every 5 min a complete JV scan is performed and the inset shows the recovery at MPP from the previous J-V scan. Overall the cell retained

90% of its initial PCE after 270 h of constant MPP tracking. In the first 20 h of illumination, an exponential decay was observed (so-called “burn-in”),<sup>[344]</sup> followed by a linear regime for the next 250 h. The burn-in potentially happens due to photochemical reactions changing the trap states under illumination, increasing the energetic disorder either in the absorber or at the interfaces.<sup>[354]</sup> It is unclear yet why some devices undergo this effect and some not. Figure 16b is reproduced from Han et al. and displays stability data for perovskite/CIGS tandem solar cell. The MPP track revealed a quick initial decay in PCE over the first 100 h of MPP tracking, with a minor and more linear drop in PCE after this time. Overall, the T90 time is comparable to Sahli’s report and <15% in PCE was lost over 500 h of tracking, despite no encapsulation. For the all-perovskite tandem in Figure 16c, a T90 time of 463 h has been reached, after 463 h of tracking in a glovebox, the PCE dropped by only 10%. No initial burn-in was measured, however, the testing was performed in an inert atmosphere. These results show that not only the device PCE has been improved with the fabrication progress but also their MPP stability. The few tandem stability reports clearly highlight the need for unified measurement protocols regarding the MPP tracking conditions, the illumination spectra and atmospheric conditions as well as encapsulation utilization to enable more robust comparisons and the verification of differences between the herein summarized perovskite-based tandem solar cells.

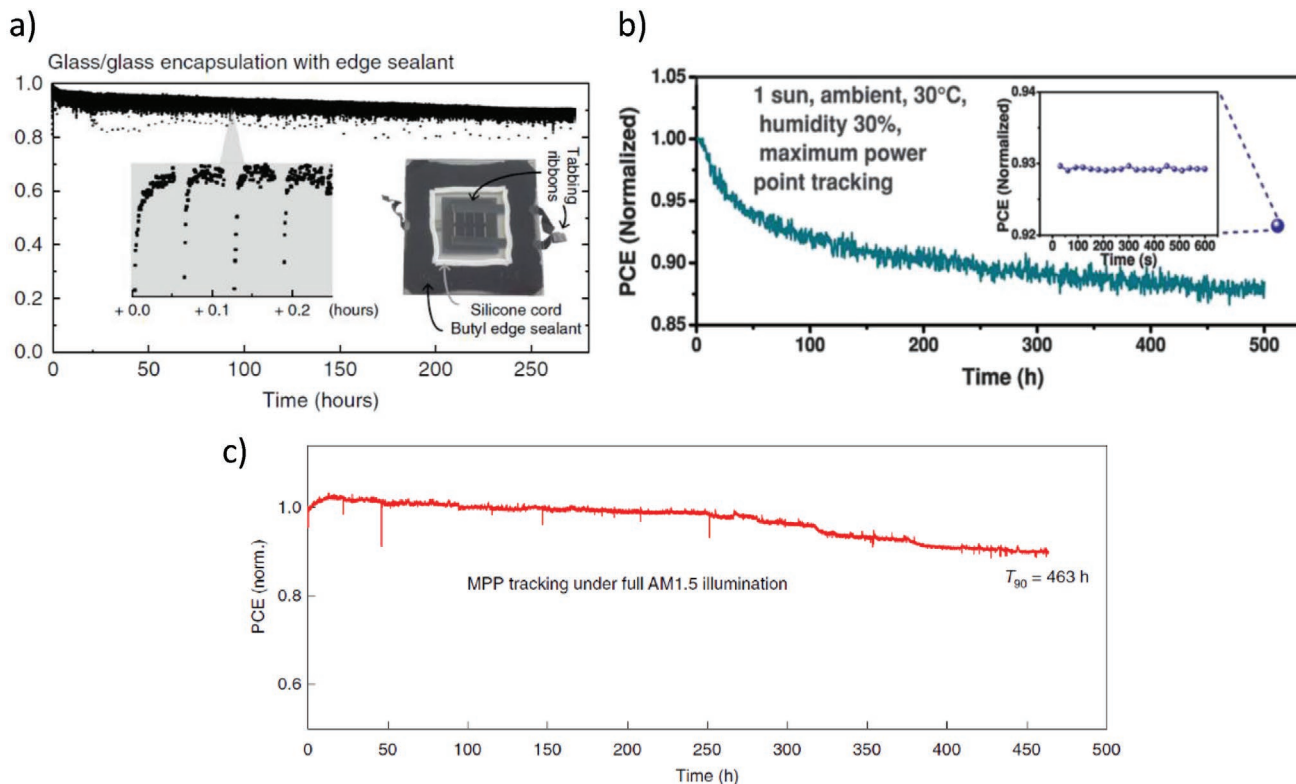


**Figure 16.** Long term stability measurements (normalized data shown only) based on prolonged MPP tracking for a) perovskite/silicon, b) perovskite/CIGS, and c) perovskite/perovskite tandem solar cells. The inset in (a) shows the encapsulated cell and the recovery from the J-V scans taken every 5 min. Reproduced with permission.<sup>[38]</sup> Copyright 2018, Springer Nature. In (b), the measurement conditions as well as the MPP track after resting the device in dark for several hours are shown. Reproduced with permission.<sup>[63]</sup> Copyright 2018, The American Association for the Advancement of Science. The T<sub>90</sub> time as displayed in (c) is the time when 90% of the initial performance is reached after continuous tracing. Reproduced with permission.<sup>[15]</sup> Copyright 2019, Springer Nature.

Despite these already exciting results, to pass the IEC standardized test, other requirements are needed. A thorough overview of international standards for stability of photovoltaic devices can be found in ref. [355]. Among them, the devices have to survive accelerated aging in the so-called 85/85 damp-heat tests, where they are exposed to a temperature of 85 °C and 85% relative humidity in addition to temperature cycling between –40 and 85 °C, as well as UV preconditioning. Compared to MPP tracking, these tests require more complex equipment and are therefore less often reported in literature, mostly for single-junction device. Those reports show good stability in the 85/85 test<sup>[55,340]</sup> and also for temperature cycling.<sup>[339,341]</sup> Ensuring good encapsulation and/or barriers in the device, perovskite solar cells can survive even device temperatures of 100 °C.<sup>[192]</sup>

The above mentioned IEC standards already test the device with harsh conditions, thus their positive results give high optimism for perovskite industrialization. In addition, good encapsulation can suppress outside factors, such as humidity and oxygen. Nevertheless, due to perovskite ionic nature, the real operational conditions might cause additional challenges. Namely, the day-night cycling will cause the regular ion redistribution and current mismatch due to spectral changes will increase the not extracted charge carrier accumulation in the perovskite sub-cell. Since the  $V_{OC}$  stability is usually lower than the MPP,<sup>[356]</sup> this might open new pathways for interaction between the module and inverter electronics and the cells realizing optimized recovery conditions.

There are also some other stability aspects before perovskite-based tandems can enter the real operation. Among them are potential induced degradation and reverse bias stability. Neither has been in-depth analyzed, however, the reports show that a much lower reverse bias can be applied to perovskite solar cells ( $\approx$ 1.5 V) compared to silicon ones, with strong dependence on perovskite solar cell layout.<sup>[357,358]</sup> This shows that not only perovskite but also supporting layers play a crucial role in reverse bias stability. If the reverse bias stability of perovskite cannot be improved, the amount of bypass diodes per module will have to increase.

## 5. Outlook Toward Overcoming 30% Power Conversion Efficiency

Following the herein presented trend over rapidly increasing device performance for all perovskite-based tandem solar cells as well as the ability to apply numerous advanced characterization methods, the PCE of record tandem devices is likely to increase further. In Figure 17, we thus compare the PCE potential for the three different perovskite-based tandem solar cells. The figure visualizes the state-of-the-art of each solar cell performance parameter,  $J_{SC}$ ,  $V_{OC}$ , FF, and PCE. These values are compared to the detailed balance limit (DBL) for multi-junction devices as well as to our own empirical limit, for the respective bandgap combination for the tandem absorbers. The basis for the figure are the best tandems reported so far for perovskite/silicon, perovskite/CIGS, and all-perovskite by the company Oxford PV (28%), Al-Ashouri (23.3%), and Lin (24.8%), respectively,<sup>[13–15]</sup> see also Table 1. To ensure a fair comparison, we keep the bandgap combinations identical to those reported for

the three record devices. Based on the band gaps, we calculated the DBL for the series-connected tandem solar cell, following the approach by Brown and Green.<sup>[359]</sup> As these experimentally utilized bandgap combinations are not perfectly matched, the DBL (first column) is well below the 45% predicted for more optimized band gaps such as 1.1 and 1.72 eV, which is depicted by the dashed line in the PCE plot (Figure 17d). For the empirical limit, we assumed the following for the individual parameters: i) the  $J_{SC}$  is derived from optical simulations from Jost et al. for perovskite/silicon<sup>[92]</sup> and using the same procedure for perovskite/CIGS. For all-perovskite tandems, we assume that 90% of the  $J_{SC}$  within the AM 1.5G spectrum for a 1.2 eV bandgap is available (see Figure 3b) and is equally distributed between the two sub-cells. These assumptions include realistic, mostly unavoidable losses from parasitic absorption. ii) For the  $V_{OC}$ , we assume realistic best values for Si and CIGS bottom cells to be 720 and 710 mV, respectively, under reduced illumination as in the tandem architecture.<sup>[62,69]</sup> For the perovskite top and bottom cells, we assume ca. 94% of the  $V_{OC}$  in the SQ limit, which has been shown for 1.5 eV perovskite band gaps (see Figure 3a)<sup>[360]</sup> and use values of 873 mV for the bottom cell, respectively. The  $V_{OC}$  of the perovskite bottom cell was reduced due to the lower light intensity in the tandem configuration, similarly as the silicon and CIGS one. iii) As our calculations show that the tandem FF in the DBL limit is only slightly higher than the FF of the individual sub-cells, we also adapted the tandem FF to be in the range of best single-junction solar cells. For wide-bandgap perovskite and for silicon, FFs above 84%, while for CIGS and low band gap perovskites, FFs of 80–81% can be found in the literature.<sup>[95]</sup> Thus, we assume 84% for the perovskite/silicon and 82% for the perovskite/CIGS and all-perovskite tandem FFs in the empirical limit. With that, we can compare the three different values, i.e., the detailed balance limit, the best experimental value, and our empirical limit, for all performance parameters and tandem technologies.

Starting with the  $J_{SC}$ , it is obvious that the experimental record values of tandems with silicon and CIGS are already fairly optimized. This was also achieved by the extensive optical simulations that were derived for these tandems (see Section 4.2.2). Recent simulations for double-sided textured device yielded a  $J_{SC}$  of 20.5 mA cm<sup>-2</sup><sup>[92]</sup> which is very close to the reports of Oxford PV and Sahli et al.<sup>[13,38]</sup> Further improvements are possible in developing a more transparent front contact and improving the NIR response of the bottom cell. Note that the empirical limit is slightly higher as the DBL being counterintuitive at the first place due to the following reasons: i) non-optimized bandgap combination and step like absorption in the DBL limit are considered with band gaps as found in the experiment (no overlapped absorption between the sub-cells in DBL), wherein the empirical limit realistic absorption onsets and layer thicknesses are considered, and ii) for silicon also phonon-mediated absorption below the optical band gap improves the near-infrared response.<sup>[361]</sup> Looking at the experimental  $J_{SC}$  of all-perovskite tandem cells, however, it is well below the DBL and the empirical prediction from Figure 3a, even when utilizing realistic optical losses. The reason for this can be found in optical limitations of the Sn-Pb low bandgap perovskite cells near the bandgap wavelengths. Therefore, to generate more photocurrent in the NIR region,

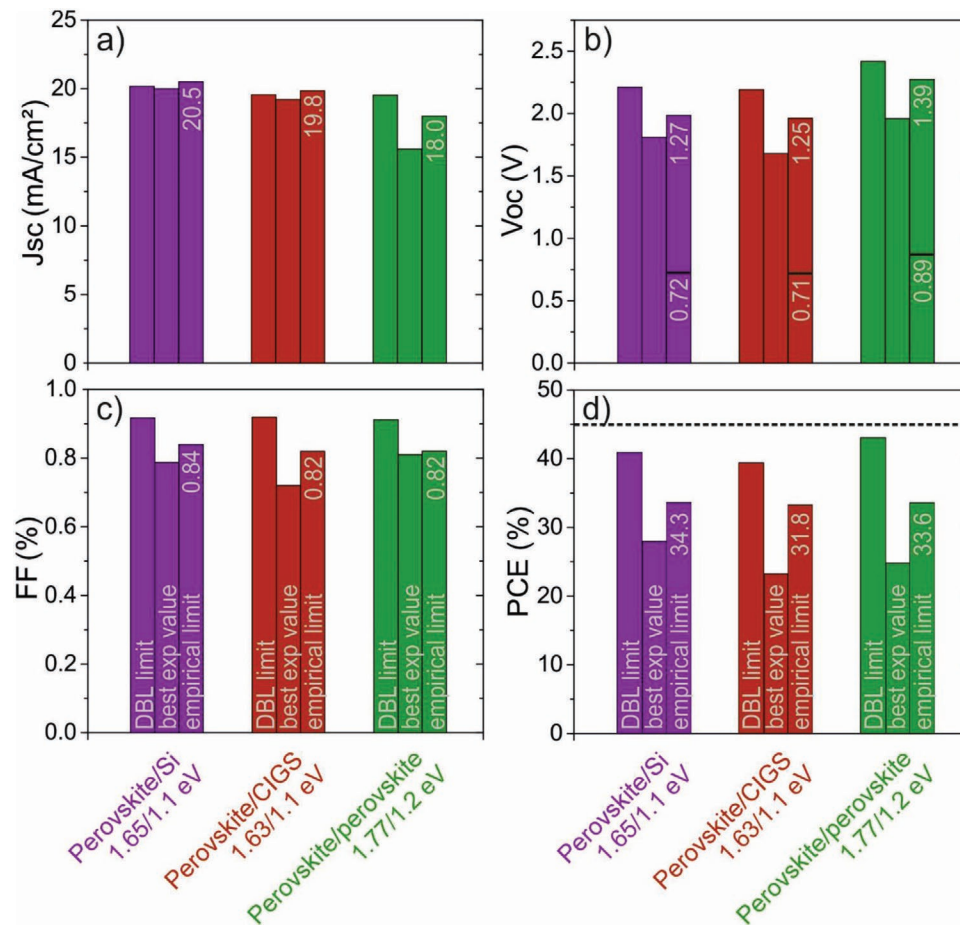


**Figure 17.** Comparison of performance parameters for all perovskite-based tandem solar cells reviewed herein based on the detailed balance limit (DBL) for series-connected tandem solar cells limit based on the bandgap combination for the experimental best value from Table 1 and our empirical limit that is derived as explained in the text for these bandgap combinations. For perovskite/silicon and perovskite/CIGS, the bandgap combinations of 1.65/1.1 and 1.63/1.1 eV were used, respectively. For perovskite/perovskite, the 1.77/1.2 eV was considered.

even thicker films are necessary (see Figure 7c).<sup>[69]</sup> In addition, the use of AR coatings for the superstrate glass and circumvention of metal as a recombination or buffer layer will reduce parasitic losses due to reflection and parasitic NIR absorption. Further optical simulations and potential light trapping strategies are necessary for all-perovskite tandem solar cells to improve light management as has been done for the other tandem technologies, in addition to electronic characterization to improve the recombination layer.

The experimental  $V_{OC}$  is lower than empirical estimation for all three tandem technologies, which is mostly related to the fact that the wide bandgap top cells do not reach  $V_{OC}$  values of their  $\approx 1.5$  eV bandgap analogs yet (see Figure 3a). The slightly higher difference for CIGS tandems is explained by i) the CIGS bottom cell  $V_{OC}$  that is lower for the experimental best tandem as compared to CIGS single-cell records. Note that the record  $V_{OC}$  (but not PCE) perovskite/CIGS device has similar  $V_{OC}$  as the record perovskite/silicon device. For all-perovskite the top cell requires an  $\approx 1.77$  eV bandgap that has a higher nonradiative recombination loss than the  $\approx 1.63/1.65$  eV analogs utilized for the other two tandem solar cells. Thus the main challenge toward the empirical limit is improving the  $V_{OC}$  of perovskite top cells, either through optimizing energy alignment (see

Sections 4.3 and 4.4) and/or suppressing halide segregation. In general, the nonradiative losses for these bandgap analogs are still very high compared to the best single-junction compositions with band gaps  $\approx 1.5$  eV. Thus further understanding of the interface recombination is necessary and PL methods have been shown to be powerful here (see Section 4.5).

The experimental FFs are below empirical predictions at 84% and 82% for perovskite/silicon and perovskite/CIGS tandems, respectively. Interestingly, the highest FF is measured with all-perovskite tandem solar cells. This is rather surprising and cannot be ascribed to smaller device sizes as the FF of 82% is also certified on  $>1\text{ cm}^2$  area for all-perovskite tandems (see also Table 1). However, this  $1\text{ cm}^2$  device has a much lower  $J_{SC}$ , which could stem from the higher conductivity and therefore absorptivity of the front TCO and/or mismatched sub-cells potentially boosting the FF.<sup>[68]</sup> Thus, for a fair FF comparison of all three tandem technologies for  $1\text{ cm}^2$  devices more data for perovskite/CIGS but especially for all-perovskite tandems is needed. Overall, the FF of perovskite/silicon and perovskite/CIGS might be improved by deeper understanding of the electric and electronic properties of the recombination contact and the respective field drop across the interconnection layers (see section Electrical Simulation).

Comparing the PCE values, we interestingly find that the best all-perovskite tandem cell has a better bandgap combination than the other tandems and thus the DBL limit is higher for this technology. However, it is still lower than the 1.1/1.72 eV bandgap combination in the DBL limit (dashed line). Very importantly, we estimate empirical limits for all different tandem combinations that are 34.3%, 31.8%, and 33.6% for silicon, CIGS and all-perovskite tandems, respectively. These values are comparable or slightly higher as previous reports.<sup>[69,70,92,129]</sup> When a lower bandgap CIGS bottom cell will be applied as in the current best single-junction record, the empirical value of the perovskite/CIGS tandem will also rise toward 34% similarly as the other ones.

To summarize, in this review, we analyzed the current status of the perovskite-based tandem solar cell and their main scientific challenges. For the latter, we presented and discussed advanced optical, structural, electrical, radiative, and electronic characterization techniques as well as optical and electrical simulations, enabling to understand the current drawbacks and how to overcome them. Using an empirical approach, we estimate that all three technologies analyzed here, perovskite/silicon, perovskite/CIGS, and perovskite/perovskite, have a similar PCE potential of around 34%. The main limitation in current record tandem devices following the comparison with our empirical limits are moderate  $V_{OC}$ s and FFs for all three as well as the low  $J_{SC}$  for all-perovskite tandems. The main challenge is ensuring the high  $V_{OC}$  of the perovskite top cell through optimization of the perovskite itself with reduced interface recombination of the high bandgap perovskite top cell together with favorable energy alignment of the contact layers. This should also help improving the FF. In addition, the  $J_{SC}$  of low bandgap perovskite bottom cells for all-perovskite tandem devices needs to be enhanced for a better optical understanding of these cells. As the empirical values presented herein are based on reasonable assumptions, we believe it is very likely that these predicted PCEs of 34% will be reached within the next years for all the three different tandem technologies.

## Acknowledgements

The authors thank Amran Al-Ashouri, Max Grischek, Eike Köhnen, Marcel Roß, Philipp Tockhorn, and Fengjiu Yang for proof reading and fruitful discussions. Funding was provided by the Federal Ministry of Education and Research (BMBF) for funding of the Young Investigator Group Perovskite Tandem Solar Cells within the program "Materialforschung fuer die Energiewende" (grant no. 03SF0540) Further funding was provided by the German Federal Ministry for Economic Affairs and Energy (BMWi) through the "PersiST" project (grant no. 0324037C) and by the Helmholtz Association within the framework of HySPRINT Innovation lab and the future project PEROSEED. In addition the German Science Foundation (DFG) is acknowledged within the SPP 2196 "Perovskite semiconductors: From fundamental properties to devices".

## Conflict of Interest

The authors declare no conflict of interest.

## Keywords

all-perovskite, monolithic perovskites, perovskite/CIGS, perovskite/silicon, perovskite solar cells, tandem solar cells

Received: December 13, 2019

Revised: March 5, 2020

Published online: May 4, 2020

- [1] "Renewable Sources Contribute More Than 40 Percent to Germany's Public Net Electricity Generation in 2018 – Fraunhofer ISE," *Fraunhofer Institute for Solar Energy Systems ISE*. [Online]. Available: <https://www.ise.fraunhofer.de/en/press-media/news/2019/renewable-sources-contribute-more-than-40-percent-to-germanys-public-net-electricity-generation-in-2018.html>, (accessed: December 2019).
- [2] IEA, "IEA World Energy Outlook 2019," *IEA*. [Online]. Available: <https://www.iea.org/reports/world-energy-outlook-2019>, (accessed: December 2019).
- [3] Z. Li, Y. Zhao, X. Wang, Y. Sun, Z. Zhao, Y. Li, H. Zhou, Q. Chen, *Joule* **2018**, 2, 1559.
- [4] Z. J. Yu, J. V. Carpenter, Z. C. Holman, *Nat. Energy* **2018**, 3, 747.
- [5] R. Jones-Albertus, D. Feldman, R. Fu, K. Horowitz, M. Woodhouse, *Prog. Photovolt. Res. Appl.* **2016**, 24, 1272.
- [6] Study: Current and Future Cost of Photovoltaics – *Fraunhofer ISE, Fraunhofer Institute for Solar Energy Systems ISE*. [Online]. Available: <https://www.ise.fraunhofer.de/en/publications/studies/studie-current-and-future-cost-of-photovoltaics-long-term-scenarios-for-market-development-system-prices-and-lcoe-of-utility-scale-pv-systems.html>, (accessed: December 2019).
- [7] C. Case, N. Beaumont, D. Kirk, *ACS Energy Lett.* **2019**, 4, 2760.
- [8] J. Werner, B. Niesen, C. Ballif, *Adv. Mater. Interfaces* **2017**, 5, 1700731.
- [9] A. K. Jena, A. Kulkarni, T. Miyasaka, *Chem. Rev.* **2019**, 119, 3036.
- [10] M. A. Green, A. Ho-Baillie, H. J. Snaith, *Nat. Photonics* **2014**, 8, 506.
- [11] H.-S. Kim, A. Hagfeldt, N.-G. Park, *Chem. Commun.* **2019**, 55, 1192.
- [12] "Web of Science search for 'perovskite solar cells' in the title."
- [13] OxfordPV press release: Perovskite world record, 20-Dec-2018. [Online]. Available: <https://www.oxfordpv.com/news/oxford-pv-perovskite-solar-cell-achieves-28-efficiency>, (accessed: November 2019).
- [14] A. Al-Ashouri, A. Magomedov, M. Roß, M. Jošt, M. Talaikis, G. Chistiakova, T. Bertram, J. A. Márquez, E. Köhnen, E. Kasparavičius, S. Levchenko, L. Gil-Escríg, C. J. Hages, R. Schlatmann, B. Rech, T. Malinauskas, T. Unold, C. A. Kaufmann, L. Korte, G. Niaura, V. Getautis, S. Albrecht, *Energy Environ. Sci.* **2019**, 12, 3356.
- [15] R. Lin, K. Xiao, Z. Qin, Q. Han, C. Zhang, M. Wei, M. I. Saidaminov, Y. Gao, J. Xu, M. Xiao, A. Li, J. Zhu, E. H. Sargent, H. Tan, *Nat. Energy* **2019**, 4, 864.
- [16] M. Saliba, T. Matsui, J.-Y. Seo, K. Domanski, J.-P. Correa-Baena, M. K. Nazeeruddin, S. M. Zakeeruddin, W. Tress, A. Abate, A. Hagfeldt, M. Grätzel, *Energy Environ. Sci.* **2016**, 9, 1989.
- [17] S. De Wolf, J. Holovsky, S.-J. Moon, P. Löper, B. Niesen, M. Ledinsky, F.-J. Haug, J.-H. Yum, C. Ballif, *J. Phys. Chem. Lett.* **2014**, 5, 1035.
- [18] J. Tong, Z. Song, D. H. Kim, X. Chen, C. Chen, A. F. Palmstrom, P. F. Ndione, M. O. Reese, S. P. Dunfield, O. G. Reid, J. Liu, F. Zhang, S. P. Harvey, Z. Li, S. T. Christensen, G. Teeter, D. Zhao, M. M. Al-Jassim, M. F. A. M. van Hest, M. C. Beard, S. E. Shaheen, J. J. Berry, Y. Yan, K. Zhu, *Science* **2019**, 364, 475.
- [19] Y. Chen, H. T. Yi, X. Wu, R. Haroldson, Y. N. Gartstein, Y. I. Rodionov, K. S. Tikhonov, A. Zakhidov, X.-Y. Zhu, V. Podzorov, *Nat. Commun.* **2016**, 7, 1.
- [20] Z. Chen, Q. Dong, Y. Liu, C. Bao, Y. Fang, Y. Lin, S. Tang, Q. Wang, X. Xiao, Y. Bai, Y. Deng, J. Huang, *Nat. Commun.* **2017**, 8, 1890.

- [21] X. Cheng, L. Jing, Y. Yuan, S. Du, Q. Yao, J. Zhang, J. Ding, T. Zhou, *CrystEngComm* **2019**, *21*, 4085.
- [22] P. Schulz, D. Cahen, A. Kahn, *Chem. Rev.* **2019**, *119*, 3349.
- [23] M. Stolterfoht, P. Caprioglio, C. M. Wolff, J. A. Márquez, J. Nordmann, S. Zhang, D. Rothhardt, U. Hörmann, Y. Amir, A. Redinger, L. Kegelmann, F. Zu, S. Albrecht, N. Koch, T. Kirchartz, M. Saliba, T. Unold, D. Neher, *Energy Environ. Sci.* **2019**, *12*, 2778.
- [24] C. M. Wolff, P. Caprioglio, M. Stolterfoht, D. Neher, *Adv. Mater.* **2019**, *31*, 1902762.
- [25] Y. Liu, S. Akin, L. Pan, R. Uchida, N. Arora, J. V. Milić, A. Hinderhofer, F. Schreiber, A. R. Uhl, S. M. Zakeeruddin, A. Hagfeldt, M. I. Dar, M. Grätzel, *Sci. Adv.* **2019**, *5*, eaaw2543.
- [26] M. Kim, G.-H. Kim, T. K. Lee, I. W. Choi, H. W. Choi, Y. Jo, Y. J. Yoon, J. W. Kim, J. Lee, D. Huh, H. Lee, S. K. Kwak, J. Y. Kim, D. S. Kim, *Joule* **2019**, *3*, 2179.
- [27] Q. Jiang, Y. Zhao, X. Zhang, X. Yang, Y. Chen, Z. Chu, Q. Ye, X. Li, Z. Yin, J. You, *Nat. Photonics* **2019**, *13*, 460.
- [28] E. H. Jung, N. J. Jeon, E. Y. Park, C. S. Moon, T. J. Shin, T.-Y. Yang, J. H. Noh, J. Seo, *Nature* **2019**, *567*, 511.
- [29] J. J. Yoo, S. Wieghold, M. C. Sponseller, M. R. Chua, S. N. Bertram, N. T. P. Hartono, J. S. Tresback, E. C. Hansen, J.-P. Correa-Baena, V. Bulović, T. Buonassisi, S. S. Shin, M. G. Bawendi, *Energy Environ. Sci.* **2019**, *12*, 2192.
- [30] H. Min, M. Kim, S.-U. Lee, H. Kim, G. Kim, K. Choi, J. H. Lee, S. I. Seok, *Science* **2019**, *366*, 749.
- [31] N. J. Jeon, J. H. Noh, Y. C. Kim, W. S. Yang, S. Ryu, S. I. Seok, *Nat. Mater.* **2014**, *13*, 897.
- [32] T. Abzieher, S. Moghadamzadeh, F. Schackmar, H. Eggers, F. Sutterlüti, A. Farooq, D. Kojda, K. Habicht, R. Schmager, A. Mertens, R. Azmi, L. Klohr, J. A. Schwenzer, M. Hetterich, U. Lemmer, B. S. Richards, M. Powalla, U. W. Paetzold, *Adv. Energy Mater.* **2019**, *9*, 1802995.
- [33] F. Mathies, H. Eggers, B. S. Richards, G. Hernandez-Sosa, U. Lemmer, U. W. Paetzold, *ACS Appl. Energy Mater.* **2018**, *1*, 1834.
- [34] J. Ávila, C. Momblona, P. Boix, M. Sessolo, M. Anaya, G. Lozano, K. Vandewal, H. Míguez, H. J. Bolink, *Energy Environ. Sci.* **2018**, *11*, 3292.
- [35] C. Momblona, L<sup>3</sup>n Gil-Escríg, E. Bandiello, E. M. Hutter, M. Sessolo, K. Lederer, J. Blochwitz-Nimoth, H. J. Bolink, *Energy Environ. Sci.* **2016**, *9*, 3456.
- [36] J. Borchert, R. L. Milot, J. B. Patel, C. L. Davies, A. D. Wright, L. Martínez Maestro, H. J. Snaith, L. M. Herz, M. B. Johnston, *ACS Energy Lett.* **2017**, *2*, 2799.
- [37] S. Rafizadeh, K. Wienands, L. E. Mundt, A. J. Bett, P. S. C. Schulze, L. C. Andreani, M. Hermle, S. W. Glunz, J. C. Goldschmidt, *IEEE J. Photovolt.* **2019**, *1*.
- [38] F. Sahli, J. Werner, B. A. Kamino, M. Bräuninger, R. Monnard, B. Paviet-Salomon, L. Barraud, L. Ding, J. J. Diaz Leon, D. Sacchetto, G. Cattaneo, M. Despeisse, M. Boccard, S. Nicolay, Q. Jeangros, B. Niesen, C. Ballif, *Nat. Mater.* **2018**, *17*, 820.
- [39] R. Swartwout, M. T. Hoerantner, V. Bulović, *ENERGY Environ. Mater.* **2019**, *2*, 119.
- [40] P. A. Basore, in *2016 IEEE 43rd Photovoltaic Specialists Conference (PVSC)*, **2016**, pp. 2635–2637.
- [41] S. Albrecht, B. Rech, *Nat. Energy* **2017**, *2*, 16196.
- [42] A. Martí, G. L. Araújo, *Sol. Energy Mater. Sol. Cells* **1996**, *43*, 203.
- [43] A. De Vos, *J. Phys. Appl. Phys.* **1980**, *13*, 839.
- [44] J. Werner, F. Sahli, F. Fu, J. J. Diaz Leon, A. Walter, B. A. Kamino, B. Niesen, S. Nicolay, Q. Jeangros, C. Ballif, *ACS Energy Lett.* **2018**, *3*, 2052.
- [45] D. P. McMeekin, S. Mahesh, N. K. Noel, M. T. Klug, J. Lim, J. H. Warby, J. M. Ball, L. M. Herz, M. B. Johnston, H. J. Snaith, *Joule* **2019**, *3*, 387.
- [46] W. Shockley, H. J. Queisser, *J. Appl. Phys.* **1961**, *32*, 510.
- [47] S. S. Hegedus, F. Kampas, J. Xi, *Appl. Phys. Lett.* **1995**, *67*, 813.
- [48] N. Pellaton Vaucher, B. Rech, D. Fischer, S. Dubail, M. Goetz, H. Keppner, N. Wyrsch, C. Beneking, O. Hadjadj, V. Shklover, A. Shah, *Sol. Energy Mater. Sol. Cells* **1997**, *49*, 27.
- [49] J. Rath, *Sol. Energy Mater. Sol. Cells* **1998**, *53*, 189.
- [50] I. A. Yunaz, A. Yamada, M. Konagai, *Jpn. J. Appl. Phys.* **2007**, *46*, L1152.
- [51] S. Roland, S. Neubert, S. Albrecht, B. Stannowski, M. Seger, A. Facchetti, R. Schlatmann, B. Rech, D. Neher, *Adv. Mater.* **2015**, *27*, 1262.
- [52] S. Essig, C. Allebé, T. Remo, J. F. Geisz, M. A. Steiner, K. Horowitz, L. Barraud, J. S. Ward, M. Schnabel, A. Descoedres, D. L. Young, M. Woodhouse, M. Despeisse, C. Ballif, A. Tamboli, *Nat. Energy* **2017**, *2*, 1.
- [53] J. Gilot, M. M. Wienk, R. C. A. J. Janssen, *Adv. Funct. Mater.* **2010**, *20*, 3904.
- [54] L. Meng, Y. Zhang, X. Wan, C. Li, X. Zhang, Y. Wang, X. Ke, Z. Xiao, L. Ding, R. Xia, H.-L. Yip, Y. Cao, Y. Chen, *Science* **2018**, *361*, 1094.
- [55] K. A. Bush, A. F. Palmstrom, Z. J. Yu, M. Boccard, R. Cheacharoen, J. P. Mailoa, D. P. McMeekin, R. L. Z. Hoye, C. D. Bailie, T. Leijtens, I. M. Peters, M. C. Minichetti, N. Rolston, R. Prasanna, S. Sofia, D. Harwood, W. Ma, F. Moghadam, H. J. Snaith, T. Buonassisi, Z. C. Holman, S. F. Bent, M. D. McGehee, *Nat. Energy* **2017**, *2*, 17009.
- [56] A. F. Palmstrom, G. E. Eperon, T. Leijtens, R. Prasanna, S. N. Haberl, W. Nemeth, E. A. Gaulding, S. P. Dunfield, M. Reese, S. Nanayakkara, T. Moot, J. Werner, J. Liu, B. To, S. T. Christensen, M. D. McGehee, M. F. A. M. van Hest, J. M. Luther, J. J. Berry, D. T. Moore, *Joule* **2019**, *3*, 2193.
- [57] J. A. Raiford, R. A. Belisle, K. A. Bush, R. Prasanna, A. F. Palmstrom, M. D. McGehee, S. F. Bent, *Sustain. Energy Fuels* **2019**, *3*, 1517.
- [58] T. Leijtens, K. A. Bush, R. Prasanna, M. D. McGehee, *Nat. Energy* **2018**, *3*, 828.
- [59] S. De Wolf, M. Kondo, *J. Appl. Phys.* **2009**, *105*, 103707.
- [60] S. Albrecht, M. Saliba, J. P. Correa Baena, F. Lang, L. Kegelmann, M. Mews, L. Steier, A. Abate, J. Rappich, L. Korte, R. Schlatmann, M. K. Nazeeruddin, A. Hagfeldt, M. Grätzel, B. Rech, *Energy Env. Sci* **2016**, *9*, 81.
- [61] J. Gilot, M. M. Wienk, R. C. A. J. Janssen, *Appl. Phys. Lett.* **2007**, *90*, 143512.
- [62] M. Jošt, T. Bertram, D. Koushik, J. A. Marquez, M. A. Verheijen, M. D. Heinemann, E. Könen, A. Al-Ashouri, S. Braunger, F. Lang, B. Rech, T. Unold, M. Creatore, I. Lauermann, C. A. Kaufmann, R. Schlatmann, S. Albrecht, *ACS Energy Lett.* **2019**, *4*, 583.
- [63] Q. Han, Y.-T. Hsieh, L. Meng, J.-L. Wu, P. Sun, E.-P. Yao, S.-Y. Chang, S.-H. Bae, T. Kato, V. Bermudez, Y. Yang, *Science* **2018**, *361*, 904.
- [64] D. Chen, P. Manley, P. Tockhorn, D. Eisenhauer, G. Köppel, M. Hammerschmidt, S. Burger, S. Albrecht, C. Becker, K. Jäger, *J. Photonics Energy* **8**, p. 022601.
- [65] A. Y. Alsalloum, B. Turedi, X. Zheng, S. Mitra, A. A. Zhumekenov, K. J. Lee, P. Maity, I. Gereige, A. AlSaggaf, I. S. Roqan, O. F. Mohammed, O. M. Bakr, *ACS Energy Lett.* **2020**, *5*, 657.
- [66] H. Eggers, F. Schackmar, T. Abzieher, Q. Sun, U. Lemmer, Y. Vaynzof, B. S. Richards, G. Hernandez-Sosa, U. W. Paetzold, *Adv. Energy Mater.* **2020**, *10*, 1903184.
- [67] B. Chen, Z. J. Yu, S. Manzoor, S. Wang, W. Weigand, Z. Yu, G. Yang, Z. Ni, X. Dai, Z. C. Holman, J. Huang, *Joule* **2020**, <https://doi.org/10.1016/j.joule.2020.01.008>.
- [68] E. Könen, M. Jošt, A. B. Morales-Vilches, P. Tockhorn, A. Al-Ashouri, B. Macco, L. Kegelmann, L. Korte, B. Rech, R. Schlatmann, B. Stannowski, S. Albrecht, *Sustain. Energy Fuels* **2019**, *3*, 1995.
- [69] K. Jäger, L. Korte, B. Rech, S. Albrecht, *Opt. Express* **2017**, *25*, A473.
- [70] M. T. Hörantner, H. J. Snaith, *Energy Environ. Sci.* **2017**, *10*, 1983.
- [71] M. Saliba, J.-P. Correa-Baena, M. Grätzel, A. Hagfeldt, A. Abate, *Angew. Chem., Int. Ed.* **2017**, *57*, 2554.

- [72] S. Gharibzadeh, B. A. Nejand, M. Jakoby, T. Abzieher, D. Hauschild, S. Moghadamzadeh, J. A. Schwerzer, P. Brenne, R. Schmager, A. A. Haghhighirad, L. Weinhardt, U. Lemmer, B. S. Richards, I. A. Howard, U. W. Paetzold, *Adv. Energy Mater.* **0**, p. 1803699.
- [73] A. Rajagopal, R. J. Stoddard, S. B. Jo, H. W. Hillhouse, A. K.-Y. Jen, *Nano Lett.* **2018**, *18*, 3985.
- [74] E. L. Unger, L. Kegelmann, K. Suchan, D. Sörell, L. Korte, S. Albrecht, *J. Mater. Chem. A* **2017**, *5*, 11401.
- [75] S. Yang, J. Dai, Z. Yu, Y. Shao, Y. Zhou, X. Xiao, X. C. Zeng, J. Huang, *J. Am. Chem. Soc.* **2019**, *141*, 5781.
- [76] D. Zhao, C. Chen, C. Wang, M. M. Junda, Z. Song, C. R. Grice, Y. Yu, C. Li, B. Subedi, N. J. Podraza, X. Zhao, G. Fang, R.-G. Xiong, K. Zhu, Y. Yan, *Nat. Energy* **2018**, *3*, 1093.
- [77] C.-Y. Chang, B.-C. Tsai, Y.-C. Hsiao, M.-Z. Lin, H.-F. Meng, *Nano Energy* **2019**, *55*, 354.
- [78] T. Leijtens, R. Prasanna, K. A. Bush, G. E. Eperon, J. A. Raiford, A. Gold-Parker, E. J. Wolf, S. A. Swifter, C. C. Boyd, H.-P. Wang, M. F. Toney, S. F. Bent, M. D. McGehee, *Sustain. Energy Fuels* **2018**, *2*, 2450.
- [79] R. Prasanna, T. Leijtens, S. P. Dunfield, J. A. Raiford, E. J. Wolf, S. A. Swifter, J. Werner, G. E. Eperon, C. de Paula, A. F. Palmstrom, C. C. Boyd, M. F. A. M. Hest, S. F. Bent, G. Teeter, J. J. Berry, M. D. McGehee, *Nat. Energy* **2019**, *1*.
- [80] Z. Yang, Z. Yu, H. Wei, X. Xiao, Z. Ni, B. Chen, Y. Deng, S. N. Habisreutinger, X. Chen, K. Wang, J. Zhao, P. N. Rudd, J. J. Berry, M. C. Beard, J. Huang, *Nat. Commun.* **2019**, *10*, 1.
- [81] L. Krückemeier, U. Rau, M. Stolterfoht, T. Kirchartz, *Adv. Energy Mater.* **2019**, *10*, 1902573.
- [82] M. Suri, A. Hazarika, B. W. Larson, Q. Zhao, M. Vallés-Pelarda, T. D. Siegler, M. K. Abney, A. J. Ferguson, B. A. Korgel, J. M. Luther, *ACS Energy Lett.* **2019**, *4*, 1954.
- [83] B. Chen, X. Zheng, Y. Bai, N. P. Padture, J. Huang, *Adv. Energy Mater.* **2017**, *7*, 1602400.
- [84] G. E. Eperon, M. T. Hörantner, H. J. Snaith, *Nat. Rev. Chem.* **2017**, *1*, 95.
- [85] Q. Tai, K.-C. Tang, F. Yan, *Energy Environ. Sci.* **2019**, *12*, 2375.
- [86] N. Torabi, A. Behjat, Y. Zhou, P. Docampo, R. J. Stoddard, H. W. Hillhouse, T. Ameri, *Mater. Today Energy* **2019**, *12*, 70.
- [87] Z. Song, C. Chen, C. Li, R. A. Awni, D. Zhao, Y. Yan, *Semicond Sci Technol* **2019**, *34*, 093001.
- [88] Y. Hu, L. Song, Y. Chen, W. Huang, *Sol. RRL* **2019**, *3*, 1900080.
- [89] C. Wang, Z. Song, C. Li, D. Zhao, Y. Yan, *Adv. Funct. Mater.* **2019**, *29*, 1808801.
- [90] K. A. Bush, S. Manzoor, K. Frohma, Z. J. Yu, J. A. Raiford, A. F. Palmstrom, H.-P. Wang, R. Prasanna, S. F. Bent, Z. C. Holman, M. D. McGehee, *ACS Energy Lett.* **2018**, *3*, 2173.
- [91] B. Chen, Z. Yu, K. Liu, X. Zheng, Y. Liu, J. Shi, D. Spronk, P. N. Rudd, Z. Holman, J. Huang, *Joule* **2019**, *3*, 177.
- [92] M. Jošt, E. Köhnen, A. B. Morales-Vilches, B. Lipovšek, K. Jäger, B. Macco, A. Al-Ashouri, J. Krč, L. Korte, B. Rech, R. Schlatmann, M. Topič, B. Stannowski, S. Albrecht, *Energy Environ. Sci.* **2018**, *11*, 3511.
- [93] L. Mazzarella, Y.-H. Lin, S. Kirner, A. B. Morales-Vilches, L. Korte, S. Albrecht, E. Crossland, B. Stannowski, C. Case, H. J. Snaith, R. Schlatmann, *Adv. Energy Mater.* **2019**, *9*, 1803241.
- [94] G. Nogay, F. Sahli, J. Werner, R. Monnard, M. Boccard, M. Despeisse, F.-J. Haug, Q. Jeangros, A. Ingenito, C. Ballif, *ACS Energy Lett.* **2019**, *4*, 844.
- [95] M. A. Green, E. D. Dunlop, D. H. Levi, J. Hohl-Ebinger, M. Yoshita, A. W. Y. Ho-Baillie, *Prog. Photovolt. Res. Appl.* **2019**, *27*, 565.
- [96] Best Research-Cell Efficiency Chart. [Online]. Available: <https://www.nrel.gov/pv/cell-efficiency.html>, (accessed: March 2020).
- [97] M. A. Green, Y. Hisikawa, E. D. Dunlop, D. H. Levi, J. Hohl-Ebinger, A. W. Y. Ho-Baillie, *Prog. Photovolt. Res. Appl.* **2018**, *26*, 3.
- [98] Fraunhofer Institute for Solar Energy Systems, ISE, Photovoltaics report, **2019**.
- [99] LONGi Solar sets new bifacial mono-PERC solar cell world record at 24.06 percent. [Online]. Available: <https://www.prnewswire.com/news-releases/longi-solar-sets-new-bifacial-mono-perc-solar-cell-world-record-at-24-06-percent-300779413.html>, (accessed: November 2019).
- [100] J. P. Mailoa, C. D. Bailie, E. C. Johlin, E. T. Hoke, A. J. Akey, W. H. Nguyen, M. D. McGehee, T. Buonassisi, *Appl. Phys. Lett.* **2015**, *106*, 121105.
- [101] K. Yoshikawa, W. Yoshida, T. Irie, H. Kawasaki, K. Konishi, H. Ishibashi, T. Asatani, D. Adachi, M. Kanematsu, H. Uzu, K. Yamamoto, *Sol. Energy Mater. Sol. Cells* **2017**, *173*, 37.
- [102] A. Richter, J. Benick, F. Feldmann, A. Fell, M. Hermle, S. W. Glunz, *Sol. Energy Mater. Sol. Cells* **2017**, *173*, 96.
- [103] M. Richter, P. Saint-Cast, T. Dannenberg, M. Zimmer, J. Rentsch, *Energy Procedia* **2015**, *77*, 832.
- [104] R. Brendel, C. Kranz, S. Wyczanowski, S. Dorn, K. Weise, C. Klein, K. Bothe, T. Dullweber, *Proc 27th Eur. Photovolt. Sol. Energy Conf. Exhib.* **2012**, pp. 557–560.
- [105] A. Descoeudres, J. Horzel, B. Paviet-Salomon, L. L. Senaud, G. Christmann, J. Geissbühler, P. Wyss, N. Badel, J.-W. Schüttauf, J. Zhao, C. Allebé, A. Faes, S. Nicolay, C. Ballif, M. Despeisse, *Prog. Photovolt. Res. Appl.* **2019**, <https://doi.org/10.1002/pip.3227>.
- [106] FinanzNachrichten.de. [Online]. Available: <https://www.finanznachrichten.de/nachrichten-2019-05/46816494-trina-solar-announces-new-efficiency-record-of-24-58-efficiency-for-monocrystalline-silicon-i-topcon-cell-008.htm>, (accessed: November 2019).
- [107] E. Yablonovitch, T. Gmitter, R. M. Swanson, Y. H. Kwark, *Appl. Phys. Lett.* **1985**, *47*, 1211.
- [108] R. Peibst, Y. Larionova, S. Reiter, T. F. Wietler, N. Orlowski, S. Schäfer, B. Min, M. Stratmann, D. Tetzlaff, J. Krügener, U. Höhne, J.-D. Kähler, H. Mehlich, S. Frigge, R. Brendel, *IEEE J. Photovolt.* **2018**, *8*, 719.
- [109] J. Werner, A. Walter, E. Rucavado, S.-J. Moon, D. Sacchetto, M. Rienaecker, R. Peibst, R. Brendel, X. Niquille, S. De Wolf, P. Löper, M. Morales-Masis, S. Nicolay, B. Niesen, C. Ballif, *Appl. Phys. Lett.* **2016**, *109*, 233902.
- [110] Y. Wu, D. Yan, J. Peng, T. Duong, Y. Wan, S. P. Phang, H. Shen, N. Wu, C. Barugkin, X. Fu, S. Surve, D. Grant, D. Walter, T. P. White, K. R. Catchpole, K. J. Weber, *Energy Environ. Sci.* **2017**, *10*, 2472.
- [111] J. Zheng, C. F. J. Lau, H. Mehrvarz, F.-J. Ma, Y. Jiang, X. Deng, A. Soeriadi, J. Kim, M. Zhang, L. Hu, X. Cui, D. S. Lee, J. Bing, Y. Cho, C. Chen, M. A. Green, S. Huang, A. W. Y. Ho-Baillie, *Energy Env. Sci* **2018**, *11*, 2432.
- [112] J. Zheng, H. Mehrvarz, F.-J. Ma, C. F. J. Lau, M. A. Green, S. Huang, A. W. Y. Ho-Baillie, *ACS Energy Lett.* **2018**, *3*, 2299.
- [113] H. Shen, S. T. Omelchenko, D. A. Jacobs, S. Yalamanchili, Y. Wan, D. Yan, P. Phang, T. Duong, Y. Wu, Y. Yin, C. Samundsett, J. Peng, N. Wu, T. P. White, G. G. Andersson, N. S. Lewis, K. R. Catchpole, *Sci. Adv.* **2018**, *4*, eaau9711.
- [114] J. Zheng, H. Mehrvarz, C. Liao, J. Bing, X. Cui, Y. Li, V. R. Gonçales, C. F. J. Lau, D. S. Lee, Y. Li, M. Zhang, J. Kim, Y. Cho, L. G. Caro, S. Tang, C. Chen, S. Huang, A. W. Y. Ho-Baillie, *SSRN Electron. J.* **2019**, 2623.
- [115] P. Löper, S.-J. Moon, S. L. Martín de Nicolas, B. Niesen, M. Ledinsky, S. Nicolay, J. Bailat, J.-H. Yum, S. De Wolf, C. Ballif, *Phys. Chem. Chem. Phys.* **2015**, *17*, 1619.
- [116] J. Werner, C.-H. Weng, A. Walter, L. Fesquet, J. P. Seif, S. De Wolf, B. Niesen, C. Ballif, *J. Phys. Chem. Lett.* **2016**, *7*, 161.
- [117] S. Albrecht, M. Saliba, J. P. Correa Baena, F. Lang, L. Kegelmann, M. Mews, L. Steier, A. Abate, J. Rappich, L. Korte, R. Schlatmann, M. K. Nazeeruddin, A. Hagfeldt, M. Grätzel, B. Rech, *Energy Environ. Sci.* **2016**, *9*, 81.

- [118] F. T. Si, D. Y. Kim, R. Santbergen, H. Tan, R. A. C. M. M. Swaaij, A. H. M. Smets, O. Isabella, M. Zeman, *Appl. Phys. Lett.* **2014**, *105*, 063902.
- [119] H. Sai, T. Matsui, T. Koida, K. Matsubara, M. Kondo, S. Sugiyama, H. Katayama, Y. Takeuchi, I. Yoshida, *Appl. Phys. Lett.* **2015**, *106*, 213902.
- [120] H.-Z. B. für M. und Energie, HZB Website. [Online]. Available: [https://www.helmholtz-berlin.de/pubbis/news\\_seite?nid=21020;sprache=en;seitenid=1](https://www.helmholtz-berlin.de/pubbis/news_seite?nid=21020;sprache=en;seitenid=1), (accessed: March 2020).
- [121] B. A. Kamino, B. Paviet-Salomon, S.-J. Moon, N. Badel, J. Levrat, G. Christmann, A. Walter, A. Faes, L. Ding, J. J. Diaz Leon, A. Paracchino, M. Despeisse, C. Ballif, S. Nicolay, *ACS Appl. Energy Mater.* **2019**, *2*, 3815.
- [122] J. Kegel, H. Angermann, U. Stürzebecher, E. Conrad, M. Mews, L. Korte, B. Stegemann, *Appl. Surf. Sci.* **2014**, *301*, 56.
- [123] *Handbook of Silicon Wafer Cleaning Technology*, Elsevier, Amsterdam, Netherlands **2018**.
- [124] J. Werner, G. Nogay, F. Sahli, T. C.-J. Yang, M. Bräuninger, G. Christmann, A. Walter, B. A. Kamino, P. Fiala, P. Löper, S. Nicolay, Q. Jeangros, B. Niesen, C. Ballif, *ACS Energy Lett.* **2018**, *3*, 742.
- [125] M. Jošt, S. Albrecht, B. Lipovšek, J. Krč, L. Korte, B. Rech, M. Topič, *Energy Procedia* **2016**, *102*, 43.
- [126] R. Santbergen, R. Mishima, T. Meguro, M. Hino, H. Uzu, J. Blanker, K. Yamamoto, M. Zeman, *Opt. Express* **2016**, *24*, A1288.
- [127] J. Werner, L. Barraud, A. Walter, M. Bräuninger, F. Sahli, D. Sacchetto, N. Tétreault, B. Paviet-Salomon, S.-J. Moon, C. Allebé, M. Despeisse, S. Nicolay, S. De Wolf, B. Niesen, C. Ballif, *ACS Energy Lett.* **2016**, *1*, 474.
- [128] M. A. Contreras, L. M. Mansfield, B. Egaas, J. Li, M. Romero, R. Noufi, E. Rudiger-Voigt, W. Mannstadt, *Prog. Photovolt. Res. Appl.* **2012**, *20*, 843.
- [129] J. Lehr, M. Langenhorst, R. Schmager, S. Kirner, U. Lemmer, B. S. Richards, C. Case, U. W. Paetzold, *Sustain. Energy Fuels* **2018**, *2*, 2754.
- [130] M. Langenhorst, B. Sautter, R. Schmager, J. Lehr, E. Ahlsweide, M. Powalla, U. Lemmer, B. S. Richards, U. W. Paetzold, *Prog. Photovolt. Res. Appl.* **2019**, *290*, 27.
- [131] J. Eisenlohr, B. G. Lee, J. Benick, F. Feldmann, M. Driessens, N. Milenkovic, B. Bläsi, J. C. Goldschmidt, M. Hermle, *Sol. Energy Mater. Sol. Cells* **2015**, *142*, 60.
- [132] A. Jasenek, U. Rau, K. Weinert, H. W. Schock, J. H. Werner, in *Proceedings of 3rd World Conference on Photovoltaic Energy Conversion*, 2003 **2003**, *1*, pp. 593–598.
- [133] F. Lang, M. Jošt, J. Bundesmann, A. Denker, S. Albrecht, G. Landi, H.-C. Neitzert, J. Rappich, N. H. Nickel, *Energy Environ. Sci.* **2019**, *12*, 1634.
- [134] S. Kijima, T. Nakada, *Appl. Phys. Express* **2008**, *1*, 075002.
- [135] Z. Jehl, M. Bouttemy, D. Lincot, J. F. Guillemoles, I. Gerard, A. Etcheberry, G. Voorwinden, M. Powalla, N. Naghavi, *J. Appl. Phys.* **2012**, *111*, 114509.
- [136] M. D. Heinemann, R. Mainz, F. Ä-sterle, H. Rodriguez-Alvarez, D. Greiner, C. A. Kaufmann, T. Unold, *Sci. Rep.* **2017**, *7*, 45463.
- [137] T. Todorov, T. Gershon, O. Gunawan, Y. S. Lee, C. Sturdevant, L.-Y. Chang, S. Guha, *Adv. Energy Mater.* **2015**, *5*, 1500799.
- [138] L. Meng, J. You, T.-F. Guo, Y. Yang, *Acc. Chem. Res.* **2016**, *49*, 155.
- [139] Y. H. Jang, J. M. Lee, J. W. Seo, I. Kim, D.-K. Lee, *J. Mater. Chem. A* **2017**, *5*, 19439.
- [140] A. R. Uhl, A. Rajagopal, J. A. Clark, A. Murray, T. Feurer, S. Buecheler, A. K.-Y. Jen, H. W. Hillhouse, *Adv. Energy Mater.* **2018**, *8*, 1801254.
- [141] F. Fu, S. Nishiwaki, J. Nishiwaki, T. Feurer, S. Pisoni, Q. Jeangros, S. Buecheler, C. Ballif, A. N. Tiwari, *ArXiv190710330 Cond-Mat Physicsphysics*, **2019**.
- [142] Z. Liu, A. Zhu, F. Cai, L. Tao, Y. Zhou, Z. Zhao, Q. Chen, Y.-B. Cheng, H. Zhou, *J. Mater. Chem. A* **2017**, *5*, 6597.
- [143] Z. Song, C. L. McElvany, A. B. Phillips, I. Celik, P. W. Krantz, S. C. Watthage, G. K. Liyanage, D. Apul, M. J. Heben, *Energy Environ. Sci.* **2017**, *10*, 1297.
- [144] N. L. Chang, A. W. Yi Ho-Baillie, P. A. Basore, T. L. Young, R. Evans, R. J. Egan, *Prog. Photovolt. Res. Appl.* **2017**, *25*, 390.
- [145] D. Forgács, L. Gil-Escríg, D. Pérez-Del-Rey, C. Momblona, J. Werner, B. Niesen, C. Ballif, M. Sessolo, H. J. Bolink, *Adv. Energy Mater.* **2018**, *7*, 1602121.
- [146] F. Jiang, T. Liu, B. Luo, J. Tong, F. Qin, S. Xiong, Z. Li, Y. Zhou, *J. Mater. Chem. A* **2016**, *4*, 1208.
- [147] G. E. Eperon, T. Leijtens, K. A. Bush, R. Prasanna, T. Green, J. T.-W. Wang, D. P. McMeekin, G. Volonakis, R. L. Milot, R. May, A. Palmstrom, D. J. Slotcavage, R. A. Belisle, J. B. Patel, E. S. Parrott, R. J. Sutton, W. Ma, F. Moghadam, B. Conings, A. Babayigit, H.-G. Boyen, S. Bent, F. Giustino, L. M. Herz, M. B. Johnston, M. D. McGehee, H. J. Snaith, *Science* **2016**, *354*, 861.
- [148] A. Rajagopal, Z. Yang, S. B. Jo, I. L. Braly, P.-W. Liang, H. W. Hillhouse, A. K.-Y. Jen, *Adv. Mater.* **2017**, *29*, 1702140.
- [149] J. H. Heo, S. H. Im, *Adv. Mater.* **2015**, *28*, 5121.
- [150] A. J. Bett, K. M. Winkler, M. Bivour, L. Cojocaru, Ö. Ş. Kabaklı, P. S. C. Schulze, G. Siefer, L. Tutsch, M. Hermle, S. W. Glunz, J. C. Goldschmidt, *ACS Appl. Mater. Interfaces* **2019**, *11*, 45796.
- [151] H. Back, G. Kim, J. Kim, J. Kong, T. K. Kim, H. Kang, H. Kim, J. Lee, S. Lee, K. Lee, *Energy Environ. Sci.* **2016**, *9*, 1258.
- [152] Y. Kato, L. K. Ono, M. V. Lee, S. Wang, S. R. Raga, Y. Qi, *Adv. Mater. Interfaces* **2015**, *2*, 1500195.
- [153] K. Domanski, J.-P. Correa-Baena, N. Mine, M. K. Nazeeruddin, A. Abate, M. Saliba, W. Tress, A. Hagfeldt, M. Grätzel, *ACS Nano* **2016**, *10*, 6306.
- [154] W. Ming, D. Yang, T. Li, L. Zhang, M.-H. Du, *Adv. Sci.* **2018**, *5*, 1700662.
- [155] W. Chen, H. Sun, Q. Hu, A. B. Djurić, T. P. Russell, X. Guo, Z. He, *ACS Energy Lett.* **2019**, *4*, 2535.
- [156] A. Rajagopal, R. J. Stoddard, H. W. Hillhouse, A. K.-Y. Jen, *J. Mater. Chem. A* **2019**, *7*, 16285.
- [157] R. Prasanna, A. Gold-Parker, T. Leijtens, B. Conings, A. Babayigit, H.-G. Boyen, M. F. Toney, M. D. McGehee, *J. Am. Chem. Soc.* **2017**, *139*, 11117.
- [158] F. Hao, C. C. Stoumpos, R. P. H. Chang, M. G. Kanatzidis, *J. Am. Chem. Soc.* **2014**, *136*, 8094.
- [159] Y. Wang, D. Qian, Y. Cui, H. Zhang, J. Hou, K. Vandewal, T. Kirchartz, F. Gao, *Adv. Energy Mater.* **2018**, *8*, 1801352.
- [160] A. V. Cohen, D. A. Egger, A. M. Rappe, L. Kronik, *ArXiv181004462 Cond-Mat* **2019**.
- [161] I. Levine, O. G. Vera, M. Kulbak, D.-R. Ceratti, C. Rehermann, J. A. Márquez, S. Levchenko, T. Unold, G. Hodes, I. Balberg, D. Cahen, T. Dittrich, *ACS Energy Lett.* **2019**, *4*, 1150.
- [162] C.-C. Chen, S.-H. Bae, W.-H. Chang, Z. Hong, G. Li, Q. Chen, H. Zhou, Y. Yang, *Mater. Horiz.* **2015**, *2*, 203.
- [163] J. Liu, S. Lu, L. Zhu, X. Li, W. C. H. Choy, *Nanoscale* **2016**, *8*, 3638.
- [164] Y. Liu, Z. Hong, Q. Chen, W. Chang, H. Zhou, T.-B. Song, E. Young, Y. (M.) Yang, J. You, G. Li, Y. Yang, *Nano Lett.* **2015**, *15*, 662.
- [165] E. T. Hoke, D. J. Slotcavage, E. R. Dohner, A. R. Bowring, H. I. Karunadasa, M. D. McGehee, *Chem. Sci.* **2014**, *6*, 613.
- [166] L. Reimer, P. W. Hawkes, A. L. Schawlow, K. Shimoda, A. E. Siegman, *Scanning Electron Microscopy: Physics of Image Formation and Microanalysis*, Springer, Berlin/Heidelberg **2013**.
- [167] *Surface Treatment of Materials for Adhesion Bonding – 1st edition* [Online]. Available: <https://www.elsevier.com/books/surface-treatment-of-materials-for-adhesion-bonding/ebnsea-jjad/978-0-8155-1523-4>, (accessed: December 2019).
- [168] R. M. Langford, M. Rogers, *Micron* **2008**, *39*, 1325.
- [169] Y. Yabuuchi, *J. Electron Microsc. (Tokyo)* **2004**, *53*, 471.

- [170] Q. Jeangros, M. Duchamp, J. Werner, M. Kruth, R. E. Durnin-Borkowski, B. Niesen, C. Ballif, A. Hessler-Wyser, *Nano Lett.* **2016**, *16*, 7013.
- [171] B. Conings, J. Drijkoningen, N. Gauquelin, A. Babayigit, J. D'Haen, L. D'Olieslaeger, A. Ethirajan, J. Verbeeck, J. Manca, E. Mosconi, F. De Angelis, H.-G. Boyen, *Adv. Energy Mater.* **2015**, *5*, 1500477.
- [172] F. Matteocci, Y. Busby, J.-J. Pireaux, G. Divitini, S. Cacovich, C. Ducati, A. Di Carlo, *ACS Appl. Mater. Interfaces* **2015**, *7*, 26176.
- [173] J. A. Raiford, C. C. Boyd, A. F. Palmstrom, E. J. Wolf, B. A. Fearon, J. J. Berry, M. D. McGehee, S. F. Bent, *Adv. Energy Mater.* **2019**, *9*, 1902353.
- [174] D. Brabazon, A. Raffer, in *Emerging Nanotechnologies for Manufacturing* (Eds: W. Ahmed, M. J. Jackson), William Andrew Publishing, Boston **2010**, pp. 59–91.
- [175] O. D. Neikov, S. Naboychenko, N. V. Yefimov, *Handbook of Non-Ferrous Metal Powders: Technologies and Applications*, Elsevier, Amsterdam, Netherlands **2018**.
- [176] N. Yantara, F. Yanan, C. Shi, H. A. Dewi, P. P. Boix, S. G. Mhaisalkar, N. Mathews, *Chem. Mater.* **2015**, *27*, 2309.
- [177] M. Abdi-Jalebi, Z. Andaji-Garmaroudi, A. J. Pearson, G. Divitini, S. Cacovich, B. Philippe, H. Rensmo, C. Ducati, R. H. Friend, S. D. Stranks, *ACS Energy Lett.* **2018**, *3*, 2671.
- [178] G. Divitini, S. Cacovich, F. Matteocci, L. CinÃ, A. Di Carlo, C. Ducati, *Nat. Energy* **2016**, *1*, 1.
- [179] D. Rugar, P. Hansma, *Phys. Today* **2008**, *43*, 23.
- [180] H. Shen, T. Duong, J. Peng, D. Jacobs, N. Wu, J. Gong, Y. Wu, S. K. Karuturi, X. Fu, K. Weber, X. Xiao, T. P. White, K. Catchpole, *Energy Environ. Sci.* **2018**, *11*, 394.
- [181] K. I. Schiffmann, *Vak. Forsch. Prax.* **2014**, *26*, 27.
- [182] *Developments in Surface Contamination and Cleaning*, Elsevier, Amsterdam, Netherlands **2012**.
- [183] *Handbook of Analytical Techniques in Concrete Science and Technology – 1st edition [Online]*. Available: <https://www.elsevier.com/books/handbook-of-analytical-techniques-in-concrete-science-and-technology/ramachandran/978-0-8155-1437-4>, (accessed: December 2019).
- [184] G. K. Williamson, W. H. Hall, *Acta Metall.* **1953**, *1*, 22.
- [185] T. Duong, N. Lal, D. Grant, D. Jacobs, P. Zheng, S. Rahman, H. Shen, M. Stocks, A. Blakers, K. Weber, T. P. White, K. R. Catchpole, *IEEE J. Photovoltaics* **2016**, *6*, 679.
- [186] J. Werner, G. Dubuis, A. Walter, P. Löper, S.-J. Moon, S. Nicolay, M. Morales-Masis, S. De Wolf, B. Niesen, C. Ballif, *Sol. Energy Mater. Sol. Cells* **2015**, *141*, 407.
- [187] A. Guchhait, H. A. Dewi, S. W. Leow, H. Wang, G. Han, F. B. Suhami, S. Mhaisalkar, L. H. Wong, N. Mathews, *ACS Energy Lett.* **2017**, *2*, 807.
- [188] D. Zhao, Y. Yu, C. Wang, W. Liao, N. Shrestha, C. R. Grice, A. J. Cimaroli, L. Guan, R. J. Ellingson, K. Zhu, X. Zhao, R.-G. Xiong, Y. Yan, *Nat. Energy* **2017**, *2*, 17018.
- [189] X. Zhao, C. Yao, T. Liu, J. C. Hamill, G. O. Ngongang Ndjawa, G. Cheng, N. Yao, H. Meng, Y.-L. Loo, *Adv. Mater.* **2019**, *31*, 1904494.
- [190] Z. Yang, A. Rajagopal, S. B. Jo, C.-C. Chueh, S. Williams, C.-C. Huang, J. K. Katahara, H. W. Hillhouse, A. K.-Y. Jen, *Nano Lett.* **2016**, *16*, 7739.
- [191] K. Wang, Z. Jin, L. Liang, H. Bian, D. Bai, H. Wang, J. Zhang, Q. Wang, S. Liu, *Nat. Commun.* **2018**, *9*, 1.
- [192] K. A. Bush, C. D. Bailie, Y. Chen, A. R. Bowring, W. Wang, W. Ma, T. Leijtens, F. Moghadam, M. D. McGehee, *Adv. Mater.* **2016**, *28*, 3937.
- [193] E. Garcia-Caurel, A. De Martino, J.-P. Gaston, L. Yan, *Appl. Spectrosc.* **2013**, *67*, 1.
- [194] A. Čampa, in *Proceedings of the 48th International Conference on Microelectronics, Devices and Materials & the Workshop on Ceramic Microsystems*, Otočec, Slovenia **2012**.
- [195] A. Tejada, S. Braunger, L. Korte, S. Albrecht, B. Rech, J. A. Guerra, *J. Appl. Phys.* **2018**, *123*, 175302.
- [196] M. van Eerden, M. Jaysankar, A. Hadipour, T. Merckx, J. J. Schermer, T. Aernouts, J. Poortmans, U. W. Paetzold, *Adv. Opt. Mater.* **2017**, *5*, 1700151.
- [197] B. Lipovšek, A. Čampa, F. Guo, C. J. Brabec, K. Forberich, J. Krč, M. Topič, *Opt. Express* **2017**, *25*, A176.
- [198] M. Morales-Masis, S. Martin De Nicolas, J. Holovsky, S. De Wolf, C. Ballif, *IEEE J. Photovolt.* **2015**, *5*, 1340.
- [199] P. Löper, M. Stuckelberger, B. Niesen, J. Werner, M. Filipič, S.-J. Moon, J.-H. Yum, M. Topič, S. De Wolf, C. Ballif, *J. Phys. Chem. Lett.* **2015**, *6*, 66.
- [200] M. Shirayama, H. Kadokawa, T. Miyadera, T. Sugita, M. Tamakoshi, M. Kato, T. Fujiseki, D. Murata, S. Hara, T. N. Murakami, S. Fujimoto, M. Chikamatsu, H. Fujiwara, *Phys. Rev. Appl.* **2016**, *5*, <https://doi.org/10.1103/PhysRevApplied.5.014012>.
- [201] P. F. Ndione, Z. Li, K. Zhu, *J. Mater. Chem. C* **2016**, *4*, 7775.
- [202] S. Braunger, L. E. Mundt, C. M. Wolff, M. Mews, C. Rehermann, M. Jošt, A. Tejada, D. Eisenhauer, C. Becker, J. A. Guerra, E. Unger, L. Korte, D. Neher, M. C. Schubert, B. Rech, S. Albrecht, *J. Phys. Chem. C* **2018**, *122*, 17123.
- [203] D. P. McMeekin, G. Sadoughi, W. Rehman, G. E. Eperon, M. Saliba, M. T. Horantner, A. Haghhighirad, N. Sakai, L. Korte, B. Rech, M. B. Johnston, L. M. Herz, H. J. Snaith, *Science* **2016**, *351*, 151.
- [204] S. Manzoor, J. Häusele, K. A. Bush, A. F. Palmstrom, J. Carpenter, Z. J. Yu, S. F. Bent, M. D. Mcgehee, Z. C. Holman, *Opt. Express* **2018**, *26*, 27441.
- [205] J. Tauc, *Mater. Res. Bull.* **1968**, *3*, 37.
- [206] A. J. Bett, P. S. C. Schulze, K. M. Winkler, Å-Z. S. Kabakli, I. Ketterer, L. E. Mundt, S. K. Reichmuth, G. Siefer, L. Cojocaru, L. Tutsch, M. Bivour, M. Hermle, S. W. Glunz, J. C. Goldschmidt, *Prog. Photovolt. Res. Appl.* **2019**, *28*, 99.
- [207] E. Aydin, M. De Bastiani, X. Yang, M. Sajjad, F. Aljamaan, Y. Smirnov, M. N. Hedhili, W. Liu, T. G. Allen, L. Xu, E. Van Kerschaver, M. Morales-Masis, U. Schwingenschlögl, S. De Wolf, *Adv. Funct. Mater.* **2019**, *29*, 1901741.
- [208] B. Lipovsek, J. Krc, M. Topic, *IEEE J. Photovoltaics* **2014**, *4*, 639.
- [209] R. Santbergen, T. Meguro, T. Suezaki, G. Koizumi, K. Yamamoto, M. Zeman, *IEEE J. Photovoltaics* **2017**, *7*, 919.
- [210] S. Altazin, L. Stepanova, J. Werner, B. Niesen, C. Ballif, B. Ruhstaller, *Opt. Express* **2018**, *26*, A579.
- [211] M. Filipič, P. Löper, B. Niesen, S. De Wolf, J. Krč, C. Ballif, M. Topič, *Opt. Express* **2015**, *23*, A263.
- [212] S. Fantacci, F. De Angelis, M. K. Nazeeruddin, M. Grätzel, *J. Phys. Chem. C* **2011**, *115*, 23126.
- [213] H. Dong, H. Zhu, Q. Meng, X. Gong, W. Hu, *Chem. Soc. Rev.* **2012**, *41*, 1754.
- [214] L. Kegelmann, P. Tockhorn, C. M. Wolff, J. A. Márquez, S. Caicedo-Dávila, L. Korte, T. Unold, W. Lövenich, D. Neher, B. Rech, S. Albrecht, *ACS Appl. Mater. Interfaces* **2019**, *11*, 9172.
- [215] T. Duong, Y. Wu, H. Shen, J. Peng, X. Fu, D. Jacobs, E.-C. Wang, T. C. Kho, K. C. Fong, M. Stocks, E. Franklin, A. Blakers, N. Zin, K. McIntosh, W. Li, Y.-B. Cheng, T. P. White, K. Weber, K. Catchpole, *Adv. Energy Mater.* **2017**, *7*, 1700228.
- [216] L. Mazzarella, M. Werth, K. Jäger, M. Jošt, L. Korte, S. Albrecht, R. Schlatmann, B. Stannowski, *Opt. Express* **2018**, *26*, A487.
- [217] M. Jaysankar, M. Filipič, B. Zielinski, R. Schmager, W. Song, W. Qiu, U. W. Paetzold, T. Aernouts, M. Debucquo, R. Gehlhaar, J. Poortmans, *Energy Environ. Sci.* **2018**, *11*, 1489.
- [218] R. Schmager, I. M. Hossain, F. Schackmar, B. S. Richards, G. Gomard, U. W. Paetzold, *Sol. Energy Mater. Sol. Cells* **2019**, *201*, 110080.

- [219] R. Schmager, G. Gomard, B. S. Richards, U. W. Paetzold, *Sol. Energy Mater. Sol. Cells* **2019**, *192*, 65.
- [220] Q. Xu, Y. Zhao, X. Zhang, *Sol. RRL* **2019**, *4*, 1900206.
- [221] M. T. Hörantner, T. Leijtens, M. E. Ziffer, G. E. Eperon, M. G. Christoforo, M. D. McGehee, H. J. Snaith, *ACS Energy Lett.* **2017**, *2*, 2506.
- [222] R. Schmager, M. Langenhorst, J. Lehr, U. Lemmer, B. S. Richards, U. W. Paetzold, *Opt. Express* **2019**, *27*, A507.
- [223] O. Dupré, B. Niesen, S. De Wolf, C. Ballif, *J. Phys. Chem. Lett.* **2018**, *9*, 446.
- [224] D. Schroder, *Semiconductor Material and Device Characterization*, 3rd ed., John Wiley & Sons, Ltd, Hoboken, New Jersey, USA **2005**.
- [225] I. Miccoli, F. Edler, H. Pfñür, C. Tegenkamp, *J. Phys. Condens. Matter* **2015**, *27*, 223201.
- [226] M. Morales-Masis, S. De Wolf, R. Woods-Robinson, J. W. Ager, C. Ballif, *Adv. Electron. Mater.* **2017**, *3*, 1600529.
- [227] X. Fan, W. Nie, H. Tsai, N. Wang, H. Huang, Y. Cheng, R. Wen, L. Ma, F. Yan, Y. Xia, *Adv. Sci.* **2019**, *6*, 1900813.
- [228] N. N. Rosli, M. A. Ibrahim, N. Ahmad Ludin, M. A. Mat Teridi, K. Sopian, *Renew. Sustain. Energy Rev.* **2019**, *99*, 83.
- [229] J. Liu, D. Jia, J. M. Gardner, E. M. J. Johansson, X. Zhang, *Mater. Today Energy* **2019**, *13*, 152.
- [230] W. H. Nguyen, C. D. Baillie, E. L. Unger, M. D. McGehee, *J. Am. Chem. Soc.* **2014**, *136*, 10996.
- [231] D. C. Look, D. C. Reynolds, J. R. Sizelove, R. L. Jones, C. W. Litton, G. Cantwell, W. C. Harsch, *Solid State Commun.* **1998**, *105*, 399.
- [232] K. Ellmer, *J. Phys. Appl. Phys.* **2001**, *34*, 3097.
- [233] A. Valla, P. Carroy, F. Ozanne, D. Muñoz, *Sol. Energy Mater. Sol. Cells* **2016**, *157*, 874.
- [234] K. Ellmer, R. Mientus, *Thin Solid Films* **2008**, *516*, 4620.
- [235] L. M. Herz, *ACS Energy Lett.* **2017**, *2*, 1539.
- [236] C. C. Stoumpos, C. D. Malliakas, M. G. Kanatzidis, *Inorg. Chem.* **2013**, *52*, 9019.
- [237] R. A. Sinton, A. Cuevas, *Appl. Phys. Lett.* **1996**, *69*, 2510.
- [238] A. B. Sproul, *J. Appl. Phys.* **1994**, *76*, 2851.
- [239] C. Leendertz, N. Mingirulli, T. F. Schulze, J. P. Kleider, B. Rech, L. Korte, *Appl. Phys. Lett.* **2011**, *98*, 202108.
- [240] S. Steingrube, P. P. Altermatt, D. S. Steingrube, J. Schmidt, R. Brendel, *J. Appl. Phys.* **2010**, *108*, 014506.
- [241] L. Wang, C. McCleese, A. Kovalsky, Y. Zhao, C. Burda, *J. Am. Chem. Soc.* **2014**, *136*, 12205.
- [242] L. Ma, F. Hao, C. C. Stoumpos, B. T. Phelan, M. R. Wasielewski, M. G. Kanatzidis, *J. Am. Chem. Soc.* **2016**, *138*, 14750.
- [243] T. Leijtens, G. E. Eperon, A. J. Barker, G. Grancini, W. Zhang, J. M. Ball, A. R. S. Kandada, H. J. Snaith, A. Petrozza, *Energy Environ. Sci.* **2016**, *9*, 3472.
- [244] M. B. Johnston, L. M. Herz, *Acc. Chem. Res.* **2016**, *49*, 146.
- [245] C. L. Davies, M. R. Filip, J. B. Patel, T. W. Crothers, C. Verdi, A. D. Wright, R. L. Milot, F. Giustino, M. B. Johnston, L. M. Herz, *Nat. Commun.* **2018**, *9*, 1.
- [246] E. M. Hutter, M.-A. C. Gélez-Rueda, A. Osharov, V. Bulović, F. C. Grozema, S. D. Stranks, T. J. Savenije, *Nat. Mater.* **2017**, *16*, 115.
- [247] C. S. Ponseca, T. J. Savenije, M. Abdellah, K. Zheng, A. Yartsev, T. Pascher, T. Harlang, P. Chabera, T. Pullerits, A. Stepanov, J.-P. Wolf, V. Sundström, *J. Am. Chem. Soc.* **2014**, *136*, 5189.
- [248] A. Marchioro, J. L. Teuscher, D. Friedrich, M. Kunst, R. van de Krol, T. Moehl, M. Grätzel, J.-E. Moser, *Nat. Photonics* **2014**, *8*, 250.
- [249] E. Guillén, F. J. Ramos, J. A. Anta, S. Ahmad, *J. Phys. Chem. C* **2014**, *118*, 22913.
- [250] A. Guerrero, G. Garcia-Belmonte, I. Mora-Sero, J. Bisquert, Y. S. Kang, T. J. Jacobsson, J.-P. Correa-Baena, A. Hagfeldt, *J. Phys. Chem. C* **2016**, *120*, 8023.
- [251] A. Baumann, K. Tvingstedt, M. C. Heiber, S. Väth, C. Momblona, H. J. Bolink, V. Dyakonov, *APL Mater.* **2014**, *2*, 081501.
- [252] M. Abdi-Jalebi, M. I. Dar, A. Sadhanala, S. P. Senanayak, M. Franckevičius, N. Arora, Y. Hu, M. K. Nazeeruddin, S. M. Zakeeruddin, M. Grätzel, R. H. Friend, *Adv. Energy Mater.* **2016**, *6*, 1502472.
- [253] D. Koushik, W. J. H. Verhees, Y. Kuang, S. Veenstra, D. Zhang, M. A. Verheijen, M. Creatore, R. E. I. Schropp, *Energy Environ. Sci.* **2016**.
- [254] S. Chen, X. Du, D. Lin, F. Xie, W. Xie, L. Gong, W. Zhang, P. Liu, J. Chen, *J. Electron Spectrosc. Relat. Phenom.* **2018**, *229*, 108.
- [255] U. B. Cappel, S. Svanström, V. Lanzilotto, F. O. L. Johansson, K. Aitola, B. Philippe, E. Giangrisostomi, R. Ovsyannikov, T. Leitner, A. Föhlisch, S. Svensson, N. Mårtensson, G. Boschloo, A. Lindblad, H. Rensmo, *ACS Appl. Mater. Interfaces* **2017**, *9*, 34970.
- [256] F. Zu, C. M. Wolff, M. Ralaiarisoa, P. Amsalem, D. Neher, N. Koch, *ACS Appl. Mater. Interfaces* **2019**, *11*, 21578.
- [257] J. Endres, D. A. Egger, M. Kulbak, R. A. Kerner, L. Zhao, S. H. Silver, G. Hodes, B. P. Rand, D. Cahen, L. Kronik, A. Kahn, *J. Phys. Chem. Lett.* **2016**, *7*, 2722.
- [258] F. Zu, P. Amsalem, D. A. Egger, R. Wang, C. M. Wolff, H. Fang, M. A. Loi, D. Neher, L. Kronik, S. Duhm, N. Koch, *J. Phys. Chem. Lett.* **2019**, *10*, 601.
- [259] N. K. Noel, S. N. Habreutinger, A. Pellaroque, F. Pulvirenti, B. Wenger, F. Zhang, Y.-H. Lin, O. G. Reid, J. Leisen, Y. Zhang, S. Barlow, S. R. Marder, A. Kahn, H. J. Snaith, C. B. Arnold, B. P. Rand, *Energy Environ. Sci.* **2019**, *12*, 3063.
- [260] R. L. Z. Hoye, P. Schulz, L. T. Schelhas, A. M. Holder, K. H. Stone, J. D. Perkins, D. Vigil-Fowler, S. Siol, D. O. Scanlon, A. Zakutayev, A. Walsh, I. C. Smith, B. C. Melot, R. C. Kurchin, Y. Wang, J. Shi, F. C. Marques, J. J. Berry, W. Tumas, S. Lany, V. Stevanović, M. F. Toney, T. Buonassisi, *Chem. Mater.* **2017**, *29*, 1964.
- [261] L. K. Ono, Y. Qi, *J. Phys. Chem. Lett.* **2016**, *7*, 4764.
- [262] D. Shin, D. Kang, J. Jeong, S. Park, M. Kim, H. Lee, Y. Yi, *J. Phys. Chem. Lett.* **2017**, *8*, 5423.
- [263] J. Hieulle, X. Wang, C. Stecker, D.-Y. Son, L. Qiu, R. Ohmann, L. K. Ono, A. Mugarza, Y. Yan, Y. Qi, *J. Am. Chem. Soc.* **2019**, *141*, 3515.
- [264] Z. Hawash, S. R. Raga, D.-Y. Son, L. K. Ono, N.-G. Park, Y. Qi, *J. Phys. Chem. Lett.* **2017**, *8*, 3947.
- [265] S. Tao, I. Schmidt, G. Brocks, J. Jiang, I. Tranca, K. Meerholz, S. Olthof, *Nat. Commun.* **2019**, *10*, 1.
- [266] J. Emara, T. Schnier, N. Pourdavoud, T. Riedl, K. Meerholz, S. Olthof, *Adv. Mater.* **2016**, *28*, 553.
- [267] R. L. Anderson, *IBM J Res Dev* **1960**, *4*, 283.
- [268] Q.-K. Wang, R.-B. Wang, P.-F. Shen, C. Li, Y.-Q. Li, L.-J. Liu, S. Duhm, J.-X. Tang, *Adv. Mater. Interfaces* **2015**, *2*, 1400528.
- [269] D. Di Girolamo, N. Phung, M. Jošt, A. Al-Ashouri, G. Chistiakova, J. Li, J. A. Márquez, T. Unold, L. Korte, S. Albrecht, A. Di Carlo, D. Dini, A. Abate, *Adv. Mater. Interfaces* **2019**, *6*, 1900789.
- [270] M. Sebastiani, L. Di Gaspare, G. Capellini, C. Bittencourt, F. Evangelisti, *Phys. Rev. Lett.* **1995**, *75*, 3352.
- [271] L. Korte, M. Schmidt, *J. Appl. Phys.* **2011**, *109*, 063714.
- [272] L. Korte, R. Rößler, C. Pettenkofer, *J. Appl. Phys.* **2014**, *115*, 203715.
- [273] V. Zardetto, B. L. Williams, A. Perrotta, F. Di Giacomo, M. A. Verheijen, R. Andriessen, W. M. M. Kessels, M. Creatore, *Sustain. Energy Fuels* **2017**, *1*, 30.
- [274] A. Rolland, L. Pedesseau, M. L. Kepenekian, C. Katan, Y. Huang, S. Wang, C. Cornet, O. Durand, J. Even, *Opt. Quantum Electron.* **2017**, *50*, 21.
- [275] Synopsys TCAD. [Online]. Available: <https://www.synopsys.com/silicon/tcad.html>, (accessed: December 2019).
- [276] PC1D – Software for modelling a solar cell, *School of Photovoltaic and Renewable Energy Engineering*, 11-Nov-2013. [Online]. Available: <https://www.engineering.unsw.edu.au/energy-engineering/research/software-data-links/pc1d-software-for-modelling-a-solar-cell>, (accessed: December 2019).

- [277] M. Burgelman, K. Decock, S. Khelifi, A. Abass, *Thin Solid Films* **2013**, 535, 296.
- [278] R. Varache, C. Leendertz, M. E. Gueunier-Farret, J. Haschke, D. Muñoz, L. Korte, *Sol. Energy Mater. Sol. Cells* **2015**, 141, 14.
- [279] C. Messmer, M. Bivour, J. Schön, M. Hermle, *J. Appl. Phys.* **2018**, 124, 085702.
- [280] J. Wang, W. Fu, S. Jariwala, I. Sinha, A. K.-Y. Jen, D. S. Ginger, *ACS Energy Lett.* **2019**, 4, 222.
- [281] T. Kirchartz, J. Nelson, in *Multiscale Modelling of Organic and Hybrid Photovoltaics* (Eds: D. Beljonne, J. Cornil), Springer, Berlin, Heidelberg **2014**, pp. 279–324.
- [282] K. Tarettö, M. Soldera, A. Koffman-Frischknecht, *IEEE J. Photovolt.* **2017**, 7, 206.
- [283] S. van Reenen, M. Kemerink, H. J. Snaith, *J. Phys. Chem. Lett.* **2015**, 6, 3808.
- [284] C. Eames, J. M. Frost, P. R. F. Barnes, B. C. O'Regan, A. Walsh, M. S. Islam, *Nat. Commun.* **2015**, 6, <https://doi.org/10.1038/ncomms8497>.
- [285] L. Bertoluzzi, C. C. Boyd, N. Rolston, J. Xu, R. Prasanna, B. C. O'Regan, M. D. McGehee, *Joule* **2019**, 4, 109.
- [286] P. Lopez-Varo, J. A. Jiménez-Tejada, M. García-Rosell, S. Ravishankar, G. Garcia-Belmonte, J. Bisquert, O. Almora, *Adv. Energy Mater.* **2018**, 8, 1702772.
- [287] W. Blume, *Byte* **1986**, 11, 165.
- [288] LTspice [Online]. Available: <https://www.analog.com/en/design-center/design-tools-and-calculators/ltpsice-simulator.html>, (accessed: December 2019).
- [289] L. Cojocaru, S. Uchida, P. V. V. Jayaweera, S. Kaneko, Y. Toyoshima, J. Nakazaki, T. Kubo, H. Segawa, *Appl. Phys. Express* **2017**, 10, 025701.
- [290] L. Cojocaru, S. Uchida, P. V. V. Jayaweera, S. Kaneko, Y. Toyoshima, J. Nakazaki, T. Kubo, H. Segawa, *Appl. Phys. Express* **2017**, 10, 059102.
- [291] A. W. Walker, O. Hohn, D. N. Micha, B. Blasi, A. W. Bett, F. Dimroth, *IEEE J. Photovolt.* **2015**, 5, 1636.
- [292] M. Hermle, G. Létay, S. P. Philipps, A. W. Bett, *Prog. Photovolt. Res. Appl.* **2008**, 16, 409.
- [293] M. Steiner, W. Guter, G. Peharz, S. P. Philipps, F. Dimroth, A. W. Bett, *Prog. Photovolt. Res. Appl.* **2012**, 20, 274.
- [294] J. F. Geisz, M. A. Steiner, I. Garcia, R. M. France, W. E. McMahon, C. R. Osterwald, D. J. Friedman, *IEEE J. Photovolt.* **2015**, 5, 1827.
- [295] H. Wagner, T. Ohrdes, A. Dastgheib-Shirazi, B. Puthen-Veettil, D. König, P. P. Altermatt, *J. Appl. Phys.* **2014**, 115, 044508.
- [296] E. L. Warren, M. G. Deceglie, M. Rienäcker, R. Peibst, A. C. Tamboli, P. Stradins, *Sustain. Energy Fuels* **2018**, 2, 1141.
- [297] M. Zeman, J. Krc, *J. Mater. Res.* **2008**, 23, 889.
- [298] L. Esaki, *Phys. Rev.* **1958**, 109, 603.
- [299] A. Singh, A. Gagliardi, *Sol. Energy* **2019**, 187, 39.
- [300] Z. Li, T. R. Klein, D. H. Kim, M. Yang, J. J. Berry, M. F. A. M. van Hest, K. Zhu, *Nat. Rev. Mater.* **2018**, 3, 1.
- [301] T. Trupke, B. Mitchell, J. W. Weber, W. McMillan, R. A. Bardos, R. Kroese, *Energy Procedia* **2012**, 15, 135.
- [302] O. Breitenstein, W. Warta, M. Langenkamp, *Lock-in Thermography*, Springer, Berlin, Heidelberg **2010**.
- [303] G. El-Hajje, C. Momblona, L. Gil-Escríg, J. Ávila, T. Guillermot, J.-F. Guillemoles, M. Sessolo, H. J. Bolink, L. Lombez, *Energy Environ. Sci.* **2016**, 9, 2286.
- [304] A. Redinger, S. Kretzschmar, T. Unold, in *2016 IEEE 43rd Photovoltaic Specialists Conference (PVSC)*, **2016**, pp. 3559–3562.
- [305] R. E. Beal, D. J. Slotcavage, T. Leijtens, A. R. Bowring, R. A. Belisle, W. H. Nguyen, G. F. Burkhard, E. T. Hoke, M. D. McGehee, *J. Phys. Chem. Lett.* **2016**, 7, 746.
- [306] K. Tvingstedt, O. Malinkiewicz, A. Baumann, C. Deibel, H. J. Snaith, V. Dyakonov, H. J. Bolink, *Sci. Rep.* **2014**, 4, 1.
- [307] U. Rau, *Phys. Rev. B* **2007**, 76.
- [308] L. E. Mundt, F. D. Heinz, S. Albrecht, M. Mundus, M. Saliba, J. P. Correa-Baena, E. H. Anaraki, L. Korte, M. Gratzel, A. Hagfeldt, B. Rech, M. C. Schubert, S. W. Glunz, *IEEE J. Photovolt.* **2017**, 7, 1081.
- [309] H. Straube, M. Siegloch, A. Gerber, J. Bauer, O. Breitenstein, *Phys. Status Solidi C* **2011**, 8, 1339.
- [310] M. Stolterfoht, V. M. Le Corre, M. Feuerstein, P. Caprioglio, L. J. A. Koster, D. Neher, *ACS Energy Lett.* **2019**, 4, 2887.
- [311] P. Würfel, W. Ruppel, *J. Lumir.* **1981**, 24-25, 925.
- [312] R. T. Ross, *J. Chem. Phys.* **1967**, 46, 4590.
- [313] A. Redinger, T. Unold, *Sci. Rep.* **2018**, 8, 1874.
- [314] P. Caprioglio, M. Stolterfoht, C. M. Wolff, T. Unold, B. Rech, S. Albrecht, D. Neher, *Adv. Energy Mater.* **0**, p. 1901631.
- [315] Z. Liu, L. Krückemeier, B. Krogmeier, B. Klingebiel, J. A. Márquez, S. Levcenko, S. Öz, S. Mathur, U. Rau, T. Unold, T. Kirchartz, *ACS Energy Lett.* **2018**, 110.
- [316] F. Staub, H. Hempel, J.-C. Hebig, J. Mock, U. W. Paetzold, U. Rau, T. Unold, T. Kirchartz, *Phys. Rev. Appl.* **2016**, 6, 044017.
- [317] D. Shvydka, J. P. Rakotonaina, O. Breitenstein, *Appl. Phys. Lett.* **2004**, 84, 729.
- [318] G. D. Spyropoulos, C. O. Ramirez Quiroz, M. Salvador, Y. Hou, N. Gasparini, P. Schweizer, J. Adams, P. Kubis, N. Li, E. Spiecker, T. Ameri, H.-J. Egelhaaf, C. J. Brabec, *Energy Environ. Sci.* **2016**, 9, 2302.
- [319] H.-S. Kim, C.-R. Lee, J.-H. Irm, K.-B. Lee, T. Moehl, A. Marchioro, S.-J. Moon, R. Humphry-Baker, J.-H. Yum, J. E. Moser, M. Grätzel, N.-G. Park, *Sci. Rep.* **2012**, 2, 1.
- [320] E. L. Unger, E. T. Hoke, C. D. Bailie, W. H. Nguyen, A. R. Bowring, T. Heumüller, M. G. Christoforo, M. D. McGehee, *Energy Env. Sci.* **2014**, 7, 3690.
- [321] M. A. Steiner, J. F. Geisz, T. E. Moriarty, R. M. France, W. E. McMahon, J. M. Olson, S. R. Kurtz, D. J. Friedman, *IEEE J. Photovolt.* **2013**, 3, 879.
- [322] T. Ameri, G. Dennler, C. Lungenschmied, C. J. Brabec, *Energy Environ. Sci.* **2009**, 2, 347.
- [323] IEC Standard 60904-3: Measurement Principles for Terrestrial Photovoltaic (PV) Solar Devices With Reference Spectral Irradiance Data, International Electrotechnical Commission, Geneva, Switzerland **2008**.
- [324] G. P. Smestad, F. C. Krebs, C. M. Lampert, C. G. Granqvist, K. L. Chopra, X. Mathew, H. Takakura, *Sol. Energy Mater. Sol. Cells* **2008**, 92, 371.
- [325] W. Tress, N. Marinova, T. Moehl, S. M. Zakeeruddin, M. K. Nazeeruddin, M. Grätzel, *Energy Environ. Sci.* **2015**, 8, 995.
- [326] P. Calado, A. M. Telford, D. Bryant, X. Li, J. Nelson, B. C. O'Regan, P. R. F. Barnes, *Nat. Commun.* **2016**, 7, 1.
- [327] S. A. L. Weber, I. M. Hermes, S.-H. Turren-Cruz, C. Gort, V. W. Bergmann, L. Gilson, A. Hagfeldt, M. Graetzel, W. Tress, R. Berger, *Energy Environ. Sci.* **2018**.
- [328] H. Yu, H. Lu, F. Xie, S. Zhou, N. Zhao, *Adv. Funct. Mater.* **2016**, 26, 1411.
- [329] E. Zimmermann, K. K. Wong, M. Müller, H. Hu, P. Ehrenreich, M. Kohlstädt, U. Würfel, S. Mastrioanni, G. Mathiazhang, A. Hinsch, T. P. Gujar, M. Thelakkat, T. Pfadler, L. Schmidt-Mende, *APL Mater.* **2016**, 4, 091901.
- [330] Y. Wang, X. Liu, Z. Zhou, P. Ru, H. Chen, X. Yang, L. Han, *Adv. Mater.* **2019**, 31, 1803231.
- [331] Y. Hishikawa, H. Shimura, T. Ueda, A. Sasaki, Y. Ishii, *Curr. Appl. Phys.* **2016**, 16, 898.
- [332] J. A. Christians, J. S. Manser, P. V. Kamat, *J. Phys. Chem. Lett.* **2015**, 6, 852.
- [333] A. Czudek, K. Hirselandt, L. Kegelmann, A. Al-Ashouri, M. Još, W. Zuo, A. Abate, L. Korte, S. Albrecht, J. Dagar, E. L. Unger, *ArXiv190605028 Cond-Mat Physicsphysics* **2019**.
- [334] V. Shrotriya, G. Li, Y. Yao, T. Moriarty, K. Emery, Y. Yang, *Adv. Funct. Mater.* **2006**, 16, 2016.

- [335] M. Meusel, R. Adelhelm, F. Dimroth, A. W. Bett, W. Warta, *Prog. Photovolt. Res. Appl.* **2002**, *10*, 243.
- [336] T. Moriarty, J. Jablonski, K. Emery, in *2012 38th IEEE Photovoltaic Specialists Conference*, **2012**, pp. 001291–001295.
- [337] J.-P. Correa-Baena, Y. Luo, T. M. Brenner, J. Snaider, S. Sun, X. Li, M. A. Jensen, N. T. P. Hartono, L. Nienhaus, S. Wieghold, J. R. Poindexter, S. Wang, Y. S. Meng, T. Wang, B. Lai, M. V. Holt, Z. Cai, M. G. Bawendi, L. Huang, T. Buonassisi, D. P. Fenning, *Science* **2019**, *363*, 627.
- [338] K. O. Brinkmann, J. Zhao, N. Pourdavoud, T. Becker, T. Hu, S. Olthof, K. Meerholz, L. Hoffmann, T. Gahlmann, R. Heiderhoff, M. F. Oszajca, N. A. Luechinger, D. Rogalla, Y. Chen, B. Cheng, T. Riedl, *Nat. Commun.* **2017**, *8*, 13938.
- [339] R. Cheacharoen, N. Rolston, D. Harwood, K. A. Bush, R. H. Dauskardt, M. D. McGehee, *Energy Environ. Sci.* **2018**, *11*, 144.
- [340] T. Matsui, T. Yamamoto, T. Nishihara, R. Morisawa, T. Yokoyama, T. Sekiguchi, T. Negami, *Adv. Mater.* **2019**, *31*, 1806823.
- [341] R. Cheacharoen, C. C. Boyd, G. F. Burkhard, T. Leijtens, J. A. Raiford, K. A. Bush, S. F. Bent, M. D. McGehee, *Sustain. Energy Fuels* **2018**, *2*, 2398.
- [342] T. Leijtens, K. Bush, R. Cheacharoen, R. Beal, A. Bowring, M. D. McGehee, *J. Mater. Chem. A* **2017**, *5*, 11483.
- [343] R. Wang, M. Mujahid, Y. Duan, Z.-K. Wang, J. Xue, Y. Yang, *Adv. Funct. Mater.* **2019**, *29*, 1808843.
- [344] Q. Wang, N. Phung, D. Di Girolamo, P. Vivo, A. Abate, *Energy Environ. Sci.* **2019**, *12*, 865.
- [345] C. C. Boyd, R. Cheacharoen, T. Leijtens, M. D. McGehee, *Chem. Rev.* **2019**, *119*, 3418.
- [346] M. V. Khenkin, E. A. Katz, A. Abate, G. Bardizza, J. J. Berry, C. Brabec, F. Brunetti, V. Bulović, Q. Burlingame, A. Di Carlo, R. Cheacharoen, Y.-B. Cheng, A. Colsmann, S. Cros, K. Domanski, M. Dusza, C. J. Fell, S. R. Forrest, Y. Galagan, D. Di Girolamo, M. Grätzel, A. Hagfeldt, E. von Hauff, H. Hoppe, J. Kettle, H. Köbler, M. S. Leite, S. Liu, Y.-L. Loo, J. M. Luther, C.-Q. Ma, M. Madsen, M. Manceau, M. Matheron, M. McGehee, R. Meitzner, M. K. Nazeeruddin, A. F. Nogueira, Ç. Odabaşı, A. Osharov, N.-G. Park, M. O. Reese, F. De Rossi, M. Saliba, U. S. Schubert, H. J. Snaith, S. D. Stranks, W. Tress, P. A. Troshin, V. Turkovic, S. Veenstra, I. Visoly-Fisher, A. Walsh, T. Watson, H. Xie, R. Yıldırım, S. M. Zakeeruddin, K. Zhu, M. Lira-Cantu, *Nat. Energy* **2020**, *5*, 35.
- [347] N. Arora, M. I. Dar, A. Hinderhofer, N. Pellet, F. Schreiber, S. M. Zakeeruddin, M. Grätzel, *Science* **2017**, *358*, 768.
- [348] Y. Hou, X. Du, S. Scheiner, D. P. McMeekin, Z. Wang, N. Li, M. S. Killian, H. Chen, M. Richter, I. Levchuk, N. Schrenker, E. Spiecker, T. Stubhan, N. A. Luechinger, A. Hirsch, P. Schmuki, H.-P. Steinrück, R. H. Fink, M. Halik, H. J. Snaith, C. J. Brabec, *Science* **2017**, *358*, 1192.
- [349] Z. Wang, Q. Lin, F. P. Chmiel, N. Sakai, L. M. Herz, H. J. Snaith, *Nat. Energy* **2017**, *2*, 1.
- [350] J.-W. Lee, Z. Dai, T.-H. Han, C. Choi, S.-Y. Chang, S.-J. Lee, N. De Marco, H. Zhao, P. Sun, Y. Huang, Y. Yang, *Nat. Commun.* **2018**, *9*, 1.
- [351] M. Saliba, M. Stolterfoht, C. M. Wolff, D. Neher, A. Abate, *Joule* **2018**, *2*, 1019.
- [352] L. Meng, J. You, Y. Yang, *Nat. Commun.* **2018**, *9*, 1.
- [353] J. A. Christians, S. N. Habreutinger, J. J. Berry, J. M. Luther, *ACS Energy Lett.* **2018**, *3*, 2136.
- [354] Y. Bai, Y. Lin, L. Ren, X. Shi, E. Strounina, Y. Deng, Q. Wang, Y. Fang, X. Zheng, Y. Lin, Z.-G. Chen, Y. Du, L. Wang, J. Huang, *ACS Energy Lett.* **2019**, *4*, 1231.
- [355] P. Holzhey, M. Saliba, *J. Mater. Chem. A* **2018**, *6*, 21794.
- [356] B. Chen, J. Song, X. Dai, Y. Liu, P. N. Rudd, X. Hong, J. Huang, *Adv. Mater.* **2019**, *31*, 1902413.
- [357] R. A. Z. Razera, D. A. Jacobs, F. Fu, P. Fiala, M. Dussouillez, F. Sahli, T. C. J. Yang, L. Ding, A. Walter, A. F. Feil, H. I. Boudinov, S. Nicolay, C. Ballif, Q. Jeangros, *J. Mater. Chem. A* **2019**, *8*, 242.
- [358] A. R. Bowring, L. Bertoluzzi, B. C. O'Regan, M. D. McGehee, *Adv. Energy Mater.* **2018**, *8*, 1702365.
- [359] A. S. Brown, M. A. Green, *Phys. E Low-Dimens. Syst. Nanostructures* **2002**, *14*, 96.
- [360] D. Luo, R. Su, W. Zhang, Q. Gong, R. Zhu, *Nat. Rev. Mater.* **2019**, *1*, <https://doi.org/10.1038/s41578-019-0151-y>.
- [361] M. A. Green, M. J. Keevers, *Prog. Photovolt. Res. Appl.* **1995**, *3*, 189.